NATIONAL AND KAPODISTRIAN UNIVERSITY OF ATHENS

SCHOOL OF SCIENCE
DEPARTMENT OF INFORMATICS AND TELECOMMUNICATION

MSc THESIS

Theoretical study and simulation of Underwater Wireless Optical Communications channels with diffused light transmissions in the visible spectrum

Ioanna E. Karametou
Marinela R. Mertiri

Supervisor: **Dimitris Syvridis, Professor**

ATHENS

JULY 2017

ΕΘΝΙΚΟ ΚΑΙ ΚΑΠΟΔΙΣΤΡΙΑΚΟ ΠΑΝΕΠΙΣΤΗΜΙΟ ΑΘΗΝΩΝ

ΣΧΟΛΗ ΘΕΤΙΚΩΝ ΕΠΙΣΤΗΜΩΝ
ΤΜΗΜΑ ΠΛΗΡΟΦΟΡΙΚΗΣ ΚΑΙ ΤΗΛΕΠΙΚΟΙΝΩΝΙΩΝ

ΔΙΠΛΩΜΑΤΙΚΗ ΕΡΓΑΣΙΑ

Θεωρητική μελέτη και προσομοίωση υποθαλάσσιων ασύρματων οπτικών καναλιών με εφαρμογή διάχυτων μεταδόσεων στο ορατό φάσμα

Ιωάννα Ε. Καραμέτου
Μαρινέλα Ρ. Μερτίρη

Επιβλέπων: **Δημήτριος Συβρίδης,** Καθηγητής

ΑΘΗΝΑ

ΙΟΥΛΙΟΣ 2017

MSc THESIS

Theoretical study and simulation of Underwater Wireless Optical Communications channels with diffused light transmissions in the visible spectrum

Ioanna E. Karametou

S.N.: M1449

Marinela R. Mertiri

S.N.: M1453

SUPERVISOR: **Dimitrios Syvridis, Professor**

ΔΙΠΛΩΜΑΤΙΚΗ ΕΡΓΑΣΙΑ

Θεωρητική μελέτη και προσομοίωση υποθαλάσσιων ασύρματων οπτικών καναλιών με εφαρμογή διάχυτων μεταδόσεων στο ορατό φάσμα

Ιωάννα Ε. Καραμέτου

Α.Μ.: Μ1449

Μαρινέλα Ρ. Μερτίρη

Α.Μ.: Μ1453

ΕΠΙΒΛΕΠΟΝΤΕΣ: **Δημήτριος Συβρίδης,** Καθηγητής

ABSTRACT

In the recent years, there is an increasing research interest in the underwater wireless optical communications. The scope of the current thesis is to present a theoretical study of underwater wireless optical channels where diffused transmissions are applied in the visible spectrum. For the purposes of this work, the light propagation inside the sea is simulated by a model based on the Monte Carlo method.

Initially, we analyze the optical characteristics of water and we present the most significant technologies that have been implemented for wireless data transmission on underwater channels. Moreover, we study in depth the Monte Carlo technique by analyzing its principles as regards the propagation of a large number of photons.

The simulation model refers to a point source at the seabed, which has no visual contact with the receiver. In this work, the relations of the received power with the transmitter's elevation angle, the transmitter's aperture angle, the distance between the transmitter and the receiver and the field of view of the receiver are investigated. These relations are examined in pure sea, clear ocean, coastal water, turbid water. The case where the transmitter is not located at the bottom of the sea is investigated, as well. Then, the channel's impulse responses for coastal and turbid waters are studied for various distances between transmitter and receiver.

Finally, based on the simulation results, we compare the examined environments and we derive some important observations and conclusions regarding the design, the development and the modeling of underwater wireless optical links operating in the visible spectrum.

SUBJECT AREA: Underwater wireless communications operating in the visible spectrum

KEYWORDS: wireless underwater communications, optical channels, scattering, absorption, Monte Carlo method

ΠΕΡΙΛΗΨΗ

Τα τελευταία χρόνια, υπάρχει αυξανόμενο ερευνητικό ενδιαφέρον γύρω από τις υποθαλάσσιες ασύρματες οπτικές επικοινωνίες. Το αντικείμενο της διπλωματικής εργασίας είναι η θεωρητική μελέτη των υποθαλάσσιων ασύρματων οπτικών καναλιών με εφαρμογή διάχυτων μεταδόσεων στο ορατό φάσμα. Στα πλαίσια της εργασίας αυτής, προσομοιώνεται η διάδοση του φωτός μέσα στη θάλασσα με ένα μοντέλο διάδοσης που βασίζεται στη μέθοδο Monte Carlo.

Αρχικά, αναλύουμε τα οπτικά χαρακτηριστικά του νερού και παρουσιάζουμε τις πιο σημαντικές τεχνολογίες που έχουν υλοποιηθεί για ασύρματη μετάδοση δεδομένων σε υποθαλάσσιες επικοινωνίες. Μελετάμε σε βάθος την τεχνική Monte Carlo με ανάλυση των αρχών της όσον αφορά τη διάδοση μεγάλου αριθμού φωτονίων.

Το μοντέλο της προσομοίωσης αφορά σημειακή πηγή στον βυθό της θάλασσας χωρίς οπτική επαφή με τον δέκτη. Στα πλαίσια της εργασίας, ερευνάται η σχέση της λαμβανόμενης ισχύος με τη γωνία ανύψωσης του πομπού, τη γωνία απόκλισης του πομπού, την απόστασης μεταξύ του πομπού και του δέκτη και το οπτικό πεδίο του δέκτη. Η σχέση αυτή εξετάζεται σε καθαρή θάλασσα, καθαρό ωκεανό, ρηχά νερά, θολά νερά. Η περίπτωση ο πομπός να μη βρίσκεται στον πάτο της θάλασσας εξετάζεται επίσης. Στη συνέχεια, μελετάται η κρουστική απόκριση του καναλιού για τα ρηχά και θολά νερά για διάφορες αποστάσεις μεταξύ πομπού και δέκτη.

Τελικά, με βάση τα αποτελέσματα της προσομοίωσης, συγκρίνουμε τα περιβάλλοντα που εξετάστηκαν και καταλήγουμε σε κάποιες σημαντικές παρατηρήσεις και συμπεράσματα σχετικά με τον σχεδιασμό, την ανάπτυξη και τη μοντελοποίηση υποθαλάσσιων ασύρματων οπτικών ζεύξεων στο ορατό φάσμα.

ΘΕΜΑΤΙΚΗ ΠΕΡΙΟΧΗ: Ασύρματες υποθαλάσσιες επικοινωνίες στο οπτικό φάσμα

ΛΕΞΕΙΣ ΚΛΕΙΔΙΑ: ασύρματες υποθαλάσσιες επικοινωνίες, οπτικά κανάλια, σκέδαση, απορρόφηση, μέθοδος Monte Carlo

We dedicate this master thesis to our families that have supported us in every way throughout our studies.

AKNOWLEDGMENTS

For the preparation of this Master Thesis, we would like to thank the supervisors, Professor Dimitris Syvridis and PhD Candidate Marilena Akriotou, for their time, co-operation and their valuable contribution to its completion.

CONTENTS

LIST OF FIGURES

LIST OF IMAGES

LIST OF TABLES

PREFACE

The current MSc thesis was implemented in the context of the graduate course of studies of the Department of Informatics and Telecommunications of National and Kapodistrian University of Athens, with MSc specialization in Telecommunications Systems and Network Technologies, during the academic year 2016 – 2017. The scope of this work is to present a theoretical study, extended by simulating scenarios, of the Underwater Wireless Optical Communications (UWOC) systems, where wavelengths in the visible optical spectrum were used for signal transmission. The simulations were realized by utilizing the Monte Carlo method in a Matlab project.

In Section 1, we present the most well known technologies as well as the theoretical aspects of Underwater Wireless Communications (UWC), paying special attention to the characteristics of optical UWC systems. Continuing with Section 2, we analytically describe the broadly used Monte Carlo simulation method, as implemented in our project. The scenarios for the experiments and the corresponding results are discussed in Sections 3 and 4, respectively. Finally, Section 5 summarizes the conclusions of the realized simulations.

1. INTRODUCTION

Collecting data from the ocean has been of significant interest to scientific, industrial and military communities for several years. These data are used for the purposes of scientific research, pollution monitoring, weather monitoring, seismic studies as well as oil and gas pipeline maintenance and security. Even though oceans and seas cover the majority of the Earth's surface, they are still generally unexplored. This is especially the case for deep sea waters.

The recent works have shown a special interest in underwater wireless sensor networks (UWSNs), because of their flexibility and simplicity of deployment compared to cabled networks. UWSN refers to the data transmission in an unguided water environment with the use of wireless carriers, such as radio-frequency (RF) waves, acoustic waves, and optical waves. A UWSN consists of spatially distributed autonomous nodes to which a number of sensors are connected. These nodes are linked together in order to exchange the data that are collected by the sensors. The network can provide knowledge about the physical events happening in the volatile underwater environment. More specifically, we can use such networks to assess the aqueous environment, monitor the seafloor activity for disaster prevention, survey the seismic activity in order to provide tsunami warnings, help underwater geochemical prospecting and model the weather impact on submarine life [1].

In regard to the communication link, we should pay special attention to the underwater channel properties. It is broadly known that radio frequencies are not suitable for wireless links in water, because they suffer from strong attenuation. Therefore, they can typically achieve communication ranges of a few centimeters only [1]. The use of acoustic waves is also problematic because of their limited bandwidth, their very low celerity and the large, high energy consuming antennas under use. On the other hand, optical wireless underwater communications turn out to be a promising alternative for communications over ranges of up to several tens of meters, as it is a cost-effective and low energy consumption solution. Using a proper wavelength (in the blue/green range, 450 nm to 550 nm), we can reach high data rates over moderate transmission ranges, depending on the water conditions and the transmitter/receiver parameters [1].

From a historical point of view, light has been used as a method of wireless communication for thousands of years and in a variety of ways. For example, around 1,000 BC in ancient China, beacon towers were used in order to transmit military information, while around 800 BC the ancient Greek and Roman armies sent signals with the use of polished shields which reflected the sunlight to the desired direction. In 1880, Alexander Graham Bell invented a wireless telephone system which used sunlight as the transmission medium. This system is considered as the first optoelectronic communication system in the world. In the 1960s, the invention of laser as an optical source changed the future of optical wireless communication (OWC). Thereafter, the scientific community has intensively studied the potentials of terrestrial OWC applications. In recent years, there is a growing interest in Underwater Optical Wireless Communications (UOWC) [2].

However, optical communication in water is tricky, since the optical beam is subject to intense attenuation due to high absorption and scattering. In addition to signal attenuation, scattering can cause Inter-Symbol Interference (ISI), resulting in pulse broadening. Consequently, absorption and scattering either degrade the quality of data transmission, especially for high data rates and over long distances, or require the implementation of computationally complex signal processing at the receiver. Thus, it is essential to characterize accurately the underwater optical channel and to set the

system parameters appropriately in order to achieve high-quality transmission. In the following sections we describe the water characteristics that affect the optical signals as well as the most broadly used technologies for underwater wireless communications.

1.1 Effect of water in the optical beam

The interaction between light and water is not so straightforward. A study of the phenomena that are involved in the process has to deal with the complicated subject of light interacting with matter as well as with the complex nature of the ocean environment. In this chapter we try to extract the most important aspects of this interaction as it applies to underwater free-space optical communication [4].

1.1.1 Optical properties of water

There are two major processes that affect light propagation in water, absorption, *a(λ)*, and scattering, *b(λ)*, which both depend on wavelength *λ*. Absorption is the inevitable loss of intensity and depends on the water's refractive index. As a matter of fact, in natural waters, it is difficult to distinguish absorption from scattering when taking measurements. The optical energy is absorbed not only by pure water itself, but also by the particles inside the sea, which can be even more absorptive. Some of the suspended materials that contribute to absorption, as described in Section 1.1.3, include Colored Dissolved Organic Material (CDOM) and phytoplankton (small microscopic plant with chlorophyll) [4].

On the other hand, scattering refers to the deflection of light from the original path, which can be caused by water molecules, particulate matter, and other dissolved substances in the water with size comparable to *λ* (diffraction) and/or with index of refraction different from that of the water (refraction) [1]. In contrast to absorption, scattering depends more on the various matters that exist in an underwater environment compared to its dependence on the wavelength of the light for the wavelength range of our interest (this will be described further in Subsection 1.1.3 where the reader can find Image 6) [1]. Therefore, its impact is more noticeable in coastal areas than in open oceans.

Image 1[1] depicts the propagation behavior of light beam when encountering a particle in water.

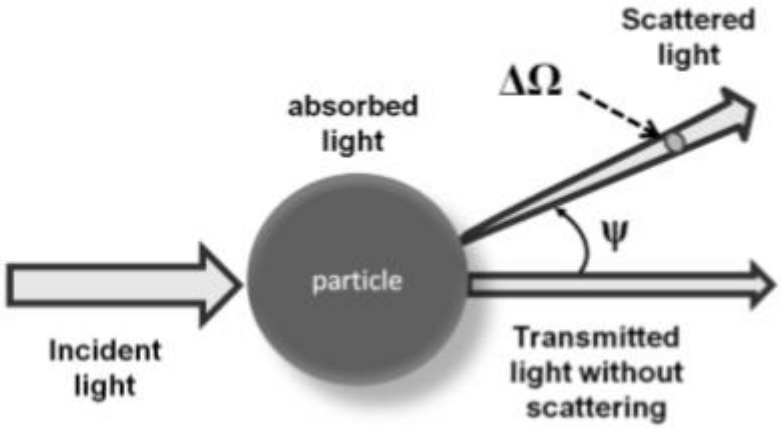

Image 1: Light propagation when encountering a particle in water [2].

We define the spectral Volume Scattering Function (VSF), $\beta(\Psi,\lambda)$, as the fraction of the incident power scattered out of the beam through an angle Ψ, within a solid angle $\Delta\Omega$ centered on Ψ. Therefore, VSF can be expressed as:

$$\beta(\theta,\lambda) = \lim_{\Delta r\to 0}\lim_{\Delta\Omega\to 0}\frac{\Delta B(\theta,\lambda)}{\Delta r\Delta\Omega} \qquad (1)$$

The VSF is used as the main Intrinsic Optical Property (IOP) for modeling the scattering in water. The integration of the VSF over all directions, gives the scattering coefficient $b(\lambda)$:

$$b(\lambda) = 2\pi\int_0^{\pi}\beta(\Psi,\lambda)sin\Psi d\Psi \qquad (2)$$

It is known that the size of particulate matter strongly affects light scattering. If the particulate size is smaller than the wavelength of light, then we have Rayleigh scattering, whereas if the particles are of the same order of magnitude or larger than the wavelength of light, we have Mie scattering. Different water types affect scattering in different ways. More specifically, since scattering in pure sea water is more pronounced at shorter wavelengths, due to the presence of salts and ions, it is well described by Rayleigh scattering [4]. In this case, both forward and backward scattering take place. The Rayleigh scattering coefficient for pure sea water, b_w is expressed as [4]

$$b_w(\lambda) = 0.005826\left(\frac{400}{\lambda}\right)^{4.322} \qquad (3)$$

In the case of an isotropic scattering, where the forward and backward scatterings have the same probabilities, the VSF is empirically expressed as [4]

$$\beta_w(\theta) = 0.06225(1+0.835cos^2\theta) \qquad (4)$$

Contrary to the pure sea, in ocean waters scattering is also caused by organic and inorganic particles that are found in the water. Scattering is also influenced by factors like temperature, pressure and salinity, as these characteristics change the refractive index of water. In such water environments, the probability of forward scattering is much higher than the probability of backward scattering and is well described by Mie scattering. In this case, the scattering coefficients for large and small particles of ocean water are expressed as [4]

$$b_l(\lambda) = 1.151302\left(\frac{400}{\lambda}\right)^{1.17} \qquad (5)$$

$$b_s(\lambda) = 0.341074\left(\frac{400}{\lambda}\right)^{0.3} \qquad (6)$$

where b_l and b_s are the scattering coefficients for large and small particles, respectively.

From the above discussion, it is concluded that both absorption and scattering impact the optical beam in an underwater environment. The sum of absorption and scattering coefficients is the extinction coefficient c:

$$c(\lambda) = a(\lambda) + b(\lambda) \qquad (7)$$

Note that a, b, and c are in units of m^{-1} [1].

The absorption, scattering, extinction coefficients as well as the volume scattering function are the main Intrinsic (or Inherent) Optical Properties (IOPs) of water. As IOPs we define the optical parameters that depend only on the composition and particulate substance present in transmission medium. They are independent of the characteristics of the light sources [2]. On the other hand, Apparent Optical Properties (AOP) are susceptible to both the medium and the geometric structure of the light, such as collimated or diffused beam. The intrinsic properties are used to calculate the link budget of the channel, while the apparent properties define the directional characteristics of the optical beam and are used to evaluate the ambient light levels for communication near the water surface [2]. The common apparent properties are radiance, irradiance and reflectance. The radiance of an area is the radiant flux emitted, reflected, transmitted or received by a given surface, per unit solid angle per unit projected area and is measured in W/(sr×m^2) [6], irradiance is the radiant flux received by a surface per unit area measured in W/m^2 [7] and the reflectance defines the water effectiveness in reflecting radiant energy at its surface boundaries and it is dimensionless or expressed in percentage values [8]. An apparent property can be derived only from regular and stable light sources. For instance, the downwelling radiance from the Sun is not an apparent property, as it may change during the day.

Due to the spectral dependence of the combination of absorption and scattering, light propagation in water displays high sensitivity in beam's wavelength. For example, transmittance can fall from almost 100% over several meters in clear ocean water for wavelengths of 400 – 500 nm to near zero for turbid waters and wavelengths bellow 300 nm or above 700 nm. It is clear from the literature that applying a single value to the extinction coefficient at a given wavelength is definitely an oversimplification and it is declared that the most suitable wavelength for high quality transmission of an optic signal varies from 400 nm to 550 nm, according to the water composition [9].

1.1.2 Sea – Air surface

In addition to the water effect on the optical beam, the light is also influenced by the water-air surface. Generally, when light propagating trough a medium encounters an interface between areas of different refractive indexes, then it is partially transmitted (refractive) and partially reflected according to Fresnel's law for dielectric mediums. In order to forecast the light's behavior at the sea-air surface, it is critical to find out the seawater refractive index, which depends on the water temperature and salinity, as well as on the beam's wavelength.

The authors in [9] propose the next model for the approximate calculation of the refractive index of seawater, n_w, which is valid for temperatures in the range 0 °C < *Temp* < 30 °C, salinities in the range 0% < *S* < 35% and optical wavelengths in the range 400 nm < λ < 700 nm:

$$n_w(S, Temp, \lambda) = n_0 + (n_1 + n_2 Temp + n_3 Temp^2)S + n_4 Temp^2 + \frac{n_5 + n_6 S + n_7 Temp}{\lambda} + \frac{n_8}{\lambda^2} + \frac{n_9}{\lambda^3} \quad (8)$$

where n_0 to n_9 are empirically verified constants. The values that have been computed vary from 1.32913, for *Temp* = 30 °C, *S* = 0%, λ = 700 nm, to 1.35093, for *Temp* = 1 °C, *S* = 34.998%, λ = 404.7 nm. Taking this into consideration, mathematical equations are derived in the paper for computing the received power and bit-error rate (BER) in line-of-sight and reflective configurations. The basic idea of reflective communication is designed in Image 2. The laser transmits, in the upward direction, a cone of light

defined by the inner angle θ_{min} and the outer angle θ_{max}. It is assumed that the sensor nodes can automatically align themselves so that the transmitter faces always upward. The light that reaches the sea surface illuminates an annular area and partially bounces back according to the water's reflectivity property. If the light is polarized with the electric field of the light perpendicular to the plane shown in Image 2, the reflection coefficient is defined as

$$R_s = \left[\frac{n_w \cos(\theta_i) - n_A \cos(\theta_t)}{n_w \cos(\theta_i) + n_A \cos(\theta_t)}\right]^2 = \left[\frac{\sin(\theta_i - \theta_t)}{\sin(\theta_i + \theta_t)}\right]^2 \qquad (9)$$

where θ_i and θ_t are the incidence and transmission angles respectively, n_w is the refractive index of water and n_A the refractive index of air. If, on the other hand, the incident light is polarized in the plane of the diagram, then the reflection coefficient is given by

$$R_p = \left[\frac{n_w \cos(\theta_t) - n_A \cos(\theta_i)}{n_w \cos(\theta_t) + n_A \cos(\theta_i)}\right]^2 = \left[\frac{\tan(\theta_t - \theta_i)}{\sin(\theta_t + \theta_i)}\right]^2 \qquad (10)$$

Polarized light propagating through the underwater channel would lose its polarization properties due to the scattering nature of the medium. Therefore, the authors assumed that the light reaching the water-air surface is totally unpolarized and thus its reflectivity is given by

$$R = \frac{1}{2}(R_s + R_p) \qquad (11)$$

Since the refractive index in the water is higher than in the air, then, if the incident angle surpasses a critical value, Total Internal Reflection (TIR) occurs and all the light is reflected back, as if the interface were a perfect mirror. The critical angle is given by the following equation:

$$\theta_c = sin^{-1}\left(\frac{n_A}{n_W}\right) \qquad (12)$$

If $\theta_{min} < \theta_c$, then TIR will not be achieved and only part of the light will be reflected back to the water. However, the optical path, and consequent attenuation, of light reflected at $\theta_{min} < \theta < \theta_c$ is shorter than $\theta_c < \theta < \theta_{max}$, so that at a specific depth below the sea surface, the light intensity distribution received by the receiver will be a complicated interplay of reflectivity and attenuation.

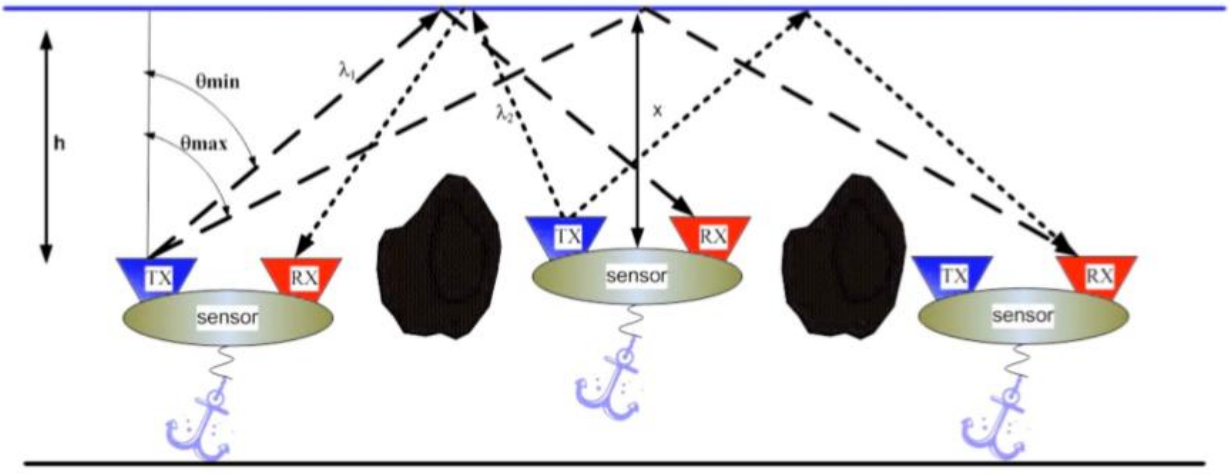

Image 2: Reflective communication scenario used in [9].

The authors have further extended the reflective configuration described above by adding the effect of waves on sea surface. According to some previous work mentioned in that paper, a very-near Gaussian Probability Distribution Function (PDF) of the surface's slope has been revealed. In those works, a Gram-Charlier series of approximate Gaussian distribution is computed in order to obtain an analytical model for the wave slope density distribution function. However, the wave slope PDF derived from experimental data differ from the Gaussian model in a few significant ways that reveal information regarding the surface contour. The two primary indicators of the deviation of the sea surface slope PDF from the classic Gaussian form are expressed as skewness and kurtosis coefficients. Skewness is notable in the downwind direction, but negligible in the crosswind direction. In [9], the researchers do not correct for skewness and kurtosis because of the symmetry of the omnidirectional transmission. They also assume that the mean slope angle is zero, although they declare that it has been found that this mean value is near zero in experimental upwind and downwind measurements. For gaining a better understanding of the angular spread of a transmitted laser beam reflected by the surface, the authors performed Monte Carlo simulations, where they launched 10^5 photons at angles between 1^o and 90^o with respect to the sea surface. They also used Equations 9–12 in order to compute the angle of reflection from the normal sea surface. For the sea surface slope, the PDF is derived using the first term of the Gram-Charlier series and is shown in Image 3 for wind speeds of 3.98, 8.58 and 10.2 m/s.

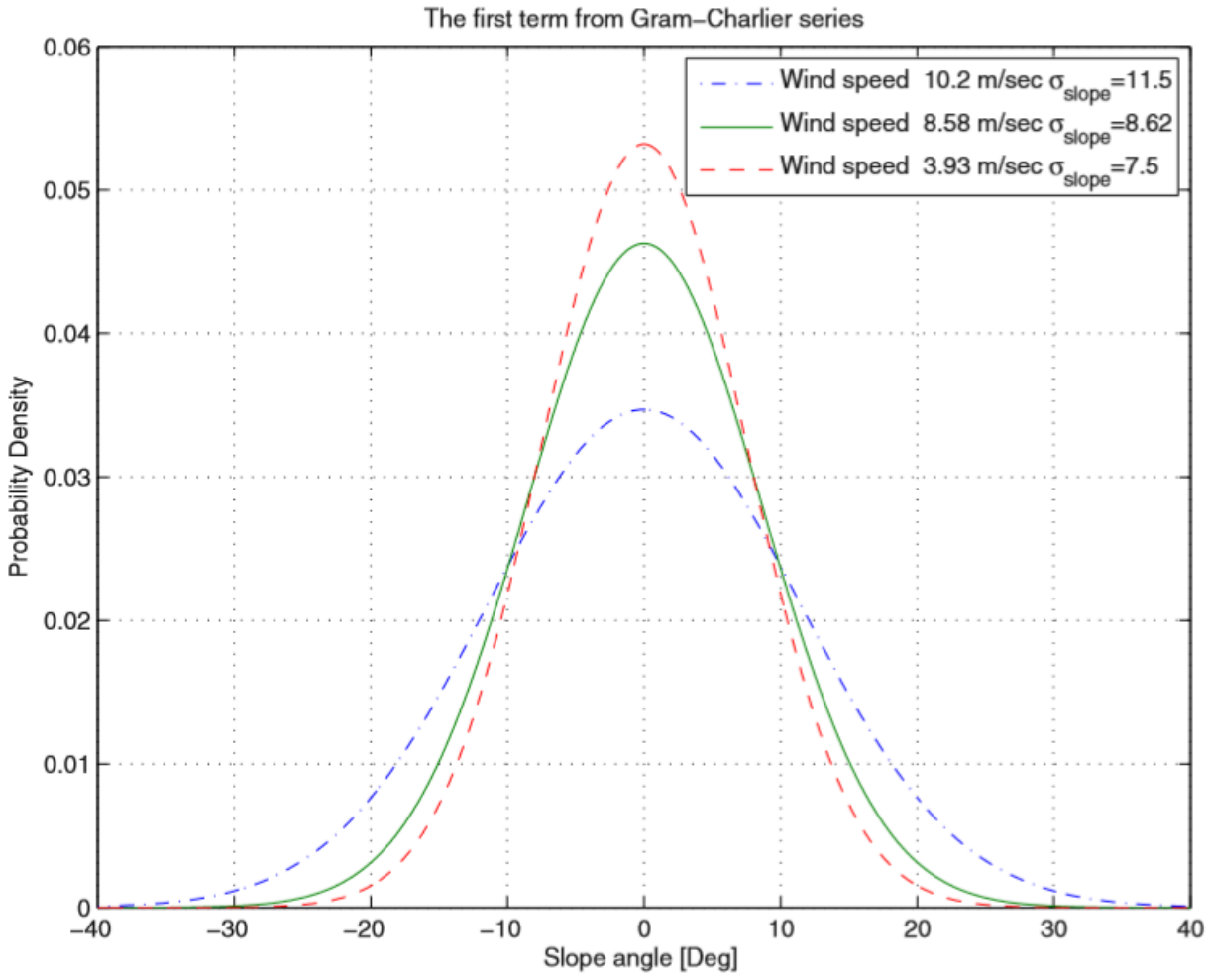

Image 3: Graph showing PDF of surface slope angle for three wind speeds [9].

The data used in the simulations are shown in Table 1.

Table 1: Parameters used in numerical calculations for [9].

Parameter	Typical Value
Extinction coefficient (m^{-1}) Clear ocean	0.1514
Temperature (^oC)	10
Salinity	3.5
Refractive index	1.33643
Critical angle (degrees)	48.44
Transmission wavelength (nm)	532
Optical efficiency of transmitter	0.9
Optical efficiency of receiver	0.9
Average transmitter power (W)	0.1
Pulse duration (ns)	1
Data rate (Mbit/sec)	0.5
Receiver aperture area (m^2)	0.01
Laser beam divergence angle (degrees)	$\theta_o = 68$
Transmitter inclination angles (degrees)	$\theta_{min} = 0$, $\theta_{max} = 68$
Dark counting rate (MHz)	1
Background counting rate (MHz)	1
Counting efficiency (%)	16
Transmitter depth – h (m)	20
Receiver depth – x (m)	20

The received power at different reflected angles is illustrated in Image 4 and Image 5, where Image 4 is for smooth sea surface while Image 5 is for wavy sea surface. In Image 4 we note that bellow the critical angle, only a little amount of light is reflected by the sea surface, but above the critical angle the transmitted photons are totally reflected at the precise angle predicted. On the other hand, the light is spread to more reflected angles for the wavy sea surface, as shown in Image 5. In this case, the wind speed was 11.5 m/s. More specifically, when the sea surface is modeled as non-smooth, some light is back-reflected due to the local surface slope. The forward-reflected light propagates mainly at angles close to the right-angle-complement of the incident angle, but a considerable angular spread occurs. Except for the obvious contrast in the variation of the arrived angle, it is also noticed that the angular spread results in considerable loss in received optic power when the reception angle of the receiver is limited. Photons arriving at different angles will have traveled through different optical paths resulting in multipath phenomena and further reduced power reception.

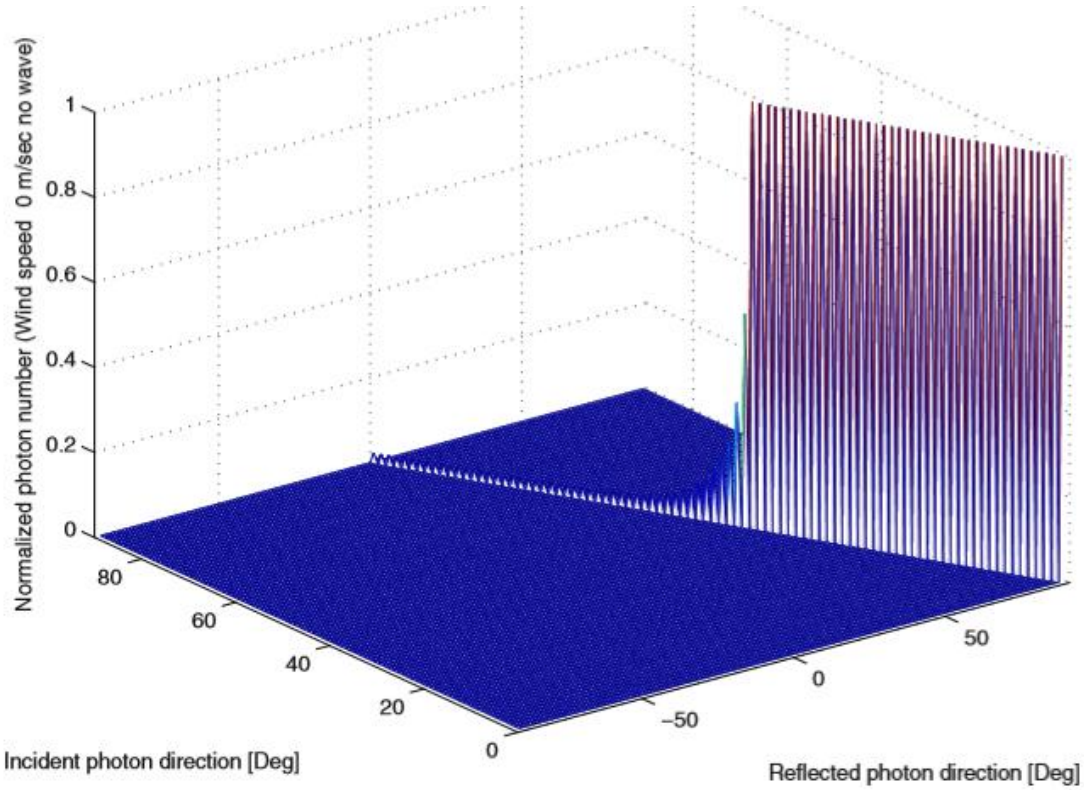

Image 4: Graph showing angular distribution of power reception resulting from reflection from a smooth sea surface. Incident photon direction is measured from seabed surface, reflected photon direction is measured from sea-surface normal [9].

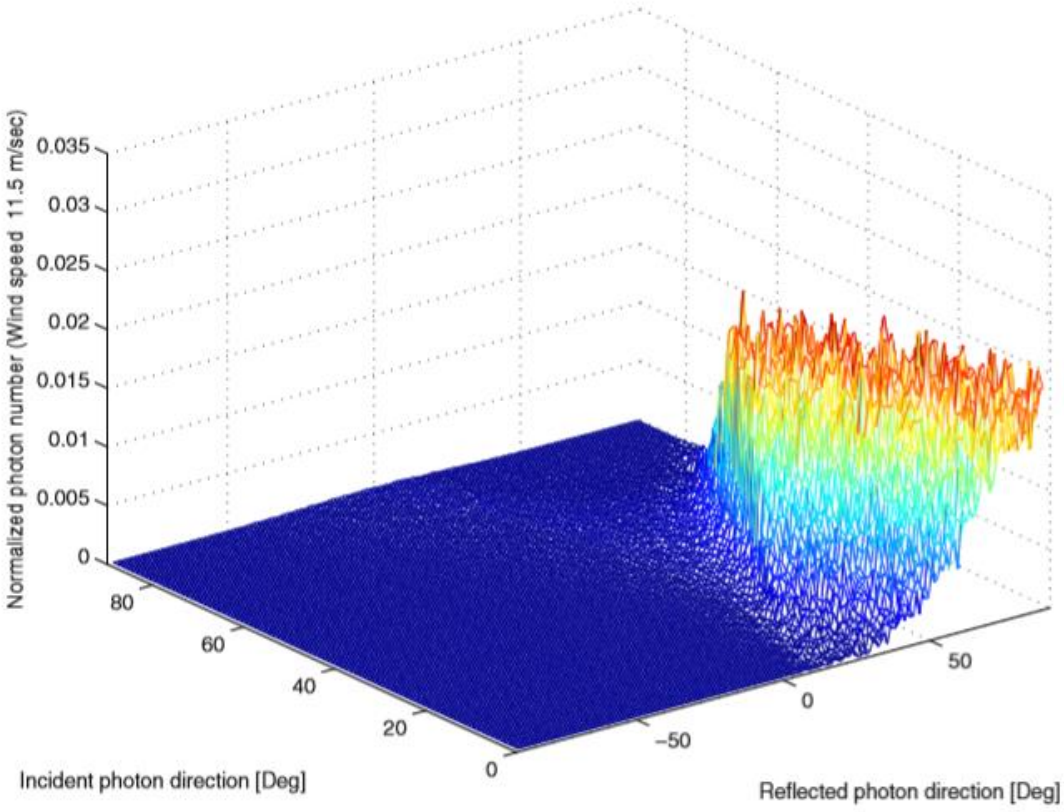

Image 5: Graph showing angular distribution of power reception resulting from reflection from a simulated wavy sea surface. Incident photon direction is measured from seabed surface, reflected photon direction is measured from sea-surface normal [9].

1.1.3 Water particles

Absorption and scattering are affected not only from the water molecules, but also from the different particles in solution or in suspension in water. The spectral absorption and scattering coefficients *a* and *b*, respectively, can be calculated by adding the contribution of each class of particles to the corresponding coefficients of the pure sea water. An example of such a particle is phytoplankton, which determines the optical properties of most oceanic waters, as their chlorophyll and related pigments heavily absorb light in the blue and red spectral ranges. In [1] it is stated that we can also use the chlorophyll concentration *C* (in $mg.m^{-3}$) as the free parameter to calculate *a* and *b*, based on bio-optical models such as those proposed by Haltrin and Kattawar [9] and Gordon and Morel [10]. The authors present the curves of *a*, *b*, and *c*, as a function of wavelength λ using the model of Gordon and Morel for two chlorophyll concentrations of 0.31 and 0.83 $mg.m^{-3}$ (Image 6). It is noticed that an increase in *C* has little influence on *a*, but it considerably affects *b*.

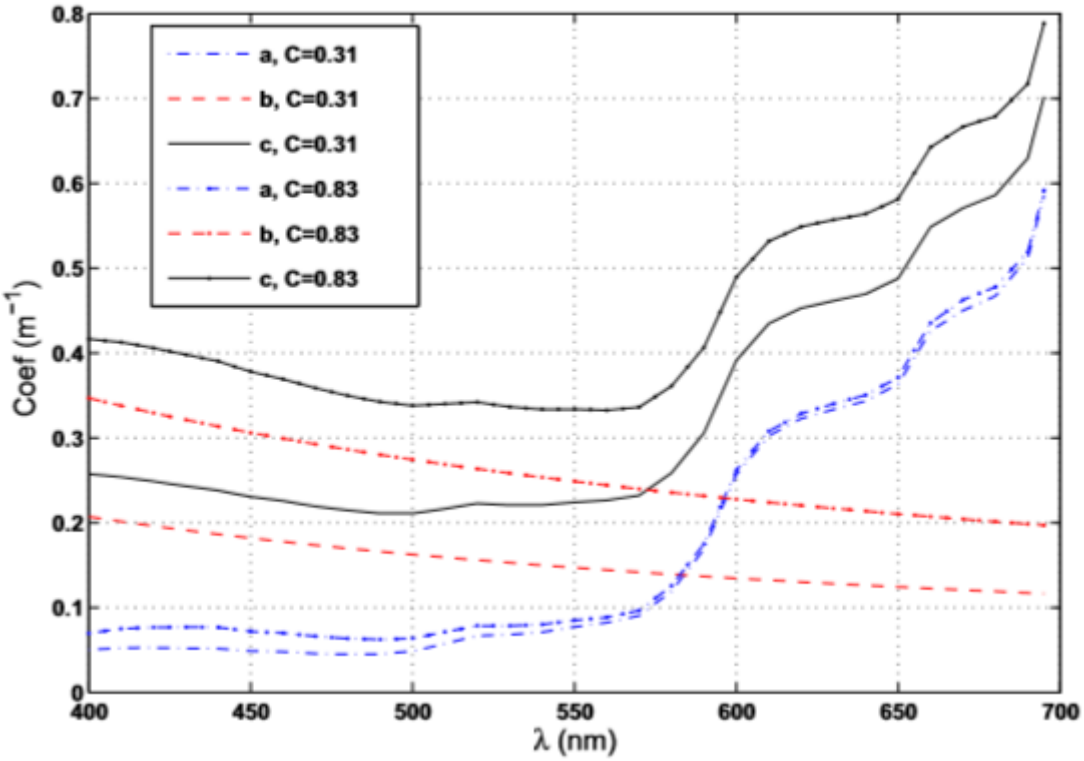

Image 6: Absorption (a), scattering (b), and extinction (c) coefficients as a function of wavelength for two chlorophyll concentrations (in mg.m^{-3}) using the model of Gordon and Morel [2].

The absorption effect of pure seawater is mainly induced from two sources: the water molecules and dissolved salt in water, such as NaCl, MgCl2, Na 2SO4, CaCl2, and KCl [2]. Pure seawater is absorptive, except around the blue-green area of the visible light spectrum. The corresponding absorption spectrum of pure seawater is shown in Image 7.

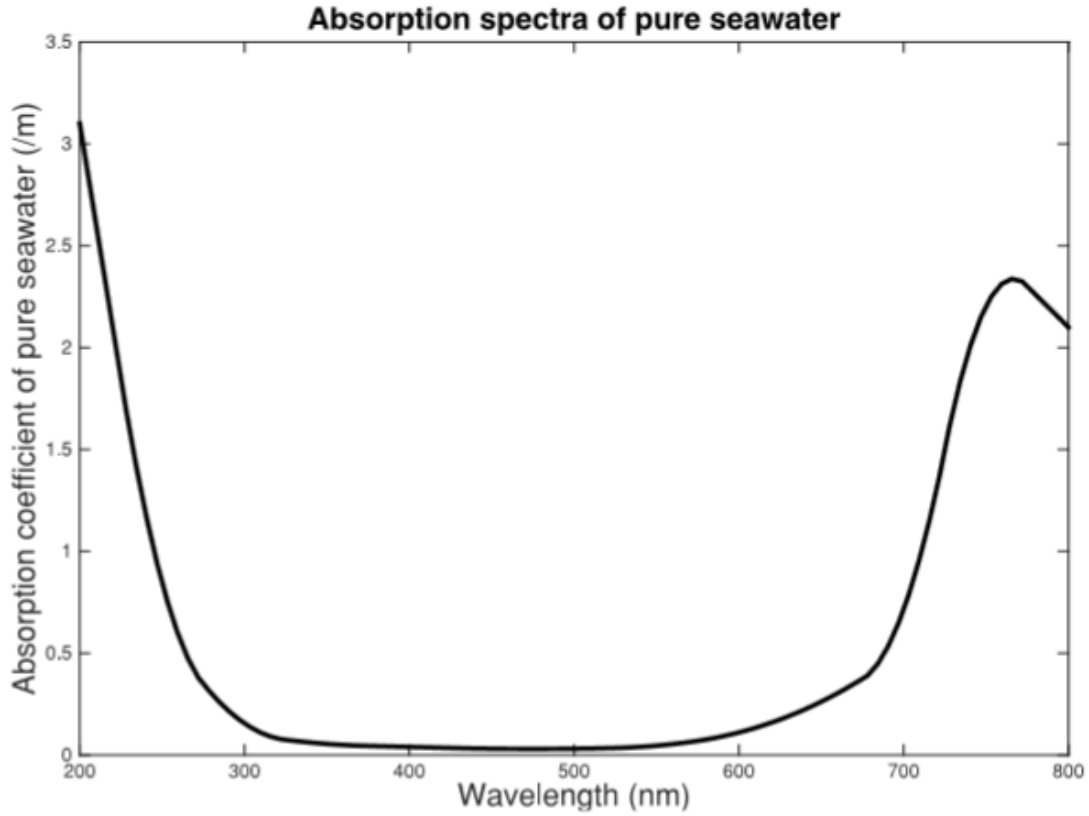

Image 7: Absorption spectra of pure seawater [2].

Inside the water there is always some amount of gelbstoff, which contains decaying marine matter or yellow substance from dead-plant tissues, with dimension smaller than 0.2 mm [2]. Gelbstoff is often called as CDOM and it generally shows lower concentration in open waters and higher concentration in coastal waters. CDOM produces humic and fulvic acids that present high absorption around blue region (420 nm – 450 nm) and thus make yellow-red color more dominant in terms of absorption. This is also depicted in Image 8, where it is shown that the CDOM is highly absorptive to blue wavelengths and less absorptive to yellow and red light.

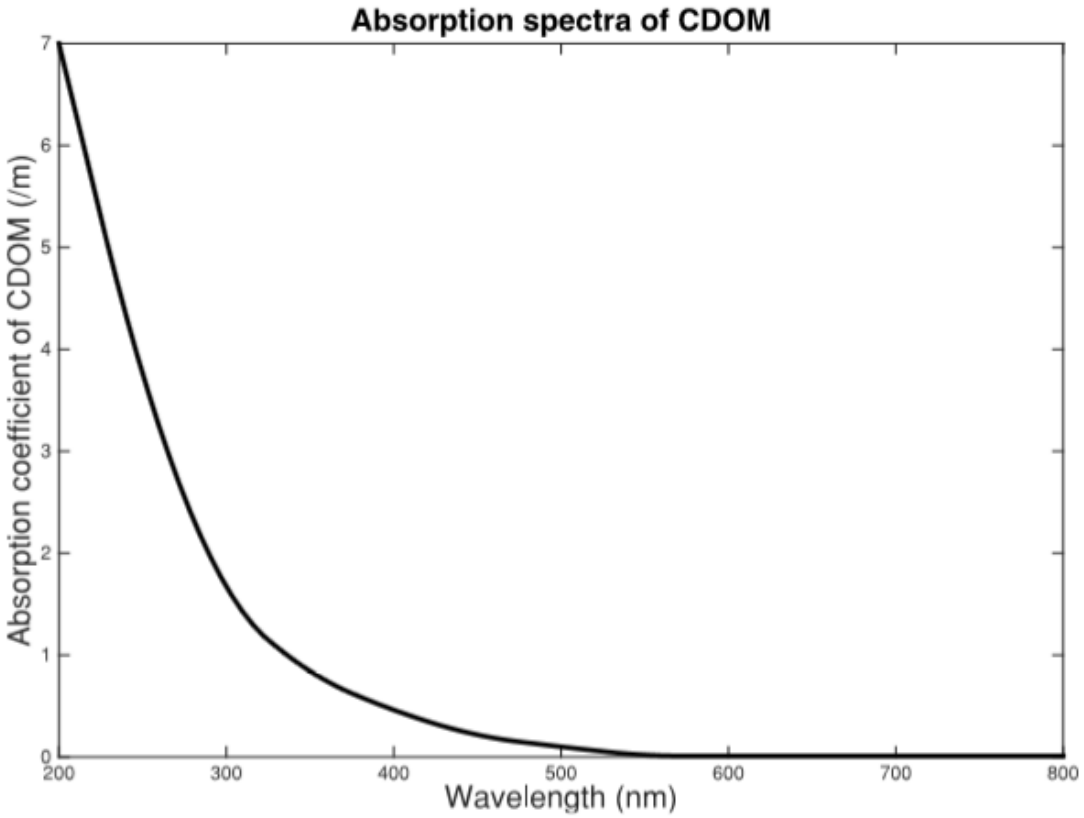

Image 8: Absorption spectra of CDOM [2].

Phytoplankton, which was mentioned in the first paragraph of this section, consists of microscopic organisms that are located only on the part of the ocean where sunlight can propagate [4]. This part can be from 50 m to 200 m in clear ocean water, up to 40 m in continental shelves and 15 m in coastal water [5]. Phytoplankton includes colored pigment due to chlorophyll, carotenoids, phaeophytins, chlorophillides and phaeophorbides, which absorb large amount of optical light. In addition to that, phytoplankton affects the absorption mainly because of the photosynthesis of chlorophyll. In other words, chlorophyll is the most important source of absorption. High concentrations of chlorophyll are commonly noticed along the equator, on the coastlines (especially east-facing) and in high latitude oceans. This is the reason why areas with high organic matter, such as near coasts, seem to be yellow-green in color. In these areas, the chlorophyll concentration may be up to 60 $mg.m^{-3}$, while for open ocean it is reduced within the range 0.01 – 4.0 $mg.m^{-3}$ [5]. As stated in [3], different phytoplankton species affect the absorption in different manners. Image 9 shows a typical absorption coefficient profile common to all species. It is noticed that the absorption coefficient due to phytoplankton is high in the 400 – 500 nm region and has an additional peak around 660 nm. In conclusion, it is accepted that while CDOM absorbs more at shorter wavelengths, phytoplankton absorbs strongly in the blue and red wavelengths, on the other hand, mainly because of the chlorophyll concentration. [4]

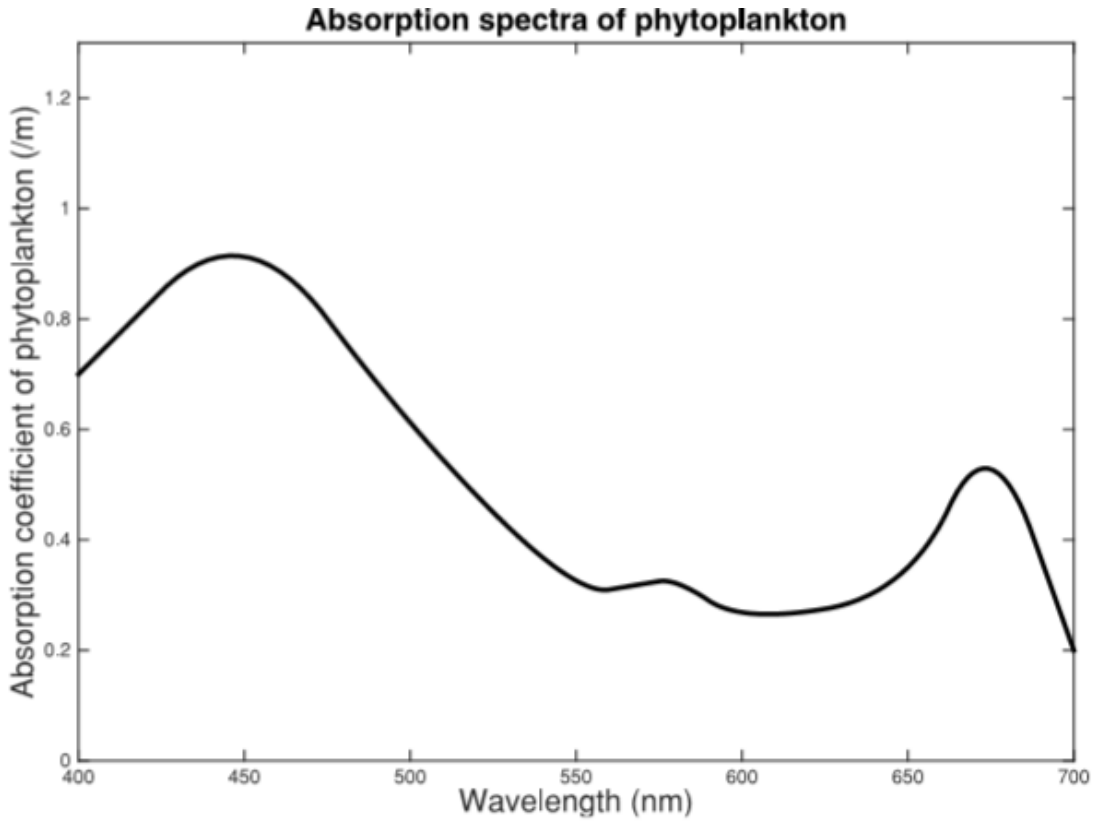

Image 9: Absorption spectra of phytoplankton [2].

Lastly, non-algal material (also referred as detritus) includes living organic particles such as bacteria, zooplankton, detrital organic matter and suspended inorganic particles like quartz and clay. As these substances have similar absorption behavior, they are usually grouped together in the literature [2]. Image 10 shows an absorption curve similar to that of CDOM (Image 8).

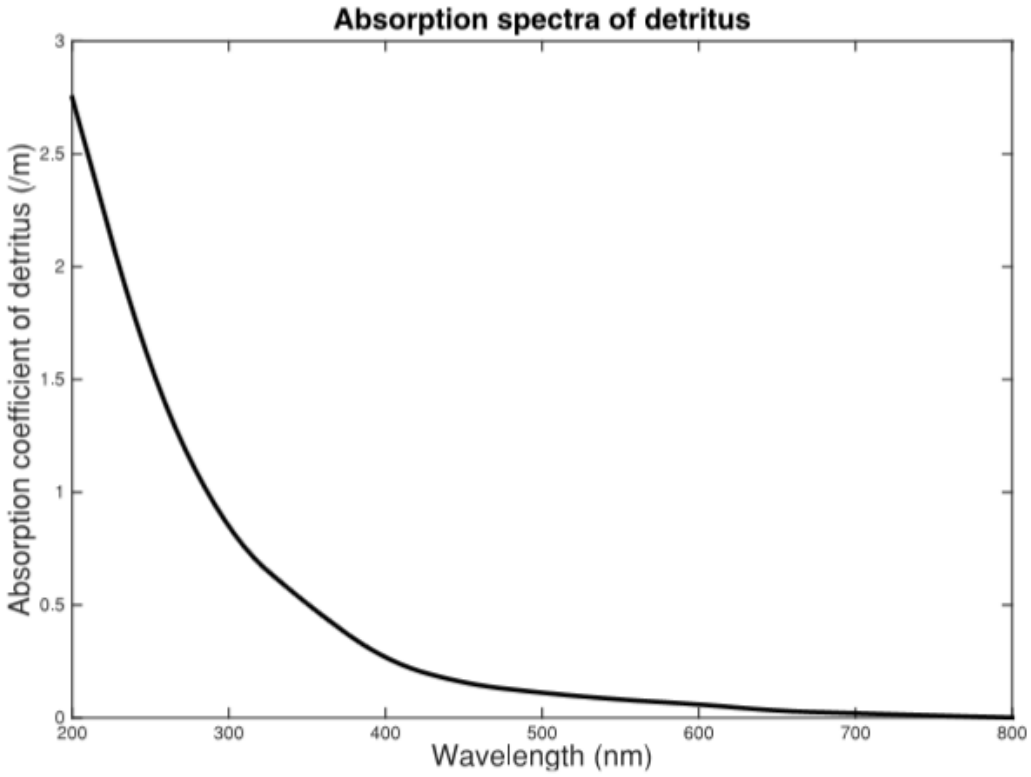

Image 10: Absorption spectra of detritus [2].

In summary, the total absorption in sea water is caused by intrinsic absorption from inorganic material, such as water molecules, suspended particles and dissolved salts, and by absorption from organic molecules, like phytoplankton and gelbstoff (CDOM). Therefore, the overall absorption coefficient in sea water is consisted of four separated factors and is defined as [4]

$$a(\lambda) = C_w a_w(\lambda) + C_{phy} a_{phy}(\lambda) + C_{CDOM} a_{CDOM}(\lambda) + C_d a_d(\lambda) \qquad (13)$$

where C_x is the concentration of inorganic and organic matters, $a_w(\lambda)$ is the absorption coefficient of pure water, $a_{phy}(\lambda)$ of phytoplankton, $a_{CDOM}(\lambda)$ of CDOM and $a_d(\lambda)$ of detritus mater.

Image 11 shows the combined absorption spectra of open ocean and coastal waters. In open oceans the chlorophyll, humic and fulvic concentration (produced by CDOM) is low and thus the absorption spectrum is mainly affected by the attenuation that is caused by pure water. In this case, the minimum attenuation window is located in the spectrum around 400-500 nm, i.e. in the blue-green region of visible light. On the other hand, chlorophyll and CDOM concentration is much higher in coastal regions. As a result, the minimum absorption window is shifted between 520 and 570 nm, i.e. in yellow-green spectrum.

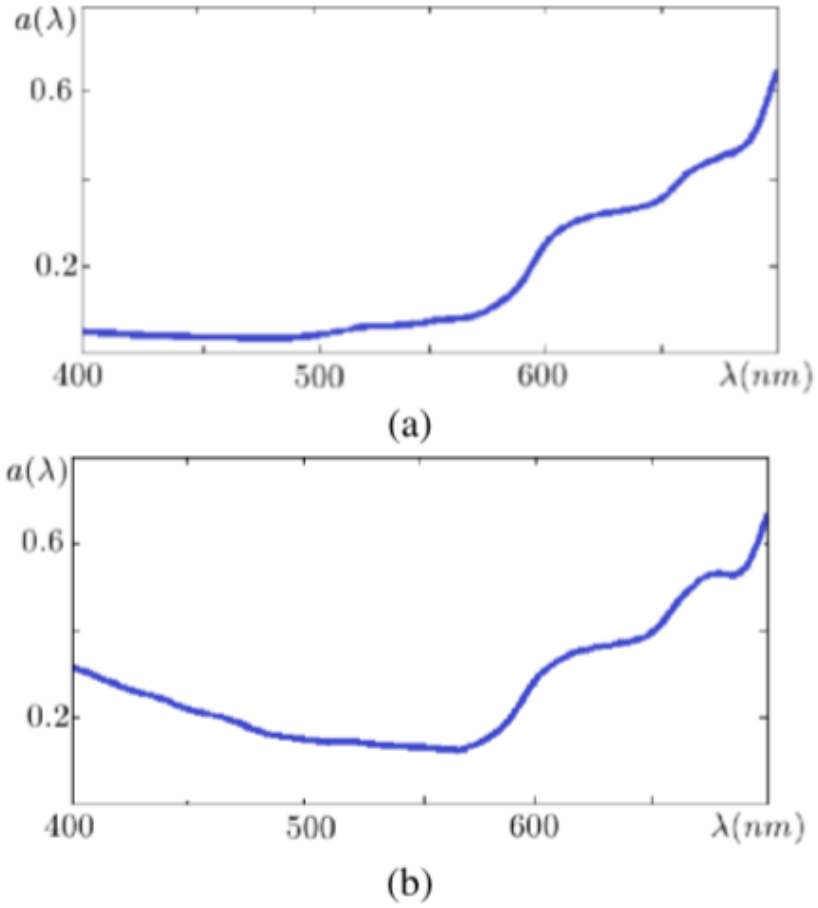

Image 11: Combined absorption spectra of different water types (a) open ocean and (b) coastal waters (absorption coefficients in m^{-1}) [4].

Since there are several factors that affect the absorption in underwater environments, the minimum attenuation window is not the same among different water types. The most suitable transmission wavelengths for the various water types, in accordance with the chlorophyll concentration, are presented in Table 2.

Table 2: Ideal transmission wavelength for different water types [4]

Water Type	Chlorophyll Concentration	Operating Wavelength
Pure sea / clear ocean	Less	450 – 500 nm (blue – green)
Coastal Ocean	High	520 – 570 nm (yellow – green)
Turbid Harbor	Very high	520 – 570 nm (yellow – green)*

'' implies performance limited by absorption and scattering coefficients*

1.1.4 Water types

Taking into consideration that underwater matters and water quality vary from one place to another, four main water types are usually examined in the literature [1]:

- **Pure sea waters**: In these water types, the major limiting factor is absorption, which increases with an increase in wavelength. In lower wavelengths, the overall attenuation is again dominated by absorption, even though scattering has an important impact too. To put it differently, the red wavelength suffers from higher attenuation than blue light and this is the reason why the deep clear ocean water seems to be rich with blue color. The absorption in pure sea waters is defined as the sum of absorption in pure water (where there is no suspended particulate matter) and absorption by salts in pure salt water. Absorption by salts is assumed to be negligible in the visible spectrum (400 - 700 nm). The absorption coefficient in pure sea water is given as

$$a_{seawater}(\lambda) < K(\lambda) - \frac{b(\lambda)}{2} \qquad (14)$$

  where λ is the operating wavelength, K is the diffuse coefficient and b is the scattering coefficient [4]. In this case, the low b (at about 0.003 m^{-1}) results in small forward scattering angle, making the beam propagate approximately in a straight line.
- **Clear ocean waters**: They have a higher concentration of dissolved particles, like dissolved salts, mineral components and colored dissolved organic matter, that affect scattering.
- **Coastal ocean waters**: They have a much higher concentration of dissolved particles, like planktonic matters, detritus and mineral components, which influence even more the absorption and scattering coefficients and increase the turbidity level.
- **Turbid harbor waters**: They have the highest concentration of dissolved and suspended matters. Thus, this water type restricts the propagation of optical signals, as the impact of absorption and scattering is much higher.

Typical values of a, b and c coefficients in sea water are shown in Table 3 for 532 nm. These are the values that we consider in our work.

Table 3: Typical Coefficients for the water types under study and for wavelength λ = 532 nm [1].

Water Type	C (mg/m^{-3})	a (m^{-1})	b (m^{-1})	c (m^{-1})
Pure sea	0.005	0.053	0.003	0.056
Clear ocean	0.31	0.069	0.08	0.15
Coastal	0.83	0.088	0.216	0.305
Turbid	5.9	0.295	1.875	2.17

1.1.5 Water Turbulence

In UOWC we define as turbulence the event that makes water experience rapid changes in the refractive index [2]. This occurs due to ocean currents which result in the sudden variations of the water's temperature, salinity and pressure. Moreover, underwater optical turbulence, also called scintillation, can lead to important degradation to the system's performance. However, due to the dynamic nature of underwater environment, there are no widely accepted turbulence models for UOWC systems. The majority of the studies on UOWC channel modeling are focused on presenting an accurate description of absorption and scattering coefficients, but the effect of underwater optical turbulence is often not taken into consideration. In our study, we also ignore the impact of water turbulence.

As for the existed UWOC studies in turbulence modeling, they commonly base their research on existed results for the atmospheric optical turbulence channel models in free-space optical communications. Because of the similarity between underwater optical turbulence and atmospheric optical turbulence, a number of works directly apply or modify the known models for the atmospheric optical turbulence. For example, the classical Kolmogorov spectrum model of Free-Space Optical (FSO) is commonly applied in the literature for underwater environment and is expressed as [4]

$$\Phi_n(\kappa) < K_3 \kappa^{-11/3} \qquad (15)$$

where $K_3 = \chi \varepsilon^{-1/3}$ is a parameter similar to C_n^2 for FSO communications and it indicates the underwater optical turbulence strength, χ is the dissipation rate of temperature or salinity variances, ε is the kinetic energy dissipation rate (typical ranges from 10^{-3} to 10^{-11} m^2s^{-3} in natural water) and κ the scalar spatial frequency (in rad/m). The received intensity fluctuations can be described by lognormal distribution, because of the aperture averaging effect due to larger aperture dimension of the optical lens (in front of detector) than the coherence length of the light [4]. The coherence length refers to a distance in which it is very likely that two fields will constructively or destructively interfere. As a result, there are may be fading events due to a disturbance of the refractive index inside the coherent wavelength. If the receiver's area is wide, it receives the average fluctuations (aperture averaging effect) as the entire surface of the receiver is integrated during the data reception, e.g. during a pulse. In this way, the effect of rapid and intense fading, owed to small coherent wavelengths, is mitigated. As a consequence, the receiver with the wide detecting surface, in general, will face milder fading which follows the log-normal distribution.

For example, the authors in [2] propose an underwater optical turbulence model, which is based on the classical lognormal turbulence model used in FSO communication:

$$f_I(I) = \frac{1}{\sqrt{2\pi}\sigma_t I} e^{-\frac{(\ln I - \mu)^2}{2\sigma_t^2}}, I > 0 \qquad (16)$$

where I is the received optical irradiance, μ is the mean logarithmic light intensity and σ_t^2 is the scintillation index. Nevertheless, this model has not been verified by experimental measurements and thus cannot be considered accurate.

For more works related to this issue, the reader is advised to study the references mentioned in [2] and [4].

1.1.6 Water Depth

The physical properties of water vary not only in different geographic locations but also in the same location but in different depths. The upper layer is named the euphotic zone because significant amount of sunlight reaches this zone. Consequently, this zone consists of large photosynthetic life, as chlorophyll is the main component of phytoplankton. The depth of this zone varies according to the type of water. In clear ocean water this zone is up to 200 m deep, while in continental shelves and coastal waters the zone's depth is 40 m and 15 m, respectively [4]. The variation of chlorophyll with depth creates a skewed Gaussian profile from surface to the bottom. The peak on skewed Gaussian chlorophyll-depth profile is called the deep-chlorophyll maximum. This is the point where the attenuation coefficient reaches its maximum value as shown in Image 12. The zone located a few meters below the euphotic zone is called dysphotic

zone, as the sunlight is not sufficient for photosynthetic development. Further below this zone we have the aphotic zone, where no light ever reaches these depths. Each of these zones has its own physical characteristics and optical properties. Our study is focused on the euphotic and disphotic zone and all the characteristics and optical properties that are taken into consideration are those of this topmost zone.

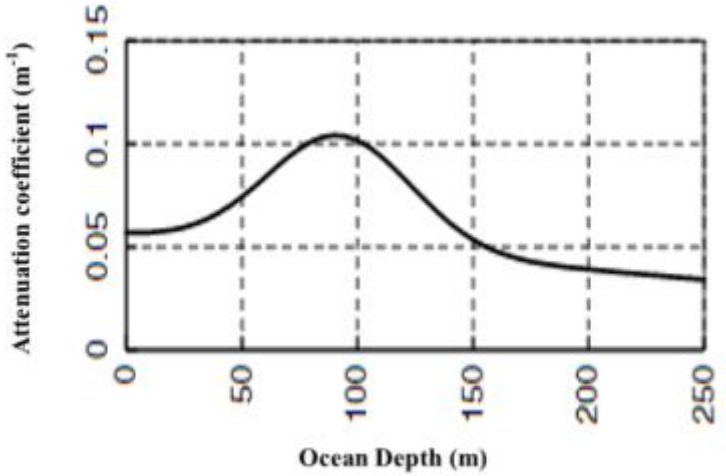

Image 12: Attenuation curve with increasing optical depth [4].

1.1.7 Background Noise

Another physical aspect that is present in underwater environments and must be taken into consideration is the background noise. Noise greatly depends on the operating wavelength and the geographical location. Normally, in deep ocean waters the background noise is less than in harbor waters, where there is some amount of manmade noise. Typically, the noise sources in underwater environment are described as continuous spectrum with Gaussian profile. The main sources of background noise are [4]:

1. diffused extended background noise,
2. background noise from the Sun or other stellar or point objects and
3. scattered light collected by the receiver.

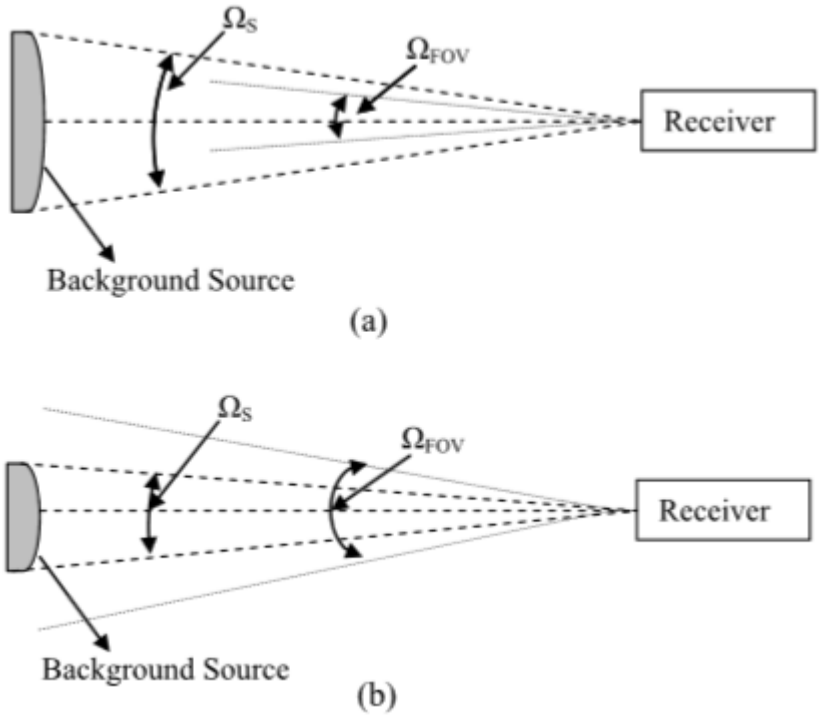

Image 13: Geometry of (a) extended source when $\Omega_{FOV} < \Omega_S$ and (b) stellar or point source when $\Omega_{FOV} > \Omega_S$ (Ω_{FOV} is the solid angle of receiver field-of-view and Ω_S is the solid angle field-of-view of the source) [4].

Image 13: Geometry of (a) extended source when $\Omega_{FOV} < \Omega_S$ and (b) stellar or point source when $\Omega_{FOV} > \Omega_S$ (Ω_{FOV} is the solid angle of receiver field-of-view and Ω_S is the solid angle field-of-view of the source) shows the geometry of point and extended sources in relation to the receiver. In the euphotic zone of the ocean, meaning at the depth of tens of meters, the dominant contributor of background noise is solar interference. On the contrary, at larger depths, the main source of optical noise is biological luminance. The peak of the biological luminance is centered on the blue-green band and potentially increases the noise existing in the system. The total background noise is given as [4]

$$P_{BG} = P_{BG\_solar} + P_{BG\_biological} \quad (17)$$

In the last formula, $P_{BG-solar}$ is the solar background noise power and is expressed as

$$P_{BG\_solar} = A_R(\pi FOV)^2 \Delta\lambda T_F L_{sol} \quad (18)$$

where A_R is the receiver area, $\Delta\lambda$ the optical filter bandwidth and T_F the optical filter transmissivity at the receiving side. The solar radiance, L_{sol} (W/m^2) is defined as

$$L_{sol} = \frac{ERL_f e^{-Kd}}{\pi} \quad (19)$$

where E is the downwelling irradiance (W/m^2), R is the underwater reflectance of the downwelling irradiance, L_f is the factor that describes the directional dependence of underwater radiance, K is the diffuse attenuation coefficient and d is the underwater depth. For instance, if the optical signal has a wavelength of 532 nm, then we will have E = 1440 W/m^2, R = 1.25% and L_f = 2.9 in the horizontal direction [4]. The noise from biological luminance is given as

$$P_{PG\_biological} = \frac{2hc^2\gamma A_R(\pi FOV)^2\Delta\lambda T_A T_F}{\lambda^5\left[e^{(hc/\lambda kT}-1\right]} \quad (20)$$

where c = 2.25257 × 10^8 is the speed of light in water, h is the Planck's constant, T_A = exp(−τ_0) is the transmission in water, k is the Boltzmann's constant, and γ = 0.5 is the radiant absorption factor. By applying a narrow band spectral filter in front of the receiver, it is possible to reduce the background noise.

In [14] the authors have studied the scenario of transmitting data in underwater sensor networks located in coastal waters. They aim at reducing the environmental noise, mostly induced by the sunlight inserted in the underwater network. Thereby, the sensors transmit optical beams in the ultraviolet (UV) solar-blind spectrum, where almost no background illumination exists. The paper presents a comparison between optical signals in UV-C spectrum (λ = 270 nm) and in green spectrum (λ = 520 nm). It is concluded that in turbid waters, the operation at UV wavelengths provides similar performance as operating in blue or green spectrum, making the UV wavelengths an attractive alternative solution for sensor networks in such environments. Moreover, taking into account the cost of each implementation, it is stated in the paper that we can benefit from the use of sensors operating in the UV spectrum range, as these sensors are less expensive. In Table 4, the water characteristics and the system performance for each of the two scenarios are presented.

Table 4: Data on optical properties of seawater, solar radiance at the Earth's surface and resultant maximum transmission range for subsea FSO system with a BER of 10^{-4} at four different data rates, two wavelengths and three ocean types [14].

Wavelength (nm)	Extinction coefficient (m^{-1})	Solar radiation at the Earth's surface [W/(cm μm)]	Maximum transmission range for BER < 10^{-4} (m) for four data rates			
			100 bps	10 kbps	1 Mbps	100 Mbps
270	2.65	0.00035	16.40	14.74	13.10	11.46
520	Clear ocean: 0.15		257.5	228.2	199.4	170.7
	Coastal ocean: 0.30	0.12	133.1	118.5	104.0	89.7
	Harbor water: 2.19		19.96	17.95	15.95	14.00

Apart from the background noise, there are more sources of noise that can affect the communication system. Some of those noises are photodetector noise (detector dark current noise), preamplifier noise, shot noise as well as thermal noise. Furthermore, back-scattered light, which is radiated by the medium, also adds to the background noise. An ideal optical system would be an adaptive one, where the amount of background light is minimized by reducing the overall Field of View (FOV), while in the same time the amount of desired captured signal energy is maximized.

1.1.8 Multipath interference and dispersion

Like in acoustic communication, multipath interference can be also present in optical underwater channel, when an optical signal reaches the detector after interacting with multiple scattering objects or multiple reflections from other underwater bodies. In the end of the signal transmission the waveform will be spread in the time domain (time spreading) and therefore the data rate will decrease due to ISI. Nonetheless, compared

with acoustic communication, the effect of multipath interference in UOWC is not so straightforward due to the very high speed of light. The system specifications and the propagation environment determine the occurred amount of multipath interference. In shallow water environments, the optical waves that reflect from the surface or the bottom produce multiple copies of the signal at the receiver, while in deep oceans, these surface and bottom reflections can be ignored. To reduce the interference, the receiver applies advanced signal processing techniques, such as channel equalization and adaptive optics. Therefore, it is essential to carefully characterize the underwater optical channel, in order to be able to choose the best fitted system design parameters for a reliable and high quality optical link. It has been proven that, except for highly turbid environment, the channel time dispersion can be neglected when working over moderate distances [4]. Moreover, spatial diversity can also help in eliminating the effect of multipath interference by partially compensating for ISI degradation, especially for low data rates. Spatial diversity has been used successfully in wireless communications and it is a scheme that uses two or more antennas to improve the quality and the reliability of a wireless link. In underwater communications, two or more transmitters and/or receivers could be used to achieve a desired diversity level [15]. However, the performance is degraded at high data rates, especially when the Signal to Noise Ratio (SNR) is high.

1.1.9 Physical Obstructions

If the optical beam is very narrow, any living organism such as school of fish or marine animals will cause temporary signal loss at the receiver. Therefore, it is necessary to apply appropriate error correction and signal processing techniques as well as redundancy measures to ensure re-transmission of lost data. The two most broadly used error correction techniques in underwater environment is Automatic Repeat Request (ARQ) and Forward Error Correction (FEC). ARQ initiates the re-transmission of data when the data are not received within a predefined time period. FEC performs source coding, where redundant bits are encapsulated with data bits, in order to strengthen the robustness of the message. A combination of ARQ and FEC, referred as hybrid ARQ, is also used for increasing the UOWC system's reliability. Additionally, signal processing techniques are demonstrated for improving the quality of the optical link and making the system more robust against physical obstructions. Finally, the underwater communication system can benefit from the implementation of a hop-to-hop communication network [4].

1.2 Underwater Wireless Communication – state of the art

Underwater communication has a long history which starts with Leonardo da Vinci's observation: "If you cause your ship to stop, and place the head of a long tube in the water and place the outer extremity to your ear, you will hear ships at a great distance from you" [4]. Even though this was first mentioned in 1490, research in sonar systems started to be largely exploited only during World War I, when Paul Langevin invented a device for detecting the noise from moving submarines in 1915. The first useful device for underwater communication was the underwater telephone, an acoustic device developed in 1945. The advent of the computer during World War II and the Cold War leaded to great advances in submarine communication systems. Later on, RF and optical signals were studied in order to deal with the drawbacks or enhance the performance of acoustic communications. These wireless communication types are presented in the current section.

1.2.1 Acoustic Underwater Communication

Among the three types of waves, namely acoustic, RF and optical, the acoustic waves are preferred as the primary carrier for underwater wireless communication due to their relatively less absorption and long coverage distance. [4] The velocity of acoustic waves in the ocean is approximately 1500 m/s and thus, communications over long distances suffer from large latency. For example, the system presented in [16] achieves data rates of about 20 Kbps for 1 km distance in deep ocean, while the rate is reduced to about 300 – 500 bps for distances up to 100 km in shallow water and 200 km in deep ocean. This high latency in long ranges creates problems in synchronization as well as in applying multiple access protocols.

The first underwater audio communication was implemented in United States and it utilized a Single Side-Band (SSB) suppressed carrier amplitude modulation at carrier frequencies between 8 and 15 kHz using simple voice band and pulse shaping filters [4]. The received signal had poor quality and required the ability of human ear and brain to detect and process the distorted speech. With the progress of digital communication in 1960, the rate and operational range were relatively improved.

In [16] the researchers have used multipath compensation techniques, improving the system's throughput. Over the years, there have been designed many sophisticated methods for channel estimation and several algorithms have been presented for increasing the effectiveness of underwater acoustic communication. Moreover, Orthogonal Frequency Division Multiplexing (OFDM) has been broadly deployed in underwater acoustic communication, in order to reach high data rates without the need of complex equalizers [4].

However, regardless of the astonishing technological advances, the underwater acoustic communication still has to overcome a variety of obstacles in order to achieve really effective communication. The main reason for this is the nature of the underwater environment itself, as it is far more vibrant and challenging than it seems. Firstly, it is impossible to design a typical system of underwater acoustic channel, which would work in any environment. In other words, a system designed to operate in one environment, for example shallow water, may fail in another environment, for instance in deep ocean. Moreover, there are three main factors characterizing these waves, namely frequency dependent attenuation, time varying multipath propagation and high latency. The multipath phenomenon causes delay spread, which is around 10 ms, but it can be as large as 50 to 100 ms. These values of delay spread lead to ISI with values between 20 and 300 symbols at a data rate of 2 – 10 kilo-symbols per second and thus, they restrict the data transmission speed [4].

To sum up, acoustic communication is the most widespread method for underwater wireless communication and it can achieve transmission ranges of hundreds of kilometers. Nonetheless, it provides limited data rates due to the severe, frequency-dependent attenuation and pulse-spread created by the sea surface. In practice, most acoustic links operate in half-duplex mode and in a sensor network, sensor to sensor communication remains an unsolved issue, thus restricting the network topologies to star configurations with a central base station [9]. Additional drawbacks of acoustic UWC are time-varying multipath interference, shadow zones, bubble-cloud attenuation near the surface [9] and potential harm to marine mammals.

1.2.2 Radio-Frequency Underwater Communication

In order to further improve the accomplished data rates, several works use RF waves in underwater wireless communication, since they provide higher bandwidth and faster velocity in underwater environment. According to the system design architecture, data rates of RF waves vary from as low as few tens of Hz to GHz. Electromagnetic waves working at Extremely Low Frequencies (ELF), i.e. at 30 - 300 Hz, are widely used in military applications or in demonstrating communication paths between terrestrial and underwater bodies. Systems like that are used for long distances propagation and for communication with naval submarines. The first ELF project was implemented in 1968 for communication between submarines in deep waters. In this project, the submarines were called by an alerting system and then they moved to the surface in order to communicate through high bandwidth terrestrial radio links [4]. In [18], the authors have noted that it is feasible to propagate RF frequencies in MHz range in sea water for distances up to 100 m by using dipole radiation with high transmission powers in the order of 100 W. Nevertheless, this proposal requires complex antenna designs and high transmission power.

For the design of RF systems that require the utilization of communication links between underwater and terrestrial transceivers, we can use any frequency ranging from MHz to GHz. Those communication systems are called buoyant RF communication system (Image 14a) and they are not pure underwater communication. Another configuration consisted of a direct RF communication link between two transceivers both located underwater or one submerged in the water and the other one set in the air (Image 14b). This system is called direct RF communication system and it uses ELFs or Low Frequencies (LFs) for communication.

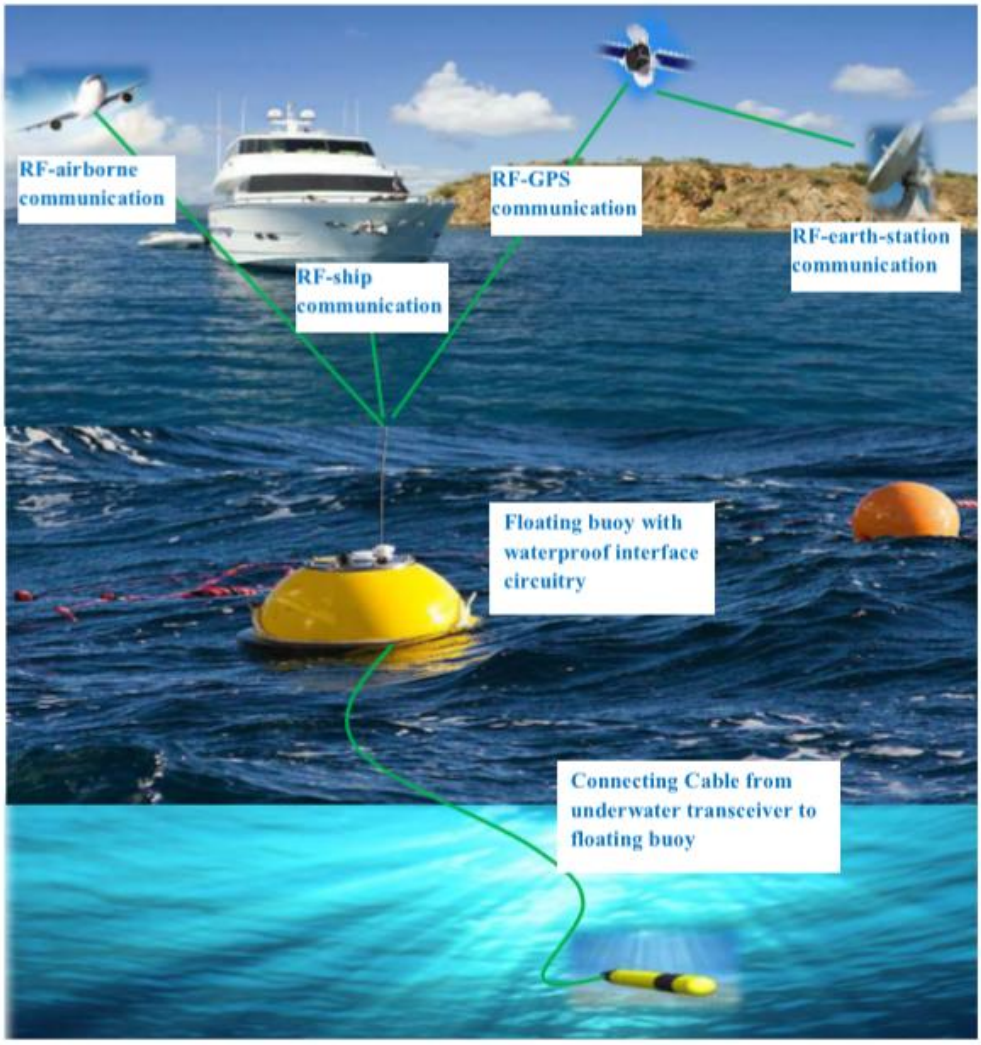

(a)

(b)

Image 14: Underwater RF system design architecture (a) Buoyant RF communication system (b) Direct RF communication System [4].

In [19], the authors made an attempt to compare RF and acoustic communications, which gives maximum propagation distances for several frequency ranges. For instance, at 100 kHz the maximum range is 6 m, at 10 kHz it is 16 m and at 1 kHz it is 22 m. Data rate in RF communication can be increased by applying Multiple Input Multiple Output (MIMO) schemes. Also, in [20] it has been declared that with the use of Quadrature Phase Shift Keying (QPSK) modulation scheme with four transmit antennas we can achieve transmission rate of 48 kbps at 23 kHz bandwidth over a distance of 2 km.

Generally, most of the works implemented for underwater communication through RF frequencies subject to high losses, resulted from the conductivity of sea water. The average conductivity in sea water is 4 mhos/m, i.e. almost two orders higher than the conductivity in fresh water. As a result, waves with high frequencies suffer from increased absorption losses in sea water, as depicted in Image 15. The absorption coefficient of sea water is related to its conductivity as:

$$a_{sea\ water} \approx \sqrt{\pi f \mu \sigma} \quad (21)$$

where α is the absorption coefficient, f the operating frequency, μ the permeability and σ the conductivity. For this reason, most of the designed work is operating in low frequencies in order to achieve long distance communication.

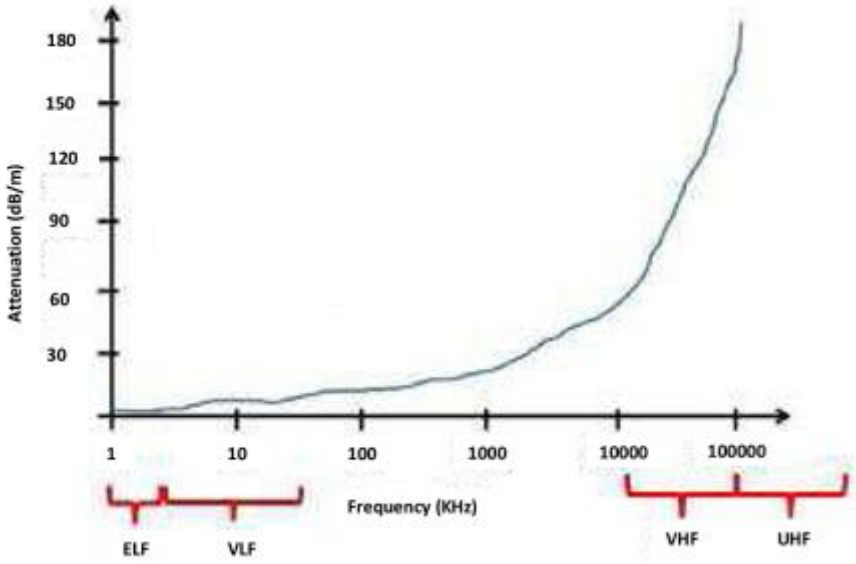

Image 15: RF attenuation in sea water [21].

On the other hand, the absorption coefficient of fresh water is basically frequency independent:

$$a_{fresh\ water} \approx \frac{\sigma}{2}\sqrt{\frac{\mu}{\varepsilon}} \quad (22)$$

where ε is the permittivity. As a consequence, RF wave communication appears to be a good choice in fresh water environment, but it necessitates not only antennas with very large size, but also high transmission power, in order to make up for high antenna losses. In a recent work in [23], the researcher is conducting an experimental configuration of a Wi-Fi network in freshwater using 700 MHz, 2.4 GHz and 5 GHz, in

order to verify its applicability to underwater communication and a rate adaptive algorithm is applied. It was derived that the system operating at 700 MHz can support longer distance communication, although it provides lower data rates. The systems operating at 2.4 GHz and 5 GHz can achieve higher data rates, but only for short ranges, as the path loss in water increases with the increase in propagation distance. Apart from the absorption loss, the transmitted signals have to deal with the refraction loss at air-water interface, as well, which is almost 60 dB at low frequencies and decreases with the increase in frequency [4].

1.2.3 Optical Underwater Communication

Since RF signals require huge antenna size as well as high transmitter power in fresh water and they suffer from high attenuation in sea water, the next obvious choice for underwater freespace communication are the optical signals, which can also support high data rates. In addition to that, recent progress in semiconductor light sources, including blue/green LEDs and diode lasers, have driven to significant research interest for underwater freespace optical communication. Besides the long range satellite-to-submarine communication links, the research activity is turned into shorter range, lower power and less costly systems that can be integrated into autonomous vehicles or sensor nodes. Because of the high frequencies of optical carriers, UOWC is able to provide data rates that exceed 1 Gbps at a distance of a few hundreds of meters. Even though the optical signals in underwater environment have to deal with a number of challenges, as they face strong attenuation due to water absorption and scattering caused by suspended particles and they are severely disturbed by the sunlight, there are still many possibilities for achieving broadband optical underwater links over average distances. In this section, we mention different experimental and theoretical studies related to optical underwater wireless communications [4].

The exploration of laser-based underwater links started during the 1970's. The experiments of Snow et al. in [23] showed the first results of a 7MHz square wave propagating over 18 attenuation lengths (-78 dB extinction) at a 30 meters range, as well as a 100 MHz signal propagating 45 meters, which corresponded to an optical path length of 4.5 up to 5.6 attenuation lengths, giving an extinction or attenuation coefficient between 0.1 m^{-1} and 0.125 m^{-1}, during the testing period. The system used argon-ion laser operating at green wavelengths, between 514 nm and 532 nm and it could achieve 50 Mbps over a distance of 9 m. In 1995, the authors in [24] carried out a Light Emitting Diode (LED) based theoretical analysis of UOWC for 10 Mbps at a range of 20 m and for 1 Mbps at a range of 30 m. This work was extended in 2005, when a theoretical analysis for varying data rates in different underwater environments was realized. This study recommended that the most appropriate operating ranges vary from less than 10 m for very turbid coastal water to over 25 m for clear coastal water [25]. In both cases the data rate is either 220 Kbps or 4.4 Mbps.

In practice, LEDs are usually adopted as a transmitting light source in deployable systems because of the ease of pointing and tracking. However, these devices have quite limited transmission bandwidth, since the maximum implemented data rate is 10 Mbps as noted by Farr et al. [26]. However, data rate can be as high as 80 Mbps for terrestrial applications by realizing analog or digital filters, in order to modify the pulse shape [27], [28]. Farr et al. have also managed to demonstrate oceanic UWOC over ranges of about 100 m using a LED transmitter [29]. Another work that was implemented by Anguita in [30] established a LED based receiver/transmitter system

which could achieve data rates up to 2 Mbps over short distances (2 meters) and it was based on the IEEE 802.15.4 standard for wireless personal area networks.

In [31], Hanson and Radic demonstrated a 1 Gbps link in a 2 meter test tank. The link ran error free up to 8 attenuation lengths without showing any signs of limitation due to inter-symbol interference or pulse spreading due to scattering. They also expanded their study using Monte Carlo simulations in order to predict the performance for longer ranges. The calculated bandwidth ranged from 1 GHz for a distance of 8 m in turbid harbor water to 5 GHz for a distance of 64 m in clear ocean water. Another interesting finding is presented in [33] where through complex analytical modeling is showed that the channel can be very broadband with over 6 GHz of bandwidth.

More recently, Mullen et al. have made detailed measurements of the scattering phase function of Maalox [34] and compared them with ocean scattering phase functions. They found that Maalox closely approximates the scattering phase function of natural waters, except for small angles, where the approximation is not so accurate. Therefore, Maalox is considered to be a convenient as well as appropriate material used for controlling the amount of scattering in laboratory experiments. In [34] and [35] Cochenour et al. relied on underwater imaging results from [37] and applied the same RF techniques to an optical communication system. This provided greater spectral efficiency, since it was possible to implement high-order modulation formats. Moreover, in [35], the authors demonstrated in a laboratory environment a LOS link which employs different modulation techniques i.e., Binary Phase Shift Keying (BPSK), QPSK, 8-PSK, 16-Quadrature Amplitude Modulation (QAM) and 32-QAM, using 70 MHz carrier and 3 W solid state Continuous Wave (CW) laser. It was observed that even in turbid water, it is possible to achieve 5 Mbps rate by using high power laser. In [38], Cochenour et al. compared experimental results with an approximate analytical scattering function with close agreement. The model was used to predict link performance for large transmission ranges and it was proved that Beer's Law exponential power loss is not valid for large attenuation lengths, as an amount of scattered light is captured by the receiver [4].

In [13], a short range underwater optical wireless communication link up to 5 m was established operating at 10 Mbps and using FM modulation. In 2010, a bidirectional communication link using high power LED arrays at 470 nm and discrete pulse interval modulation was developed in order to achieve a communication range of 50 m with high data rate [39].

Some researchers have also considered taking advantage of the scattering nature of ocean water by realizing non-line-of-sight (NLOS) communication links (as illustrated in the Image 16d bellow). With the use of the sea surface as a diffuse reflector, Pointing and Tracking (P&T) issues could potentially be avoided. However, there are many technical difficulties in such an implementation. The greatest obstacle is that light attenuation in seawater is severe and thus diffuse reflection would limit the amount of photons that reach the receiver. Another approach is the utilization of ultraviolet "solar-blind" underwater communication links, which is theoretically studied in [40]. Even though the transmission lengths are very short (up to 10 meters), it is possible to create a system operating in shallow waters with very wide field-of-view receivers, as this system can benefit from the lack of background solar noise.

Finally, another interesting topic is the use of a retro-reflecting modulator for underwater optical communication (illustrated in Image 16c in the nest section). This could possibly allow the transmitting device to operate at lower powers, since the high power optical beam is generated by the receiving system [4].

From all the above works it is concluded that it is feasible to realize a high capacity underwater wireless optical transmission over moderate ranges. In most of the work carried out so far, underwater optical communication link ranges vary from few meters to tens of meters [4].

In the following section are presented some typical UWOC configurations.

1.2.3.1 Link Configuration of UOWC

According to the link configurations between the nodes in UWSNs, we can classify UOWCs into four categories (Image 16):

a) Point-to-point Line-Of-Sight (LOS) configuration,
b) Diffused LOS configuration,
c) Retro-reflector-based LOS configuration, and
d) NLOS configuration. [2]

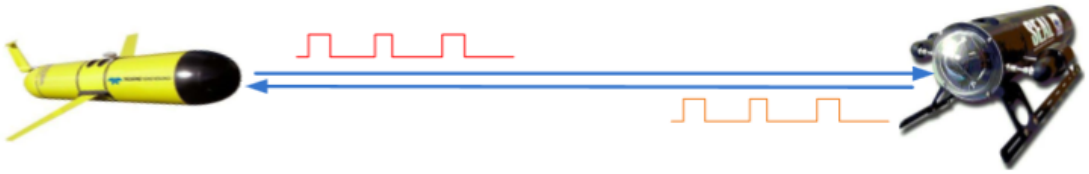

(a) Point-to-point LOS configuration

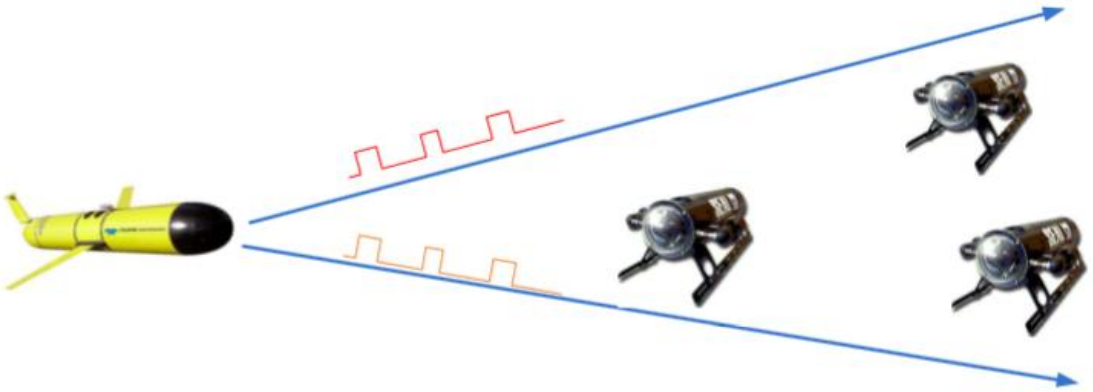

(b) Diffused LOS configuration

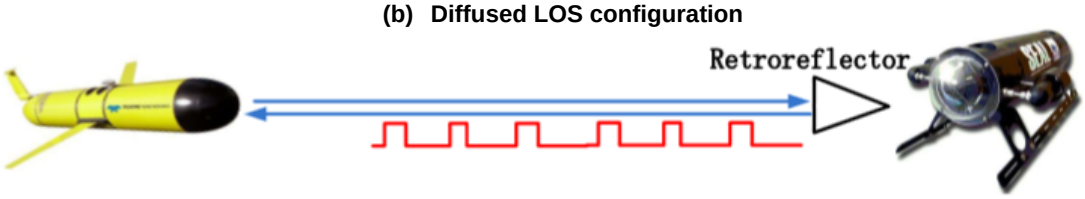

(c) Retro-reflector-based LOS configuration

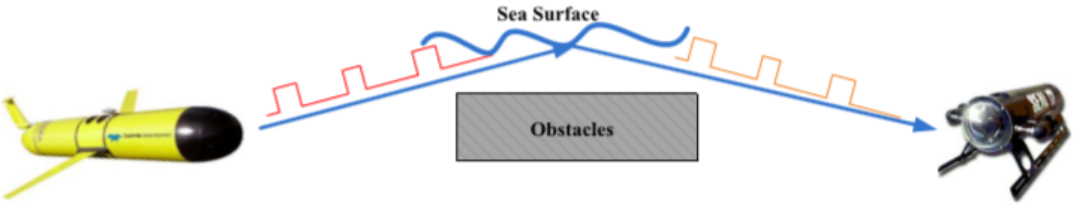

(d) NLOS configuration

Image 16: Four link configurations of UOWC [2].

1. Point-to-point LOS configuration (Image 16a): This is the most simple as well as frequently used link configuration in UOWC and it works well enough in clear oceans. Here, the two communicating nodes are aligned and the transmitter directs a narrow beam signal towards the receiver. The light sources that are commonly used in point-to-point LOS configuration are lasers, which are characterized by their narrow divergence angle. Therefore, the alignment should be precise. This requirement not only degrades the system in turbulent water environments but it can also cause serious problems when the transmitter and the receiver are non-static nodes, such as AUVs (Autonomous Underwater Vehicles) and ROVs (Remotely Operated Vehicles) [2]. For such platforms, it is vital to design a very sophisticated pointing and tracking mechanism in order to keep both transmitter and receiver in line of sight. Therefore this link configuration is more suitable for implementations where we have static transmitters and receivers, like two sensor nodes at the bottom of the ocean.
However, even in clear oceans and with perfect alignment, there are high chances of shading due to marine life growth, schools of fish or other obstacles. Thus, for demonstrating a LOS link is important to design a system which prevents the marine life from blocking the propagation path. Unfortunately, the lights that are considered best suited for underwater optical communication tend to attract schools of fish, as ocean water fishes prefer blue-green lights while fresh water fishes prefer yellow-green lights. So, in order to discourage fishes from entering the LOS region, it is better to use flashing or erratic lights [4].
The received signal power, P_R in a LOS configuration is given by [4]

$$P_{R\_LOS} = P_T \eta_T \eta_R L_p\left(\lambda, \frac{d}{\cos\theta}\right) \frac{A_R \cos\theta}{2\pi d^2 (1-\cos\theta_d)} \qquad (23)$$

where P_T is the average transmitter optical power, η_T and η_R are optical efficiencies of the transmitter and receiver, respectively, L_p is the propagation loss which is a function of the wavelength and the distance and is expressed as $L_p = exp(-c(\lambda) \times z)$ with $c(\lambda)$ the wavelength dependent extinction coefficient and z the distance, d is the perpendicular distance between the transmitter and receiver plane, θ is the angle between the perpendicular to the receiver plane and the transmitter-receiver trajectory (Image 17), A_R is the receiver aperture area and θ_d is the laser beam divergence angle. Typically, the value of θ_d is much smaller than π/20 [4].

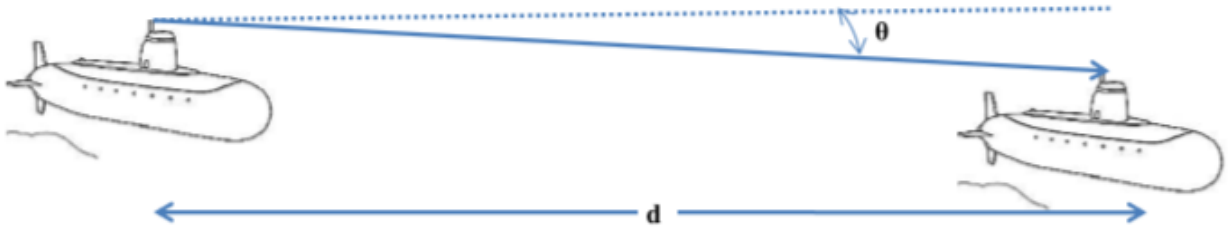

Image 17: LOS configuration scheme with more details [4].

In [41] and [42], laboratory experiments are realized for LOS links with the use of Light-Emitting Diodes (LEDs) operating in green and blue spectrum. The communication link in [42] is a 10Mbps LOS link, which, according to water type, can operate in ranges up to 40 m long. The main purpose of both experiments is

to study the characteristics of laser beam propagation through different water types, such as waters with different turbid level. From the results it is concluded that the viewing angle, propagation range and turbid level play a critical role in the behavior of the blue light.

2. Diffused LOS configuration (Image 16b): This system applies diffused light sources, such as high-power LEDs, which have large divergence angle, in order to broadcast optic signals from one node to multiple nodes. Such link types are also called diffuse links [4]. This method does not require the precise alignment that the point-to-point configuration needs. However, the diffused-light based link suffers from higher aquatic attenuation, as the light covers a larger area and, thus, it interacts more with water and its particles. The main limitations of this configuration are the relatively shorter communication distances and lower data rates.
3. Retro-reflector-based LOS configuration (Image 16c): This configuration can be considered as a special implementation of the point-to-point LOS configuration. Retro-reflector-based LOS configuration is suitable for duplex UOWC systems with underwater sensor nodes that have limited power and weight budget. In this link, the source has more power and payload capacity than the receiver, thus serves as an interrogator which sends modulated light signals towards the remote receiver. After that, the light is reflected back from the receiver, which is equipped with a small optical retro-reflector. During this process, the information that the retro-reflector responses to the transceiver will be encoded on the reflected light. Since there is no laser or other light source in the retro-reflector end, its power consumption, volume and weight will be excessively reduced.
   One drawback of this system is that the backscatter of the transmitted optical signal may interfere with the reflected signal, degrading the system's SNR and BER. Furthermore, as the optical signals go through the underwater channel twice, the received signal will experience additional attenuation. In particular, the received power in this case is given as

$$P_{R\_Retro} = P_T \eta_T \eta_R \eta_{Retro} L_P\left(\lambda, \frac{2d}{\cos\theta}\right) \frac{A_{Retro}\cos\theta}{2\pi d^2(1-\cos\theta_d)} \times \frac{A_R\cos\theta}{\pi(d\tan\theta_{Retro})^2} \quad (24)$$

where η_{Retro} is the optical efficiency of the retro-reflector, A_{Retro} is the retro-reflector aperture area, θ_{Retro} is the divergence angle of retro-reflector and the other parameters are defined in Equation (23) [4].

The retro-reflector underwater operates in two scenarios: (1) photon limited and (2) contrast limited. The photon limited scenario takes place at clear ocean waters or lakes. In this case, the link range and capacity are limited by the amount of photons falling on the detector. Because of the absorption effect, this amount is always less than the amount of transmitted photons. Furthermore, like in LOS configuration, pointing and tracking are critical in this scenario, as the information that is born by the retro-reflected signal depends on the density of interrogating photons incident on the retro-reflector. On the other hand, the contrast limited scenario occurs in turbid harbors, where link range and capacity are degraded mainly because of the scattering effect. This is a crucial problem for applications related to underwater laser imaging. In this case, the increased back-scatter signal results in reduction of received photons and thus, decreases the contrast of the image. If polarization discrimination is applied, then the back-scatter component can be significantly reduced [4]. These characteristics of underwater retro-reflector configuration are illustrated in Image 18.

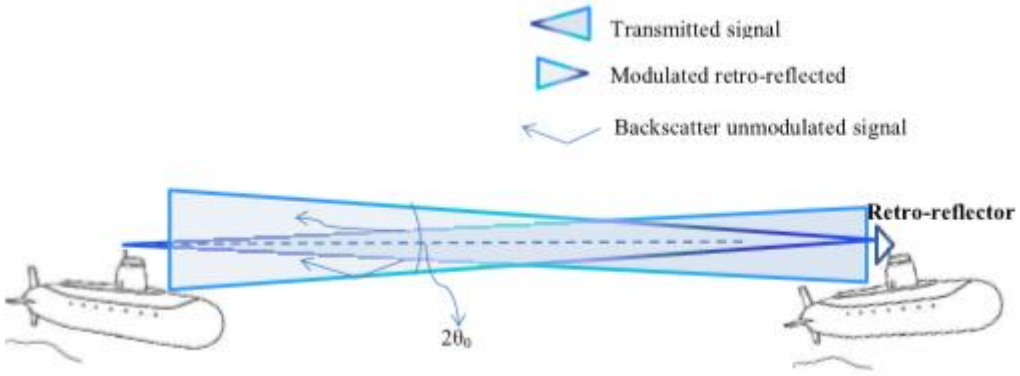

Image 18: Modulating retro-reflector configuration [4].

4. NLOS configuration (Image 16d): This overcomes the alignment restriction of LOS UOWC, which is not always feasible in practical systems. In this system, the transmitter projects the light beam to the sea surface with an angle of incidence greater than the critical angle, so that the light beam experiences a Total Internal Reflection (TIR). For this reason, these types of links are also called reflective links. On the other side, the receiver keeps facing the sea surface in a direction that is approximately parallel with the reflected light, in order to ensure proper signal reception. The major challenge of NLOS links is the random sea surface slopes induced by wind or other turbulence sources. These undesirable phenomena will reflect light back to the transmitter and cause severe signal dispersion. [2]
   For clear lake or ocean water environments, the divergence of laser beam has to be increased, by utilizing an array of LEDs or lasers, in order to form a cone of light characterized by its inner and outer angles θ_{min} and θ_{max} in the upward direction, as illustrated in Image 19. When the transmitter is at depth h, the illuminated annular surface with equal power density at depth x will be given by [4]

$$A_{ann} = 2\pi(h+x)^2(cos\theta - cos\theta_{max}) \quad (25)$$

   The received power would then be given by [4]

$$P_{R_{NLOS}}(\theta) = A_R f_R(\theta) \quad (26)$$

   where $f_R(\theta)$ is an auxiliary function dependent on P_T, A_{ann}, η_T, η_R, $(h+x)$ and transmission angle, θ_t derived from Snell's law.

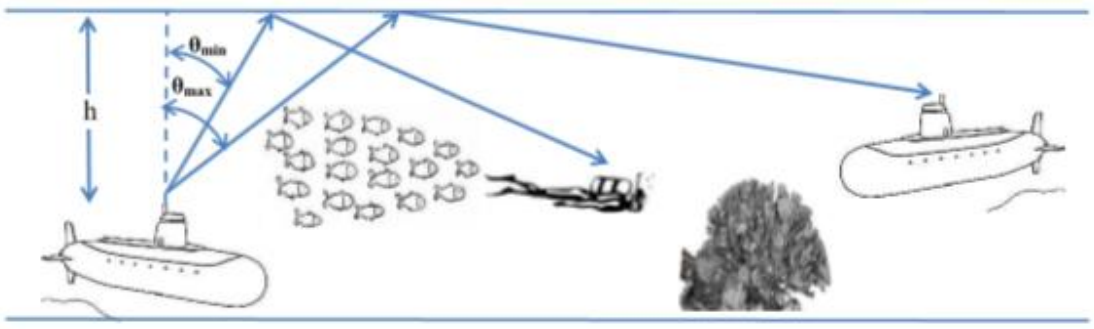

Image 19: Beam in NLOS configuration [4].

In [43] a comparison of LOS and NLOS configurations is carried out, showing that the 100 MHz bandwidth which can be available for LOS link in turbid environment decreases to almost 20 MHz in NLOS environment even in clear water. In [44], a high bandwidth UOWC system for tele-roboting operations is developed which is consisted of an array of LEDs in hemi-spherical configuration to enable larger divergence angles of the transmitter. In this experiment, wireless underwater video pictures were transmitted at 1.5 Mbps rate, up to a range around 15 m in turbid water environment. Another geometrical configuration that is used for NLOS links is the icosahedron design, which is broadly applied in UOWC systems because of its geometrical simplicity and its ability to provide complete free space coverage using LEDs. Other potential geometrical designs are those with directional transmitters and omni-directional receivers or both transmitter and receiver being omni-directional. The last case is mechanically the simplest solution, as it relaxes the pointing and tracking requirements. A scenario like this is implemented by Fair et al. [29], where omni-directional LEDs are used to provide the diffusion of light over the full operating region (Image 20) and are able to achieve omni-directional UOWC for 10 m range. This work is mainly focused in AUV and fixed node applications in seafloor observatories. Moreover, the link budget analysis for NLOS geometries is presented, taking into consideration only the attenuation caused by attenuation-extinction coefficients. Their investigation does not take into account multipath interference, spatial dispersion, time dispersion and multiple scattering. As a consequence, the results are valid only for clear ocean or lake waters [4].

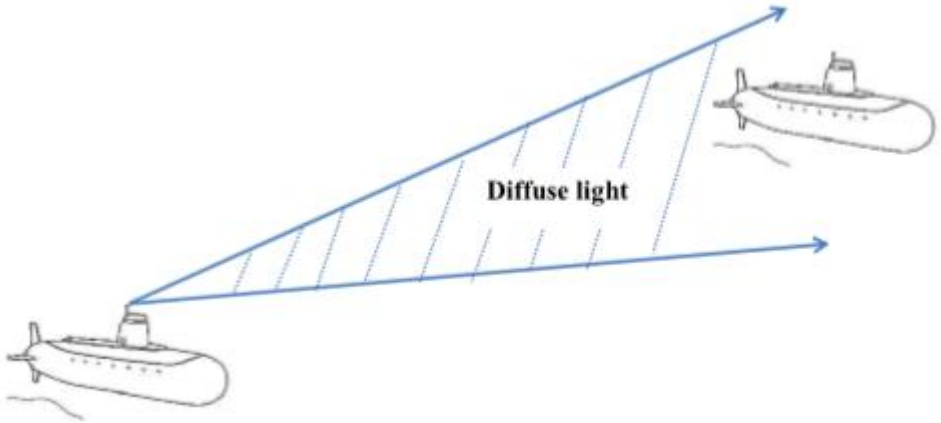

Image 20: Diffusive NLOS configuration [4].

In [45], mathematical equations are derived for computing the received power and BER in three different scenarios, namely LOS, modulating retro-reflector and reflective configurations. Using those equations, the authors analyze the link performance for each configuration. Generally, it can be deducted from the mathematical analysis that the LOS configuration has the best performance except for cases where either the LOS link is not feasible due to existing obstacles, and thus the reflective configuration is more suitable, or a more complex transceiver with more available resources can be supported and thus the retro-reflective communication is preferred.

1.2.4 Hybrid Acoustic/Optical UWC Systems

As expressed in the previous discussion, the performance of UOWC systems can be severely degraded by the absorption and scattering effects of sea water and other impact factors. These negative factors can cause frequent communication failure. Therefore, the performance of a UOWC system should be improved. Additionally, the transmission range of underwater optical wireless communication is only few meters. On the other hand, acoustic communication can support longer ranges, even though it has lower bit rate, higher power consumption and significant latency. Acoustic modems can operate between 100 and 5000 bps over moderate link distances. They can also operate at higher data rates, but for shorter distances. Taking these facts into consideration, many works, like [2], have noticed that it is necessary to create a hybrid system, that will take advantage of both technologies, and they are proposing the use of acoustic waves as back-up scenarios, in order to enhance the reliability of a UOWC system or to cover longer transmission distances. The hybrid system will complement the existing acoustic system by providing high data rate and low latency when operating within optical range and long range and robustness when operating outside the optical range. For example, the goal in underwater AUVs or sensors is to relay a high volume of data to the central base station, where the information is processed. These AUVs are frequently equipped with both acoustic and optical modems. For long distance communication the AUVs use the acoustic modems, while for short distance communication they use the optical modems, after the alignment is achieved through the acoustic communications. Consequently, in hybrid systems, optical transmitters occupy most of the uplink bandwidth as they will transmit highly-directional high bandwidth signals. In contrast, the downlink signal from the base station or ship to AUVs is a low frequency acoustic signal with wide FOV and it is used for pointing or tracking purposes [4].

Taking into consideration the advantages and disadvantages of the optical and acoustic methods, the authors in [2] have proposed two hybrid link methods, which are shown in Image 21. In the first configuration in Image 21a both acoustic and optical signals are implemented as a duplex transmission medium. In this approach, the two end points of the communication link are all mobile underwater vehicles that are equipped with both acoustic and optical transceivers. The system is sensing the channel conditions and based on them it selects what communication method to use. In particular, when the two communicating nodes are in short distance and the water is clear, the system will use an optical carrier in order to achieve high data rate. On the other hand, if the two nodes are in large distance or the water is turbid, the system will operate on the acoustic band, so that it will avoid the connection failure. This configuration benefits from its high flexibility and reliability. However, having acoustic transceivers on both ends results in high power consumption and heavy instruments and thus increases the cost of implementing a system like that. The second configuration, which is shown in Image 21b, utilizes one static control platform and several mobile sensor nodes. For the transmission of control information to the downlink, i.e. from the control platform to each sensor node, the controller uses acoustic signals as a broadcasting method. On the other side, the sensor nodes communicate with each other and with the control platform with the utilization of optical communication links. Obviously, this hybrid UWC system takes advantage of the virtues of both communication ways. One advantage is that the acoustic signals have diffusion properties and can maintain long propagation distances, and therefore they can cover the area that is distributed with sensor nodes. Furthermore, since the information transmitted from the control platform to the sensor nodes is consisted of low-speed control signals, the acoustic waves are well suited for

the downlink. As for the uplink, it is preferred to realize high speed UOWC links for transmitting a large amount of oceanic monitoring data.

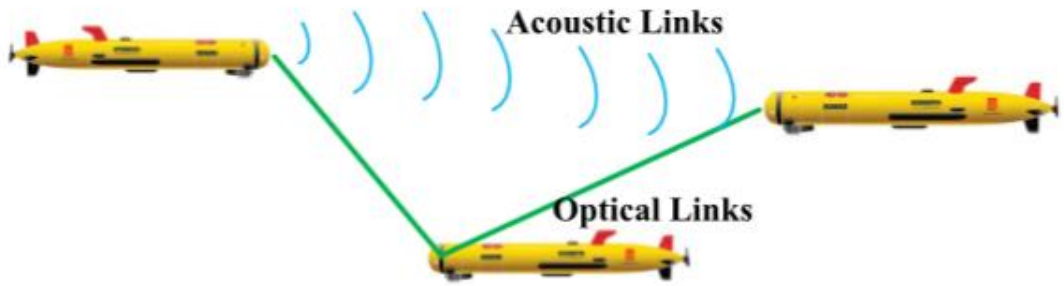

(a) Mutual hybrid UWOC configuration

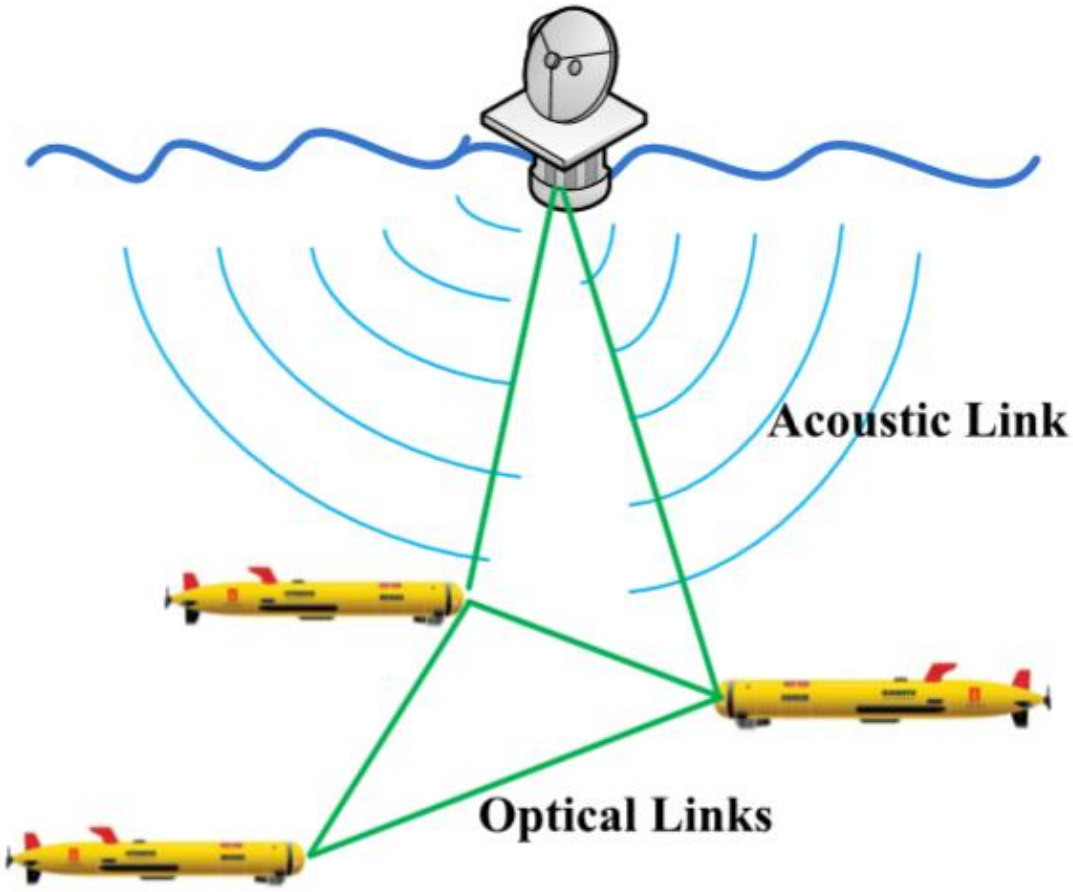

(b) Broadcasting hybrid UWOC configuration

Image 21: Two types of hybrid acoustic/optical UWC links [2].

Based on these hybrid UOWC link designs, several related research has been proposed in recent years. The researchers in [45] have presented a hybrid UWSN, which can achieve long-term underwater monitoring tasks, such as video streaming of the sea floor, as well as real time data transmission of water parameters, like temperature and pressure. This hybrid UWSN includes two types of sensor nodes: static nodes and mobile nodes. High-speed optical waves are used for point to-point communication between two nodes, whereas the acoustic mode is utilized for diffused broadcasting links. In addition, the mobile nodes can detect and approach the static nodes for data muling. The authors also demonstrated several optimizing algorithms

and the corresponding hardware implementations of the system. The experimental results showed that this hybrid data collection system can achieve a much higher power and data transmission efficiency than the typical acoustic underwater networks with multihop protocols.

Another related work is the one presented in [47], where the operation concept of an Untethered Remotely Operated Underwater Vehicle (UTROV) that utilizes both optical and acoustic communication methods is described. This vehicle can achieve conventional survey and reconnaissance tasks over a long distance using a low bandwidth acoustic modem. It can also establish an optical communication link with a small ship-based or seafloor-based relay. The main advantage of this deployment is that it does not require a physical connection to the ROV. Otherwise, the system would need to send ROVs thousands of meters deep in the sea water for fetching data, for example from oil resources, which is costly and time consuming. This model is also convenient for real time video streaming, which requires high bandwidth and low latency. Based on UTROV, the authors also implemented a seafloor borehole observatory system, which is called Circulation Obviation Retrofit Kit Optical Telemetry System (CORK-OTS) in [48]. The CORK-OTS includes several underwater ROVs and a surface boat with lowered cable. An acoustic modem was integrated at the lowered cable end in order to send control information, whereas optical transceivers were realized in both ROV and lowered cable end for reaching high data rates [2].

Hybrid duplex acoustic/optic system has also been investigated in [49], where highly directional optical signals are used for the uplink transmission of high data rates from submerged AUVs or divers to the base station, while acoustic signals are used for the wide angle, low data rate downlink. In this work, it was stated that the maximum data rate of a hybrid model is greater than the data rate of a traditional acoustic link by a factor of 150. A Multi-level Q-learning-based Routing Protocol (MURAO) is presented in [50], which uses hybrid acoustic/optical communication for underwater wireless sensor networks. From the experimental results, it was concluded that MURAO is more robust to changes of network topology and it reaches much higher transmission rates as well as shorter delays in a dynamic network, compared to the flat Q-learning routing [4].

Besides the experimental setups of hybrid UOWC, a few theoretical studies have been also reported. Some of the factors, mentioned in [49], which limit the system performance, are the refractive index variation, the optical pointing error and the acoustic latency. In [51], a theoretical evaluation of hybrid underwater optical-acoustic network is realized. This work also proposes the use of communication nodes equipped with both acoustic and optical transceivers. The authors have designed a transmission algorithm which can be applied to each node to ensure the link alignment and connectivity. Simulation results showed that the hybrid system has better energy efficiency than the pure acoustic system and is more flexible if applied in different water conditions.

As verified in Image 22, the hybrid acoustic optic system has considerable advantages in terms of throughput and energy efficiency. In Image 22a, it is obvious that the throughput of the acoustic channel saturates as the offered load increases. In contrast, in pure optical and in hybrid channel models, the throughput increases drastically. Concerning throughput, the system with the best performance is the hybrid model. Image 22b depicts the increase in power consumption as regards the increase in data rate. In this case, it is clear that the power consumption raises rapidly for acoustic models, whereas for both hybrid and optical models, where the results are close to each other, the required power consumption for achieving the same data rate is much less than in acoustic models. Even though the pure optical model is the most power efficient,

the difference between optical only and hybrid models is very small. Moreover, the hybrid model can compensate for this difference with the increased throughput performance it provides. Finally, the hybrid acoustic optic system provides some degree of freedom to choose the best suited transmission method within least transmission time, according to the load and water type.

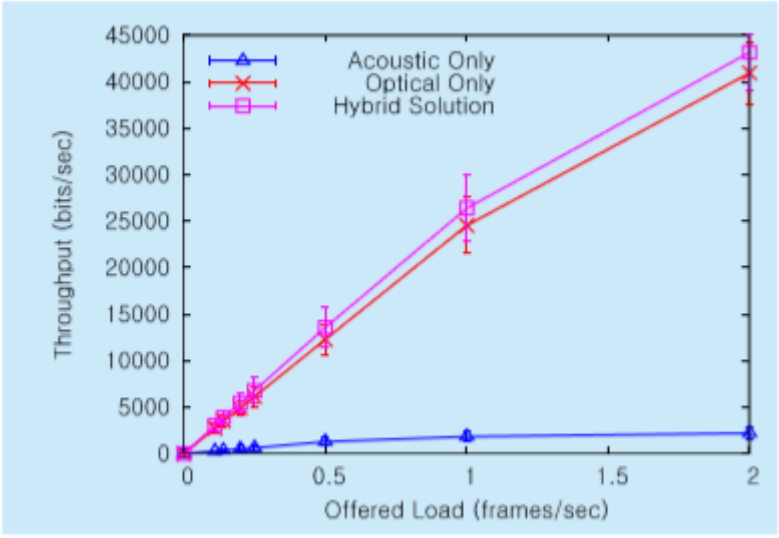

(a)

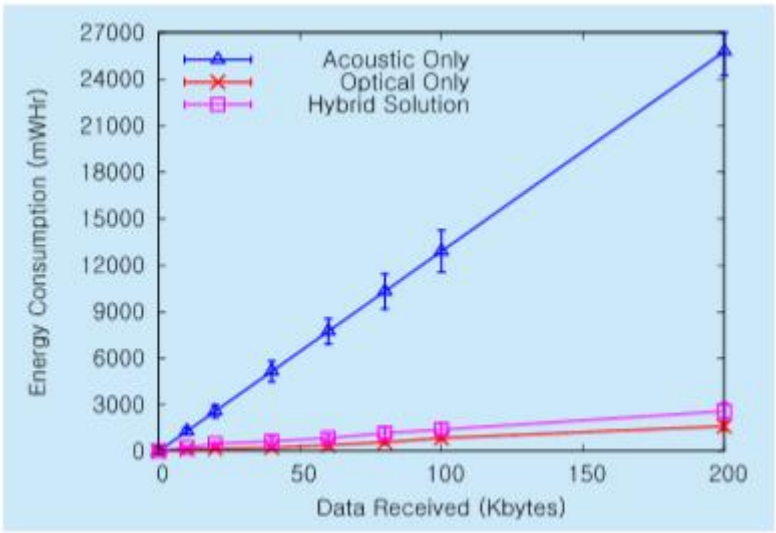

(b)

Image 22: Comparison of (a) throughput and (b) energy efficiency for acoustic, optical and hybrid systems [51].

1.2.5 Hybrid RF and Optical UWC Systems

Comparing RF signals with the optical ones, it is noted that RF signals can be transmitted only in very short distances. However, they have some advantages, as they can easily cross water-to-air or water-to-earth boundaries by following the path of least resistance, and they are more tolerant in dirty water environments [2]. Considering the benefits of RF and optical methods, a hybrid RF/optical UWC system is designed in Image 23. In this demonstration, the underwater vehicles are equipped with both RF and optical transceivers. Similarly to the configuration in **Image 21**, when the vehicles are

in deep clear water, the nodes use optical wave as transmission carrier, in order to optimize the link distance and the speed of data transmission. On the other hand, when the vehicles are moving to dirty and turbulent shallow water, they will use the RF transceivers, realizing short-range UWC with other underwater vehicles, or cross-boundary links with other communication nodes such as airplanes, satellites and ships.

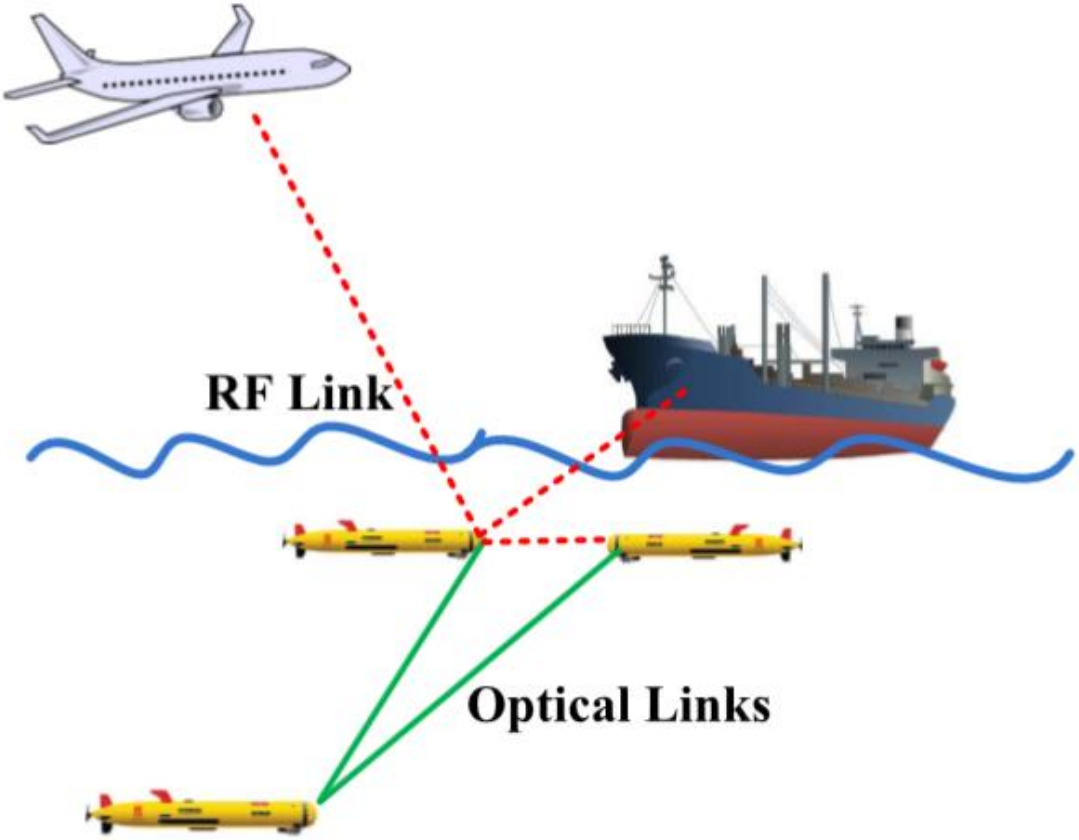

Image 23: Configuration of a hybrid RF/optical UWC system [2].

A more advanced hybrid underwater sensor network is proposed by Vasilescu et al. in [52]. The proposed network includes several sensor nodes, which are referred as *AquaNodes*. Each node is equipped with an RF bluetooth module, an acoustic module and an optical module that operates in the green spectrum. The decision of what module will be used in a specific link depends on the application environment. For example, the optical waves will be used in clear shallow water, while the Bluetooth method will be preferred in the water/air interface. Moreover, the authors have demonstrated Time-division Multiple Access (TDMA) and self-synchronization technologies for each node. The implemented experimental results have proved that this system can provide a 400-meter long acoustic link with 300 bps data rate in ocean environment and it can demonstrate an optical link up to eight meters with 330 Kbps data rate. Based on this rate, the data, such as those related to water temperature, pressure and water chemistry information, can be collected through the installed sensors and can be continuously transmitted to the communication buoy. After that, the buoy can relay the gathered information to the onshore data center for further processing and analysis.

Overall, the hybrid RF/acoustic/optical UWCs exploits the advantages of each communication method in order to increase the reliability of the system. The main challenge of hybrid RF/acoustic/optical UWC system is to adaptively and smoothly switch from one communication method to another. To carry out this function, it is of

great importance to design sophisticated environment detection protocols and algorithms that can be applied in a hybrid UWC system [2].

2. MONTE CARLO TECHNIQUE

In this work, we are modeling the underwater optical communication channel based on the Monte Carlo simulation method. This method is used in order to simulate the trajectories of a large number of emitted photons. We take into account different system parameters such as the transmitter beam width and beam divergence angle, water type, link distance, and the receiver's FOV. The Henyey–Greenstein (HG) phase function was used for modeling each photon scattering procedure. More specifically, HG phase function was used in order to describe the transition to a new direction of each photon due to a scattering event. The received intensity and the respective impulse response of the optical channel under different conditions were evaluated in this work.

In order to describe absorption and scattering process analytically, we use the Radiative Transfer Equation (RTE). To solve the RTE, we can apply both analytical methods and Monte Carlo simulations. In Monte Carlo simulations, a number of photons are stimulated into water and the interaction of photons with particulates in water is simulated. Comparing to analytical models, Monte Carlo method is simple and flexible. Thus, we apply the Monte Carlo simulation in order to measure the channel impulse response and the received intensity. The Monte Carlo method, as well as the required parameters, is described in this section.

2.1 Channel Parameters

Knowledge about the characteristics of underwater channel is necessary to model underwater communication techniques. Light beam propagating in water includes photons which undergo absorption and scattering while propagating. Light propagation in water is wavelength dependent with comparatively less attenuation in the blue/green wavelength range. In literature, absorption and scattering of the medium are characterized using two coefficients, $a(\lambda)$ and $b(\lambda)$, respectively, where λ is the wavelength. These coefficients were expressed in m^{-1} units. So, the total attenuation of the light in water can be represented by the attenuation coefficient $c(\lambda)$ (Equation 7). In our simulations the parameter λ is always the same and equal to 532 nm. Therefore, from now and on we will refer to $a(\lambda)$, $b(\lambda)$, $c(\lambda)$ as a, b, c respectively.

Another important channel parameter is the angular distribution of scattering in water, which is described by the volume scattering function $\beta(\theta)$, where θ is the scattering angle. The energy distribution of scattering light is represented by $\beta(\theta)$.

In most Monte Carlo simulations, the Henyey-Greenstein phase function is widely used to model the scattering phase function. This function is given by

$$\beta(\theta) = \frac{1-g^2}{4\pi(1+g^2-2g\cos\theta)^{3/2}} \quad (27)$$

where g is termed as the HG asymmetry parameter. The best estimate of g is $g = 0.924$ [1]. The probability density function of the scattering phase function is given by [1]

$$p_{HG}(\cos\theta, g) = \frac{1-g^2}{2(1+g^2-2g\cos\theta)^{3/2}} \quad (28)$$

2.2 Description of Monte Carlo Simulation

In this section we are analytically describing the Monte Carlo method, as applied to our simulation. Starting with the transmitter and the receiver, they are located at a distance *d* apart. More specifically, we have placed the transmitter at the location (0, 0, 0) and the receiver at (*d*, 0, 0). Furthermore, θ_{Tr} and θ_{Re} denote the elevation angles of the transmitter and receiver, respectively, and we define as φ_{Tr} the transmitter's divergence angle and as φ_{Re} the receiver's FOV.

The simulation process starts with generating numerous photons. Once a photon is launched, it is moved by a distance Δd to a new position, where it either interacts with a particle and thus the photon will be scattered and absorbed (by updating its weight), or it will reach the water surface or bottom and it will be lost or internally reflected. After every interaction with a particle in the water, the photon is scattered and is positioned in new direction coordinates (φ, θ) with reference to its current direction. The photon is repeatedly moved until it either reaches the receiver or is lost because of losing some energy after every interaction. If the photon is received, its weight and the time that it was received are recorded. If the photon is absorbed, then it is considered as a lost photon. This process is repeated for a predefined number of photons that have been inserted into the medium. By a statistical point of view, the recorded values would approach the actual values with better precision as the number of propagated photons approaches the infinity [53].

The flow diagram for the Monte Carlo simulation is presented in Image 24. Each step of the simulation is analyzed in the next sub-sections.

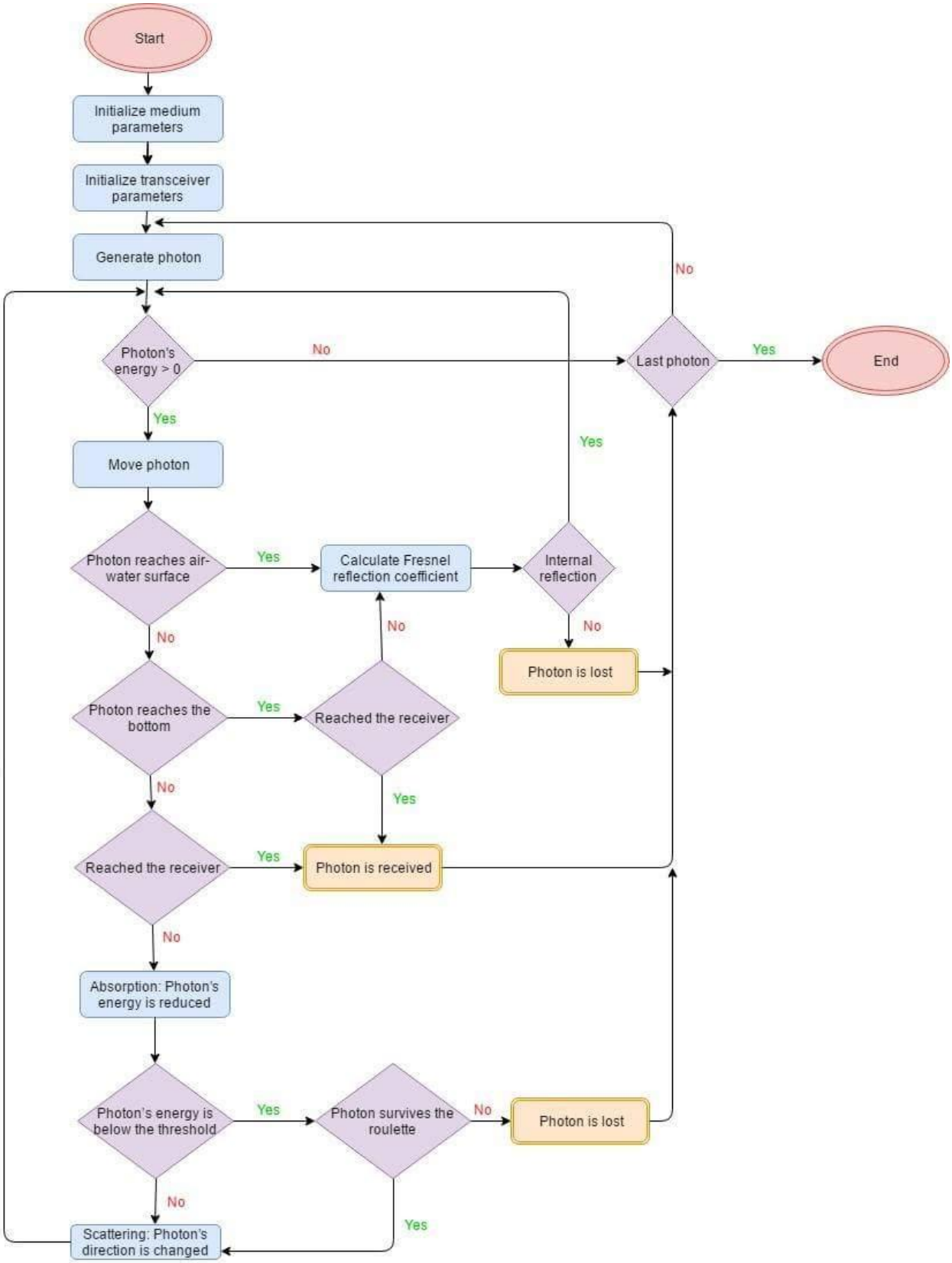

Image 24: Flow diagram for Monte Carlo simulation.

2.2.1 Photon Initialization

Initially, when each photon is launched into the medium, it is positioned at the same coordinates where the transmitter is located. At the beginning, the coordinates of the photons are identical for all of them. Initial weight and starting time of the photon is unity and zero, respectively.

In addition to the location and the weight, we also set an initial direction for the photon. To calculate the initial direction of a photon, we first need to set its azimuth (φ_{ini}) and zenith (θ_{ini}) angles, in such a way that the photon will be within the transmitter's beam. The azimuth angle takes a random value between [0, 2π]. Therefore, it is calculated from the following equation,

$$\varphi_{ini} = 2\pi\xi \qquad (29)$$

where ξ is a uniformly distributed random variable within [0,1]. The initial zenith angle for each photon is computed from the equations

$$u = \cos^{-1}\left[1 - \xi\left(1 - \cos\frac{\varphi_{Tr}}{2}\right)\right] \qquad (30)$$

$$\theta_{ini} = \mathrm{u} + \frac{\pi}{2} - \theta_{Tr} \qquad (31)$$

The direction cosines are specified by taking the cosine of the angles between the photon's direction and each axis. These are specified by μ_x, μ_y and μ_z corresponding to each of the *x*, *y*, and *z*-axes respectively and are derived from,

$$\mu_x = cos\varphi_{ini} sin\theta_{ini}$$

$$\mu_y = sin\varphi_{ini} sin\theta_{ini} \qquad (32)$$

$$\mu_z = cos\theta_{ini}$$

2.2.2 Generating the propagation distance

The Monte Carlo method propagates each photon with small step-sizes. The method chooses a different step-size (Δd) for each photon step. The probability density function for the step-size follows Beer's law. This means that it is more likely for a photon to travel a short distance than a long distance and the probability is proportional to $e^{-c\Delta d}$.

A function of a random variable ξ uniformly distributed between zero and one which yields a random variable with the distribution of the step size is:

$$\Delta d = -\frac{\log(\xi)}{c} \qquad (33)$$

The step-size Δd, which is found by using Equation (33), represents the random distance that a photon will travel before the interaction with a scattering particle [53].

2.2.3 Moving the photon

Photon's path and location within the channel is given by the direction cosines (μ_x, μ_y, μ_z) and the position vector (x, y, z). Generally, it is convenient to describe the photon's spatial position with three Cartesian coordinates and the direction of travel with three direction cosines. The required formulas of propagation are simple, and the angle variables describing photon direction do not change unless the photon's direction changes. For a photon located at (x, y, z), travelling a distance Δd in the direction (μ_x, μ_y, μ_z), the new coordinates (x', y', z') can be retrieved by the following equations

$$x' = x + \mu_x * \Delta d$$

$$y' = y + \mu_y * \Delta d \quad (34)$$

$$z' = z + \mu_z * \Delta d$$

2.2.4 Internal Reflection

The internal reflection occurs when the photon is propagated across a boundary into a region with a different refractive index. Such boundaries are the water – air surface and the bottom of the sea. For example, when a photon, during a step size, exits the water medium and reaches the air, we must move it back to the sea surface and simulate the photon's behavior for this case, as described in Image 25.

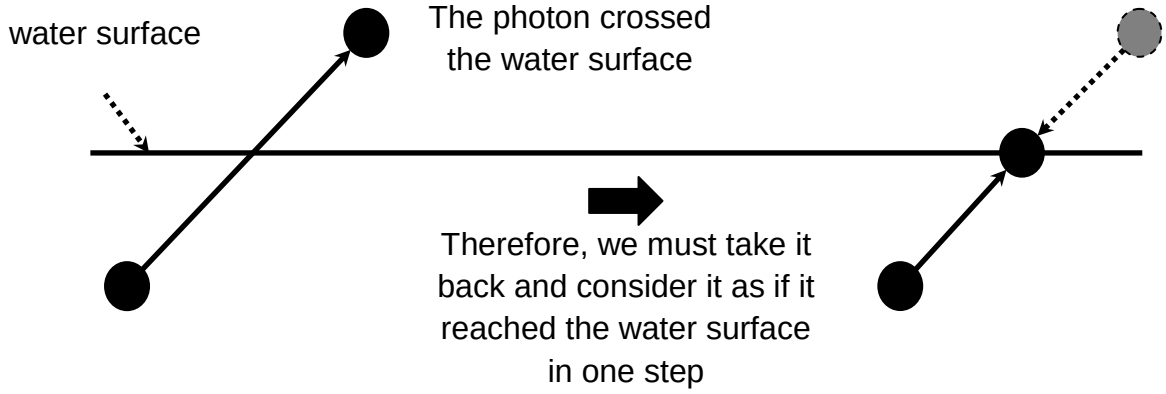

Image 25: Photon's behavior when it gets out of the sea surface in a step size.

In this case, if $z_{photon} > z_{max}$, where z_{max} denotes the height of the surface when calculated from the sea bottom, then the following process should be initiated. A random number ξ, uniformly distributed between zero and one, is used to decide whether the photon is reflected or transmitted. The probability that the photon will be internally reflected is determined by the Fresnel reflection coefficient $R(\theta_i)$:

$$R(\theta_i) = \frac{1}{2}\left[\frac{sin^2(\theta_i - \theta_t)}{sin^2(\theta_i + \theta_t)} + \frac{tan^2(\theta_i - \theta_t)}{tan^2(\theta_i + \theta_t)}\right] \quad (35)$$

where θ_i is the angle of incidence on the boundary and θ_t is the angle of transmission and is given by the Snell's law

$$n_i \sin\theta_i = n_t \sin\theta_t \quad (36)$$

where n_i and n_t are the indices of refraction of the medium from which the photon is incident and transmitted, respectively. In our simulations, θ_i coincides with the photon's zenith angle and n_i is the refractive index in the water (n_{water}). The index n_t is either the refractive index of the air (n_{air}) or the refractive index of the sea bottom (n_{bottom}) (Image 25). If $\xi < R(\theta_i)$ then the photon is internally reflected. Otherwise the photon exits the water area and it is lost. If the photon is internally reflected, then the position and direction of the photon are adjusted accordingly. If the photon is internally reflected, then it should be placed in the water-air boundary, so that it will be in the medium, and then its coordinates (x', y', z') should be updated. More specifically, for the water – air surface, the new position of the photon will be

$$x' = x + \mu_x * \Delta d'$$

$$y' = y + \mu_y * \Delta d' \quad (37)$$

$$z' = z_{max}$$

where x, y, z are the coordinates of the photon and μ_x, μ_y, μ_z the respective directions in the last step. Finally, $\Delta d'$ is the new step size, from the previous position before incident on water-air or water-bottom surface, calculated from the distance between the photon's last location and the sea surface:

$$\Delta d' = \frac{z_{max} - z}{\mu_z} \quad (38)$$

Despite the new photon's position, its direction is also changed after the reflection (Image 26).

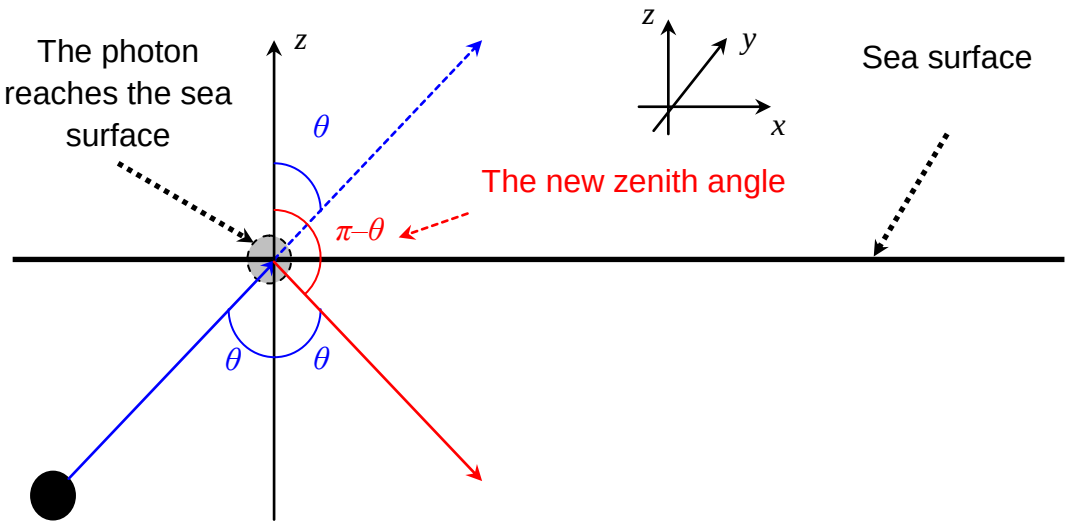

(a) Zenith angle, θ

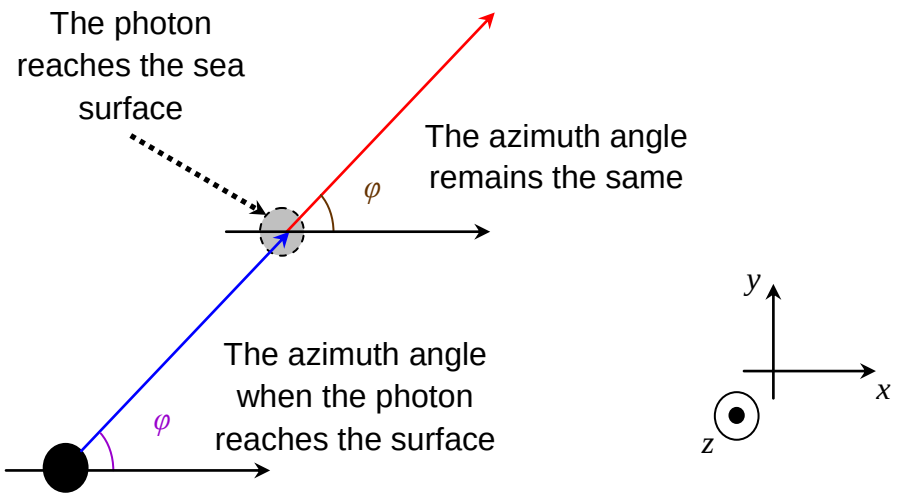

(b) Azimouth angle, *φ*

Image 26: Photon's direction after the internal reflection.

From Image 26 it is derived that the new zenith angle is the supplementary angle of the old zenith angle *θ*, while the azimuth angle *φ* remains the same. Therefore, the photon's direction (μ_x, μ_y, μ_z) will change to (μ'_x, μ'_y, μ'_z), where:

$$\mu_x{}' = \cos(\varphi) \times \sin(\pi - \theta) = \cos(\varphi) \times \sin(\theta) = \mu_x$$

$$\mu_y{}' = \sin(\varphi) \times \sin(\pi - \theta) = sin(\varphi) \times \sin(\theta) = \mu_y$$

$$\mu_z{}' = \cos(\pi - \theta) = -\cos(\theta) = -\mu_z$$

Subsequently, the new photon direction after internal reflection is

$$(\mu'_x, \mu'_y, \mu'_z) = (\mu_x, \mu_y, -\mu_z) \qquad (39)$$

As we can see from Equation (39), only μ_z changes, while both μ_x and μ_y remain the same.

Similarly, for the case where the photon reaches the sea bottom, the new position of the photon will be

$$x' = x + \mu_x * \Delta d'$$

$$y' = y + \mu_y * \Delta d' \qquad (40)$$

$$z' = z_{min}$$

where z_{min} is the z coordinate of the bottom. We have defined that $z_{min} = 0$. In this case, $\Delta d'$ is calculated from the distance between the photon's last location and the sea bottom:

$$\Delta d' = \frac{z_{min} - z}{\mu_z} \qquad (41)$$

Moreover, the photon's directions will be again modified to

$$(\mu'_x, \mu'_y, \mu'_z) = (\mu_x, \mu_y, -\mu_z)$$

2.2.5 Photon absorption

After each propagation step, the photon packet is split into two parts – a fraction is absorbed and the rest is scattered. Therefore, its weight and direction are changed. The fraction of the packet that is absorbed is [52]

$$fraction_{absorbed} = \frac{a}{a+b} = 1 - \frac{b}{a+b} = 1 - \frac{b}{c} \quad (42)$$

where $\frac{b}{c}$ is the single particle albedo. Consequently, the new photon weight (W_{new}) is given by $W_{new} = \frac{b}{c} W_{old}$, which represents the fraction of the packet that is scattered on this step. Alternatively, the reduced weight can be calculated according to the following function:

$$W_{new} = \left(1 - \frac{a}{c}\right) W_{old} \quad (43)$$

2.2.6 Photon termination

While propagating a photon, it is highly possible that it will lose much of its energy before it reaches the receiver. This energy is continuously reducing without necessarily reaching the zero value. However, to keep on propagating a photon with a minuscule weight yields very little information. On the other hand, absorbing or discarding all the remaining weight, after the weight falls below a minimum (e.g., 0.001), skews the absorption profile or violates the energy conservation respectively. A technique called roulette is used in the literature [53], in order to terminate a photon once its weight drops below a minimum threshold. The roulette technique gives such a photon (with weight W_{old}) one chance in m (e.g., 1/10) of surviving. If the photon survives the roulette, it will continue its propagation, but its new weight will be $W_{new} = mW_{old}$. Otherwise, if the photon does not survive the roulette, its weight will be reduced to zero. In that case, the photon will be discarded in an unbiased fashion, without sacrificing energy conservation and without continuing propagation until its weight reaches zero.

2.2.7 Photon scattering

A normalized phase function describes the probability density function for the azimuthal and longitudinal angles for a photon when it is scattered. If the phase function has no azimuthal dependence, then the azimuthal angle φ is uniformly distributed between 0 and 2π, and may be generated by multiplying a pseudo-random number ξ uniformly distributed over the interval [0, 1] by 2π:

$$\varphi = 2\pi\xi \quad (44)$$

This ξ is different from the random variable ξ that is used to compute Δd in Section 2.2.2.

The direction of photon trajectory is also changed with the scattering zenith angle θ, due to the scattering effect. The zenith angle θ for an isotropic distribution is given by

$$cos\theta = 2\xi - 1 \quad (45)$$

where ξ is a newly generated random variable, uniformly distributed between [0, 1].

Since scattering in water is characterized by the Henyey-Greenstein phase function, the generating function is

$$cos\theta = \frac{1}{2g}\left[1 + g^2 - \left(\frac{1-g^2}{1-g+2g\xi}\right)^2\right] \quad (46)$$

If we have isotropic scattering (i.e. $g = 0$) then we should use Equation (45).

If a photon is scattered at an angle (θ, φ) from the direction (μ_x, μ_y, μ_z) in which it is travelling, then the new direction (μ'_x, μ'_y, μ'_z) is specified by:

$$\mu_x{}' = \frac{sin\theta}{\sqrt{1-\mu_z^2}}\left(\mu_x\mu_z cos\varphi - \mu_y sin\varphi\right) + \mu_x cos\theta$$

$$\mu_y{}' = \frac{sin\theta}{\sqrt{1-\mu_z^2}}\left(\mu_y\mu_z cos\varphi + \mu_x sin\varphi\right) + \mu_y cos\theta \quad (47)$$

$$\mu_z{}' = -sin\theta\sqrt{1-\mu_z^2}cos\varphi + \mu_z cos\theta$$

If the angle is too close to the normal (for instance $|\mu_z| > 0.99999$), then the Equations in (47) can be simplified to the following forms,

$$\mu_x{}' = sin\theta cos\varphi$$

$$\mu_y{}' = sin\theta sin\varphi \quad (48)$$

$$\mu_z{}' = \frac{\mu_z}{|\mu_z|}cos\theta$$

2.3 Previous works related to underwater channel simulations

In the recent years many theoretical works have been published, which try to simulate the optical characteristics of the underwater environment. As we have seen, Monte Carlo simulation is the most frequently used method. Therefore, in this chapter we will refer to some previous works that have theoretically studied or experimentally verified the Monte Carlo method.

Starting with [53], the channel impulse response is numerically evaluated for turbid water environments, like coasts and harbors. The authors demonstrated two methods

for simulating the impulse response. In the first method they used the Henyey-Greenstein phase function and the channel was modeled based on the Monte Carlo technique, whereas in the second method the impulse response was simulated through the double Gamma function. As shown in Image 27, the impulse response derived from the Monte Carlo simulation is very close to the Gamma distribution for the tested environments. Therefore, in turbid waters we can characterize the impulse response by the use of double Gamma function for computational simplicity.

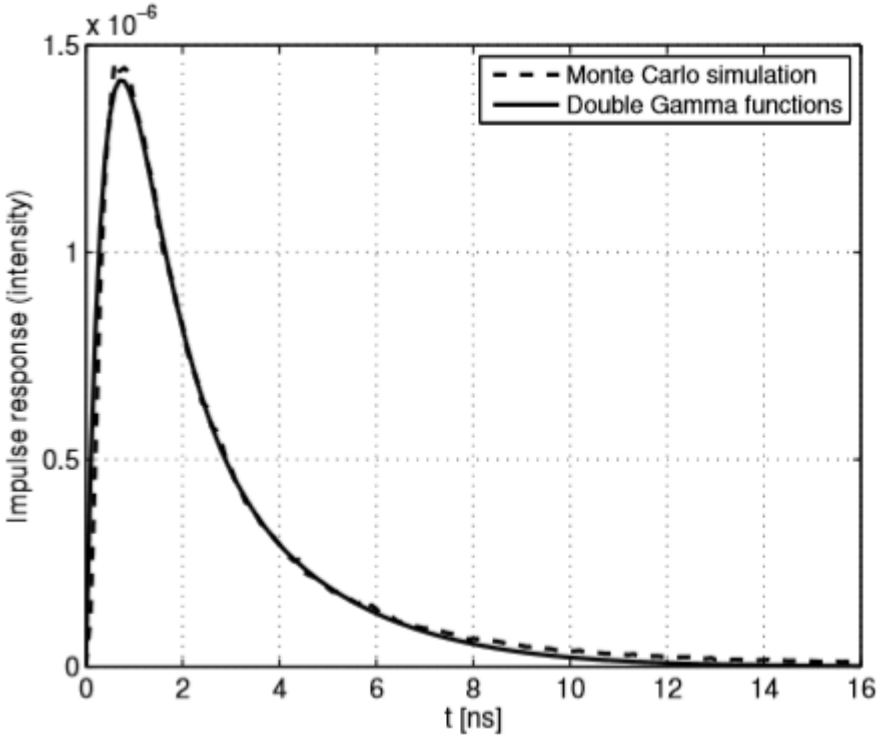

(a) L = 10 m link

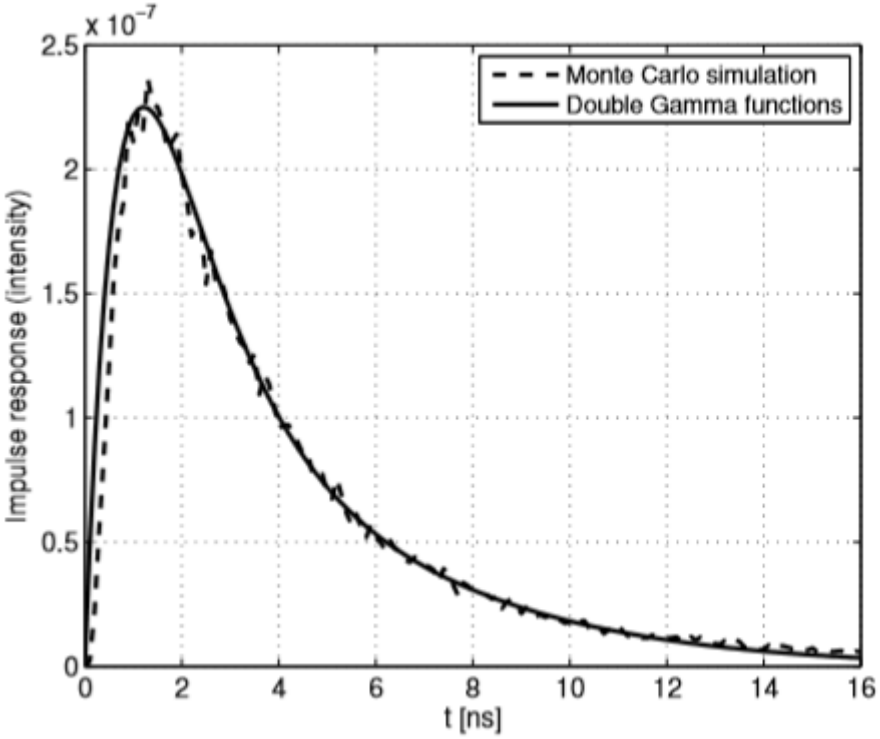

(b) L = 12 m link

Image 27: Impulse response in harbor water [53].

In [54], the impulse response was calculated for NLOS UWOC configurations using the Henyey-Greenstein phase function and Monte Carlo modeling. The simulation was applied on clear water and coastal environments and for FOVs of 30^o and 60^o. Image 28 shows the simulated results. These diagrams depict the optical received intensity versus the distance between transmitter and receiver. In Image 28a, we notice that for larger FOV the received power is higher, whereas from Image 28b, it is obvious that in short distances the received power is higher for coastal environments, but as the distance is increased the received power is decreased more sharply compared to clear waters. Thus, in clear waters we can achieve longer transmission ranges, with reduced power at the receiver side, though, after increasing significantly the distance.

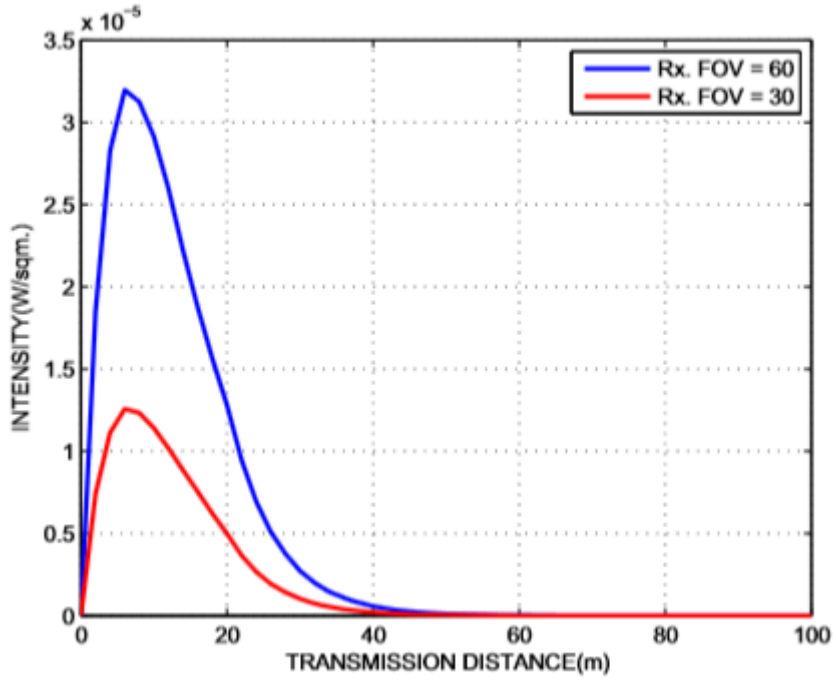

(a)

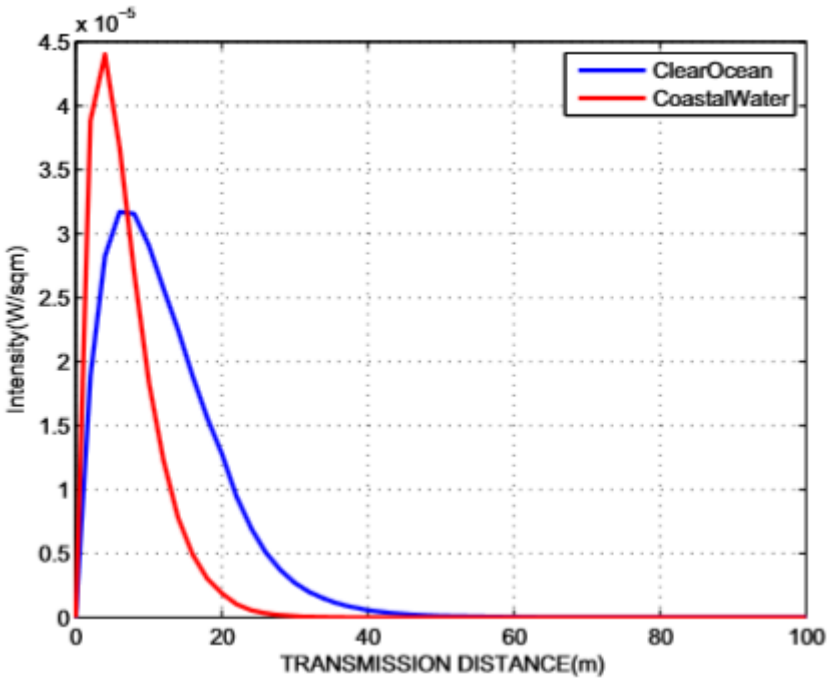

(b)

Image 28: Intensity vs. Transmission distance for (a) pure water and (b) various water types [54].

In [1], the impulse response is again calculated, but in this case the Two-Term Henyey-Greenstein (TTHG) phase function is used, instead of the simple Henyey-Greenstein function that is used in other related works, and the channel is modeled through Monte Carlo method. The advantage of the TTHG phase function is that it is considered to be more accurate for zenith angles of $\theta < 20^o$ and $\theta > 130^o$, as shown in Image 29, where b is the scattering coefficient, b_b the back-scattering coefficient and $B = b_b/b$. The authors compared the phase functions for $B = 0.038$ corresponding to a close average cosine value, $\overline{cos\theta} = 0.907$. They noticed that while the TTHG model predicts Petzold's phase function points better, especially at small angles where the phase function has its largest values, the HG model predicts a broader shape for the phase function.

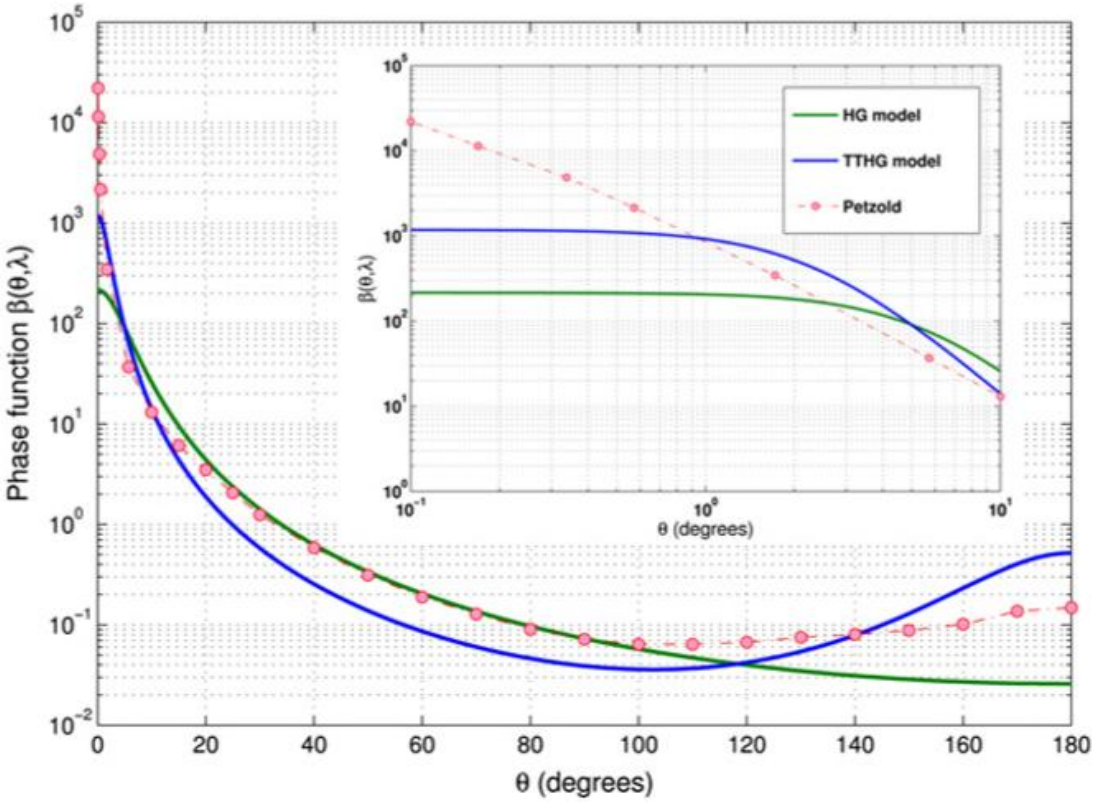

Image 29: Contrasting HG and TTHG phase functions for $B = b_b/b = 0.038$. To see better the difference of the phase functions for small angles, the Image is enlarged and displayed in log-scale for $\theta < 10^o$, where b is the scattering coefficient, b_b the back-scattering coefficient and θ zenith angle [1].

In our work, we are also simulating the NLOS optical underwater simulation environment through the Monte Carlo technique. We supplement the existing research on non-line-of-sight communication links by examining various NLOS configurations in four different water environments, namely pure sea, clear ocean, coastal water and turbid water. In our simulation we are modifying many aspects of the communication link, such as transmitter and receiver distance, aperture angle and elevation angle of the transmitter and the water's depth. Moreover, contrary to the majority of studies that consider that the receiver's Field of View is 180^o (for instance, [1] and [1]), we have applied a number of different FOV angles for the receiver, in order to see and compare the performance of each configuration. As for the impulse response of underwater environment, most works are focused in the line of sight configuration, while we on the other hand mainly focus on impulse response of the NLOS UWOC links. Finally, the main benefit of our simulation is that someone can easily change the channel as well as the NLOS communication link parameters and retrieve the computed optical received intensity and impulse response diagram for each scenario.

3. SIMULATION DESIGN

In the current thesis we are simulating a wireless optical communication link in an underwater environment. As mentioned previously, we are taking into account four different water types, which are pure sea, clear ocean, coastal water and turbid water, based on their turbidity level. Also, for each water environment we consider two scenarios regarding the water's depth. In the first scenario we have a sea with deep waters, specifically the depth is set to be 200 m, while in the second scenario we have less deeper waters with 10 m depth. In the last one, we examine the communication link's performance for the case where the optical beam is more likely to get reflected in the sea surface and, thus, more light remains within the sea with raising the probability of reaching the receiver side. In both cases, we have one transmitter and one receiver which are both located in the sea bottom. Apart from those, an additional communication link is investigated, where the water's depth is 20 m and the transmitter is not placed in the bottom, but at a height of 2 m above the bottom, thus less light is absorbed by the bottom's particles. In all configurations the beam is not transmitted directly to the receiver, but only NLOS communication is attempted.

The transmitter is regarded as a point source and its Cartesian coordinates are considered to be either (0, 0, 0) when the transmitter is at the sea bottom or (0, 0, 2) when it is placed 2 m above the bottom. It acts as a LED which transmits a light beam with wavelength 532 nm, i.e. in the green spectrum. Furthermore, we have tried a variety of elevation angles, θ_{Tr}, and aperture angles φ_{Tr}, for the transmitted light beam.

On the other side, the receiver is always located at the bottom of the sea and at a distance x from the transmitter. The distance varies according to the scenario under testing, though the distance we use in most of the simulations is 20 m. Moreover, the receiver's elevation angle is always $\theta_{Re} = \pi/2$ rad, while the receiver's *FOV* can take various values, but in most cases it is $\varphi_{Re} = \pi$ rad. To achieve the desired FOV, we regard the receiver as a round photodetector, with radius = 2 cm, covered by lenses that gather the incident light and refract it to the photodetector's surface. For instance, for realizing FOV = π the lenses should cover the area of a sphere. Therefore, the lenses along with the detector look like a hemisphere with 2 cm radius. We assume that any photon that reaches the area covered by the lenses is received by the receiver.

In the next sections we present more details on how the receiver detects the photons and how the impulse response is calculated. We also describe the three scenarios that are considered in the simulations.

3.1 Conditions of photon reception

At first, if the photon is within the receiver's plane, meaning on the photodetector's spherical area, then we consider that it has reached the receiver. Apart from that obvious case, it is possible that a photon passes the receiver's area within a step size, but at the end it gets out of the receiver's "visible area" (Image 30). In that situation, we should consider that the photon reached the receiver, as from the physical aspect, the photon would get on the photodetector plane from the moment it reaches the lenses on the receiver side. Therefore, in order to examine this case we are following the next process.

We consider the imaginary line from the photon's previous position to the current position in the three dimensional plane and we check whether this line intersects with the sphere defined for the receiver [56]. The equation of the sphere is given as

$$\left\|\vec{x} - \overrightarrow{position_{receiver}}\right\|^2 = R^2 \qquad (49)$$

where $\boldsymbol{position_{receiver}}$ is the center of the receiver's sphere, *R* is the radius of the receiver's spherical area and ***x*** is just a point on the sphere. Furthermore, the equation of a line starting from the previous photon's position, i.e. the position before the step size, $\boldsymbol{position_{photon,old}}$, with direction of the photon's trajectory $\boldsymbol{direction_{photon}}$, i.e. the direction of the considered line, is defined as

$$\vec{x} = \overrightarrow{position_{photon,old}} + d * \overrightarrow{direction_{photon}} \qquad (50)$$

where *d* is the distance along the line from the starting point and ***x*** is a point on the line. Finding the points that are on the line and on the sphere means combining the equations (49) and (50) and solving for *d*. According to [56], this is similar to solving the 2nd degree polynomial equation:

$$ad^2 + bd + c = 0 \qquad (51)$$

where:

$$a = \left\|\overrightarrow{direction_{photon}}\right\|^2 \qquad (52)$$

$$b = 2 * \left[\overrightarrow{direction_{photon}} \cdot \left(\overrightarrow{position_{photon,old}} - \overrightarrow{position_{receiver}}\right)\right] \qquad (53)$$

$$c = \left\|\overrightarrow{position_{photon,old}} - \overrightarrow{position_{receiver}}\right\|^2 - R^2 \qquad (54)$$

The discriminator of the quadratic equation (51) is defined as

$$discr = b^2 - 4 * a * c \qquad (55)$$

If *discr* ≥ 0, then the line of the photon's direction does intersect with the regarded sphere, thus the next step is to find out which of the intersecting points (if there are two points, instead of one) is closer to the photon's previous position. The distance of each point from the photon's position is calculated as:

$$d_1 = \frac{-b+\sqrt{d}}{2a}$$

$$d_2 = \frac{-b-\sqrt{d}}{2a}$$

After that, we need to figure out if this point (Point A) is on the imaginary line and lies between the photon's previous position and the photon's current position (Point B) by comparing the distance of points A and B from the photon's previous location. We should note that Point A is the first point where the line intersects with the sphere and its distance from the photon's previous location is $min(d_1, d_2)$. If the distance of this previous position from Point A is smaller than the distance from Point B (in the same direction), then we assume that the photon has passed through the receiver's visible area and therefore it is regarded as a photon that has reached the receiver. So its

current location is modified from Point B to Point A. In the other case, we assume that the photon has not reached the receiver's sphere, so it keeps moving in the sea.

Lastly, if we derive from the above flow diagram that the photon has reached the receiver's sphere, it is important to verify that the photon was within the receiver's field of view just before the last step, as well. Only then will the photon be finally considered as received. For this reason, we compute the angle between the line that passes through the photon's position and the receiver's center with the vertical line that passes through the receiver's center, since the receiver's elevation angle is 90^o (Image 30). Since we basically need to find the angle between two vectors (***ΔΦ*** and ***ΔZ***), this is calculated by their inner product, as described in [57]. Therefore, we have:

$$\overrightarrow{\Delta\Phi}\cdot\overrightarrow{\Delta Z}=\left\|\overrightarrow{\Delta\Phi}\right\|\times\left\|\overrightarrow{\Delta Z}\right\|\times\cos(\theta_p)\Longrightarrow$$

$$\cos(\theta_p)=\frac{\overrightarrow{\Delta\Phi}\cdot\overrightarrow{\Delta Z}}{\left\|\overrightarrow{\Delta\Phi}\right\|\times\left\|\overrightarrow{\Delta Z}\right\|}\Longrightarrow$$

$$\cos(\theta_p)=\frac{(x_p-x_r,y_p-y_r,z_p-z_r)\cdot(0,0,z_p-z_r)}{\left\|\overrightarrow{\Delta\Phi}\right\|\times\left\|\overrightarrow{\Delta Z}\right\|}\Longrightarrow$$

$$\cos(\theta_p)=\frac{(x_p-x_r)*0+(y_p-y_r)*0+\cancel{(z_p-z_r)}\times(z_p-z_r)}{\sqrt{(x_p-x_r)^2+(y_p-y_r)^2+(z_p-z_r)^2}\times\cancel{(z_p-z_r)}}\Longrightarrow$$

$$\cos(\theta_p)=\frac{(z_p-z_r)}{\sqrt{(x_p-x_r)^2+(y_p-y_r)^2+(z_p-z_r)^2}}\qquad(56)$$

where, (x_p, y_p, z_p) is the photon's position before the last step and the angle we need to calculate is θ_p.

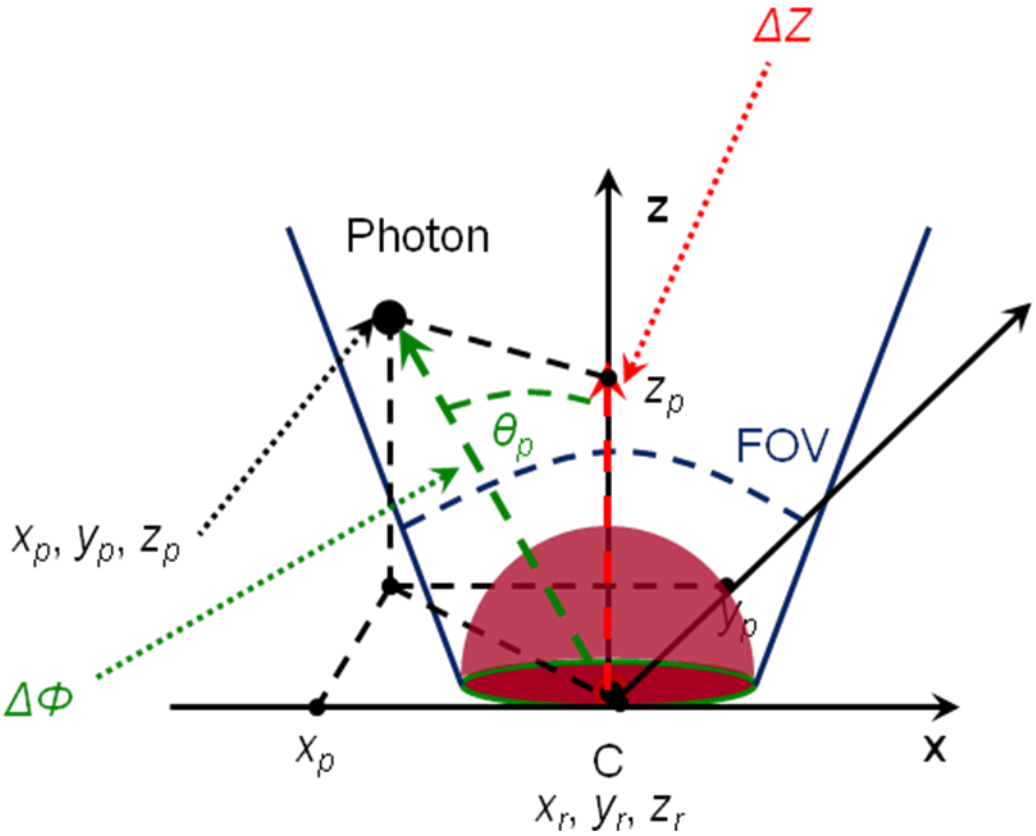

Image 30: Photon Reception within the receiver's Field of View.

If $\theta_p \leq FOV/2$ (like in Image 30), then the photon was within the receiver's FOV. Therefore, it is considered as received, meaning that its iteration in the Monte Carlo simulation will be terminated and the desired values will be saved. On the other hand, if $\theta_p > FOV/2$, then it was out of the receiver's FOV and thus it is returned to its previous position (x_p, y_p, z_p) in order to continue its iteration, until it will be either received or absorbed.

Another special case, that should be considered when examining if the photon is received, is the case where the photon reaches the sea bottom and is described in Image 31.

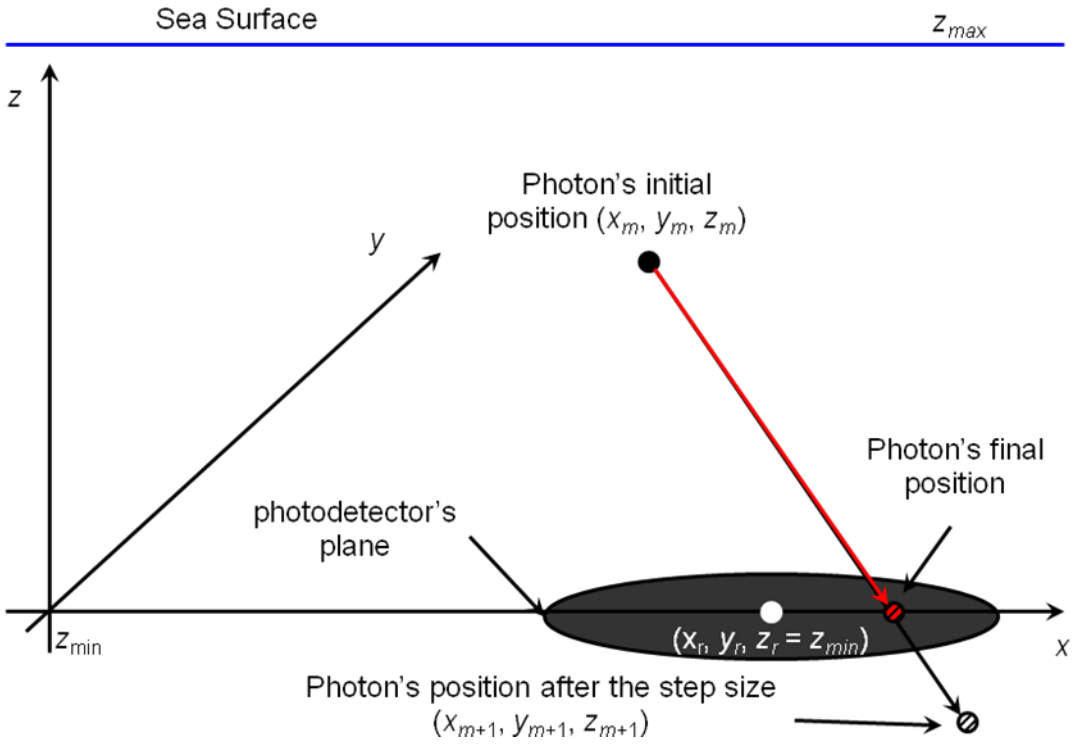

Image 31: Photon passes through the photodetector's plane on the sea bottom at a step size.

In Image 31 we notice that, after the step size, Δd, the photon goes to the position (x_{m+1}, y_{m+1}, z_{m+1}). So the new photon location is related to the previous one through the equations:

$$x_{m+1} = x_m + \mu_x * \Delta d$$

$$y_{m+1} = y_m + \mu_y * \Delta d \quad (57)$$

$$z_{m+1} = z_m + \mu_z * \Delta d$$

However, if the photon reached the position (x'_m, y'_m, z_{min}), then the distance that the photon would have traveled from (x_m, y_m, z_m), based on the calculated direction vector (μ_x, μ_y, μ_z), would be

$$z_{min} = z_m + \mu_z * \Delta d' \Rightarrow$$

$$\Delta d' = \frac{z_{min} - z_m}{\mu_z} \quad (58)$$

Finally, we consider that the photon arrived at the position (x'_m, y'_m, z_{min}). In our examples we have defined that z_{min} = 0. Taking also into account that the photodetector's boundaries are

$$(x - x_r)^2 + (y - y_r)^2 \leq r^2$$

then we have to check whether the equation bellow for photon's last position is true

$$(x'_m - x_r)^2 + (y'_m - y_r)^2 \leq r^2 \quad (59)$$

If Equation (59) is true, then the photon is received when FOV = 180^o. When FOV < 180^o one more step is required by checking if the photon was within the FOV, when it was at position (x_m, y_m, z_m) as mentioned above. Otherwise (Equation (59) is false), the photon is outside the detector's area and thus it should follow the process of internal reflection, as described in Section 2.2.4.

3.2 Channel impulse response design

In order to design the channel impulse response for a specific simulation scenario, we need to know the weight of each photon at the moment this exact photon reached the receiver as well as the exact moment that it was received in terms of the beginning of transmission which was considered as the beginning of time. More specifically, as mentioned in the Monte Carlo description, we consider that each photon is inserted into the medium at time t = 0 sec. Then, in each step size Δd, we derive the distance that a photon has travelled, which is equal to Δd, and then, considering that the light speed in water, denoted as c, is known, we calculate the time interval that the photon needs to travel that distance by dividing $\Delta d / c$. At the end of a photon's iteration, and only if the photon is received, we sum up all these calculated times, extracting this way the interval that the photon needed to travel from the transmitter to the receiver, i.e. the moment that the photon was received. Concerning the photon's weight, this is saved for each received photon. As it is expected, this is applied for all photons, thus at the end of the simulation we know for all transmitted photons the moments and their weights when they were received.

As soon as we have all we need for the Channel Impulse Response (CIR) diagram, we are ready to proceed with its design. Basically, the CIR is considered as the histogram of received intensity versus the propagation time. With this in mind, the total time is divided in time intervals of td seconds and for each one we sum the weight of photons with propagation time inside this interval. Below is an example of a histogram (Image 32).

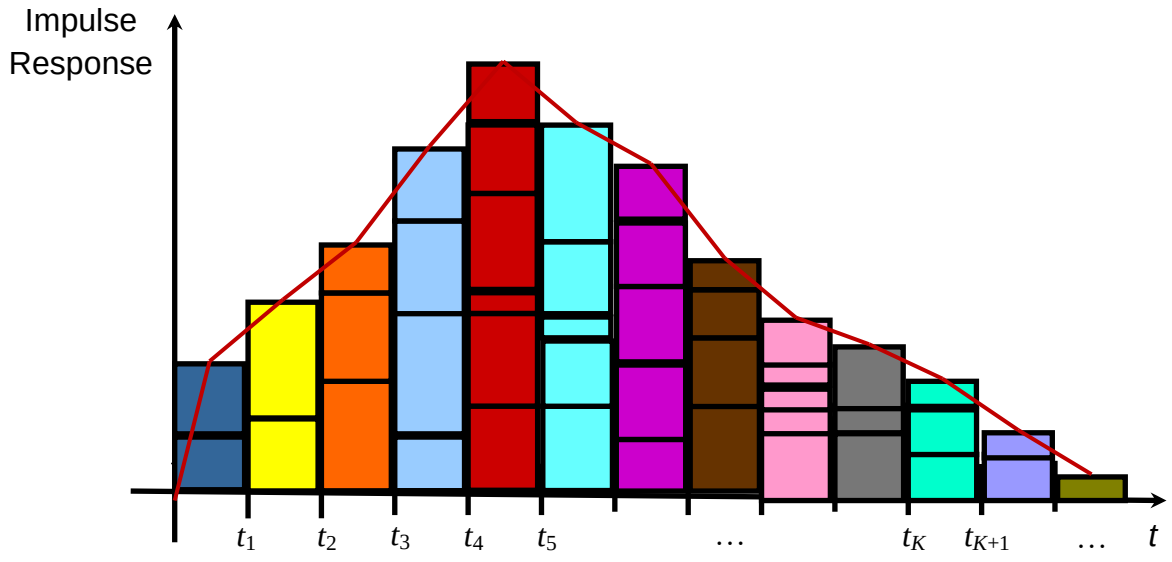

Image 32: Histogram for the impulse response.

For example, in the time interval between t_1 and t_2 two photons have reached the receiver. The heights of each of the two parallelograms correspond to the weight of each photon. So, the second photon was reached with a greater weight. The sum of the weights inside the same interval gives the value of the impulse response for this interval. Once the histogram is derived, the impulse response diagram is designed by joining the centers of each interval, as shown by the red line in Image 32 in order to obtain a rough estimation of the impulse response.

Therefore, taking into consideration the above observations, the first step is to identify which is the maximum time that a photon had to travel from the source to the destination point, t_{max}. Next, this time will be divided in smaller parts by a predefined -factor. This factor is called *partition* and varies according to the number of received photons and the t_{max} value. In our simulation, its value was manually set, based on experimental tests, in order to get an as precise as possible diagram for the CIR estimation. As soon as the partition is decided, we calculate the number of partitions, M, by

$$M = ceiling\left(\frac{t_{max}}{partition}\right) \qquad (60)$$

For each partition, i.e. for the times between t_i and t_{i+1}, we sum up the total power of the photons that are received within this interval, i.e. the sum of the weights of the photons, and we place it in the middle of these intervals. In such a way, the impulse response diagram is obtained.

3.3 Simulation scenarios

In the following paragraphs we are describing with more details all the scenarios that have been simulated in our work. Firstly, it is worth mentioning that in all of the scenarios there are some parameters that never change. These are the bellow ones:

- Wavelength, λ = 532 nm
- Refractive index of water (corresponding to the above wavelength), n_{water} = 1.333 [58]
- Refractive index of air, n_{air} = 1
- Refractive index of sea bottom, n_{bottom} = 1.45
- HG constant, g = 0.924
- Number of transmitted photons, $N = 10^6$
- Probability of surviving in roulette (in Monte Carlo Method), $roulette_{probability}$ = 10%
- Threshold for each photon's weight, $weight_{thr} = 10^{-4}$. When a photon's weight is below this threshold, then the roulette process is initiated for this photon.
- Receiver's elevation angle: $\theta_{Re} = 90^o$.

The input parameters for each scenario are presented in Table 5.

Table 5: Standard input parameters for the simulating scenarios

Parameter	1st scenario	2nd scenario	3rd scenario
Wavelength (nm)	532	532	532
n_{water}	1.333	1.333	1.333
n_{air}	1	1	1
n_{bottom}	1.45	1.45	1.45
Depth (m)	200	10	20
HG constant	0.924	0.924	0.924
No of photons	10^6	10^6	10^6
Survival probability in roulette method (%)	10	10	10
Threshold for photon's weight	10^{-4}	10^{-4}	10^{-4}
Transmitter's position (m)	[0, 0, 0]	[0, 0, 0]	[0, 0, 2]
Receiver's position (m)	[0, 0, 0]	[0, 0, 0]	[0, 0, 0]
Receiver's elevation angle	90^o	90^o	90^o

In all of our simulations we calculated two basic parameters, the received intensity and percentage of received photons. The intensity is computed as:

$$intensity = 10\log\left(\frac{total\ received\ power}{N}\right) \qquad (61)$$

where the total received power is the sum of the received photons' weights.

Moreover, for some of our simulation setups we derived the impulse response diagram. Specifically, this was implemented for coastal and turbid water environments only, as the strongest intensity was received for these cases, for various distances between the transmitter and the receiver, from 10 m to 50 m. For these scenarios, the sea depth was 10 m and both nodes were located at the sea bottom. The transmitted optical beam had 45^o elevation angle and 60^o divergence angle, while the receiver has a 90^o elevation angle and 180^o field of view. The last difference between this type of simulations and the other ones is that in this case a larger number of photons were transmitted, particularly $N = 3 \times 10^6$ photons, in order to increase the received intensity and thus improve the impulse response design.

3.3.1 1st scenario: Deep waters

In this scenario, we assumed that the communication link was demonstrated in deep sea where the depth was equal to 200 m. The constant parameters for this simulation setup were the following:

- Depth, z_{max} = 200 m
- z coordinate for the two communicating nodes: 0 m
- Transmitter's location, $posotion_{Tr}$ = [0, 0, 0]

This scenario was further divided in sub-scenarios, where one input parameter, like the transmitter's elevation angle, was variable, while the rest of them were kept unmodified. More specifically, we have considered the following sub-cases.

1. **Case a**: Only the transmitter's elevation angle, θ_{Tr}, was varied. In this simulation, a variety of angles for θ_{Tr} were applied, from 20^o to 90^o, whereas the transmitter's and receiver's aperture angles remained constant, with values $\varphi_{Tr} = 60^o$ and $\varphi_{Re} = 180^o$. Moreover, the distance between transmitter and receiver was always 20 m, thus the receiver's coordinates were $posotion_{Re}$ = [20, 0, 0].
2. **Case b**: Only the transmitter's aperture angle, φ_{Tr}, was varied. In this simulation, we used various values for φ_{Tr}, from 15^o to 60^o, whereas the rest of transmitter's and receiver's angles remained the same. Particularly, we set $\theta_{Tr} = 45^o$ and $\varphi_{Re} = 180^o$. Finally, as in the previous case, the distance between transmitter and receiver was always 20 m.
3. **Case c**: Only the transmitter's aperture angle, φ_{Tr}, was varied, whereas the distance between the transmitter and the receiver was 40 m. This is similar to the last case, but in this simulation the receiver is located at $position_{Re}$ = [40, 0, 0].
4. **Case d**: Only the distance between the transmitter and the receiver was modified. In this case, the distance of the nodes took values between 10 m and 100 m. As for the angles, they were always the same and their values were $\theta_{Tr} = 45^o$, $\varphi_{Tr} = 60^o$ and $\varphi_{Re} = 180^o$.
5. **Case e**: Only the receiver's FOV, φ_{Re}, was modified. In this simulation, we change the values of φ_{Re}, from 60^o to 180^o, whereas the other parameters were always the same. Specifically, transmitter's elevation and aperture angles were $\theta_{Tr} = 45^o$ and $\varphi_{Tr} = 60^o$, respectively. As for the distance between transmitter and receiver, it was set to 20 m. We should mention that despite the fact that in all of the above simulations we considered all four water types, in this case study we simulated only the coastal and turbid water environments. This decision was based on the observation that for pure and clear waters the received power intensity was already too low and it would further decrease if the receiver's FOV was reduced. Therefore, these configurations had no practical interest and this was the reason why we did not take them into account.

3.3.2 2nd scenario: Shallow waters

In this scenario, it was assumed that the communicating nodes were located in a shallow water environment, i.e. at 10 m depth. The constant parameters for this simulation were the following:

- Depth, z_{max} = 10 m
- z coordinate for the two communicating nodes: 0 m
- Transmitter's location, $posotion_{Tr}$ = [0,0,0]

As in the 1st scenario, this one was also divided in sub-cases, where we modify one input parameter each time, whereas the others were kept constant. More specifically, we considered the sub-cases mentioned below.

1. **Case a**: Combinations of transmitter's aperture angle, φ_{Tr}, and elevation angle θ_{Tr}. We investigated various values for the angles of φ_{Tr} and θ_{Tr}, where φ_{Tr} was either 30^o or 60^o and θ_{Tr} varied from 20^o to 90^o. In all cases, the distance between the nodes was 20 m.

2. **Case b**: Only the transmitter's aperture angle, φ_{Tr}, was varied. This is similar to the Case b: Only the transmitter's aperture angle, φ_{Tr}, was varied. In this simulation, we used various values for φ_{Tr}, from 15^o to 60^o, whereas the rest of transmitter's and receiver's angles remained the same. Particularly, we set $\theta_{Tr} = 45^o$ and $\varphi_{Re} = 180^o$. Finally, as in the previous case, the distance between transmitter and receiver was always 20 m. of the 1st scenario.
3. **Case c**: Only the distance between transmitter and receiver was changed. This was similar to the Case d: Only the distance between the transmitter and the receiver was modified. In this case, the distance of the nodes took values between 10 m and 100 m. As for the angles, they were always the same and their values were $\theta_{Tr} = 45^o$, $\varphi_{Tr} = 60^o$ and $\varphi_{Re} = 180^o$. described in Section 0.
4. **Case d**: Only the receiver's FOV, φ_{Re}, was modified. This is similar to the Case e: Only the receiver's FOV, φ_{Re}, was modified. In this simulation, we change the values of φ_{Re}, from 60^o to 180^o, whereas the other parameters were always the same. Specifically, transmitter's elevation and aperture angles were $\theta_{Tr} = 45^o$ and $\varphi_{Tr} = 60^o$, respectively. As for the distance between transmitter and receiver, it was set to 20 m. We should mention that despite the fact that in all of the above simulations we considered all four water types, in this case study we simulated only the coastal and turbid water environments. This decision was based on the observation that for pure and clear waters the received power intensity was already too low and it would further decrease if the receiver's FOV was reduced. Therefore, these configurations had no practical interest and this was the reason why we did not take them into account. of the scenario in Section 0.

3.3.3 3rd scenario: Elevated transmitter

In this last scenario, we assumed that the nodes were located in a sea with 20 m depth. The difference from the previous scenarios was that the transmitter was elevated and placed 2 m above the sea bottom. Therefore, the constant parameters in this scenario were:

- Depth, z_{max} = 20 m
- Transmitter's location, $posotion_{Tr}$ = [0, 0, 2]
- z coordinate for the receiver: 0 m

The sub-cases considered in this simulation are the same as the ones presented in Section 5.

4. SIMULATION RESULTS

In this section we present the intensity as well as the impulse response diagrams that were extracted from the simulations we realized. In the end of each section we comment on the experimental results and we derive some conclusions.

4.1 Results for 1st and 2nd scenarios

For the two first scenarios, which differ only in the depth that is set for the sea, we are extracting the intensity diagrams. More specifically, the values of the particular system parameters whose effect is investigated in each case are placed on the horizontal axis, whereas the corresponding intensity values are placed on the vertical axis (in dB). Namely, the system parameters that are taken into consideration are the transmitter's beam elevation angle, the transmitter's beam aperture angle, the distance between transmitter and receiver and the receiver's Field of View.

4.1.1 Effect of the transmitter's elevation angle

In this section, we study the impact the transmitter's elevation angle has on the received intensity. Figures Figure 1and Figure 2 depict the diagrams of intensity vs. the elevation angle for the two first scenarios, where the investigated values for the elevation angles are 20^o, 45^o, 60^o, 90^o in Figure 1 and Figure 2 in the case of $\varphi_{Tr} = 30^o$, whereas in the last case (when $\varphi_{Tr} = 60^o$ in Figure 2) the investigated values for the elevation angles are 45^o, 60^o, 90^o. From Figure 1 we notice that, after the 45^o, as the elevation angle is increased, the intensity seems almost constant. In reality, it is reduced with a slow rate. This is due to the fact that the beam direction is not in line of sight with the receiver. The lower the elevation angle is, the more it approximates the line of sight configuration. The large depth did not allow many reflections at the water-air interface. Therefore, the non-line-of-sight regime imposed the intensity decrease with slow rate for the large elevation angles.

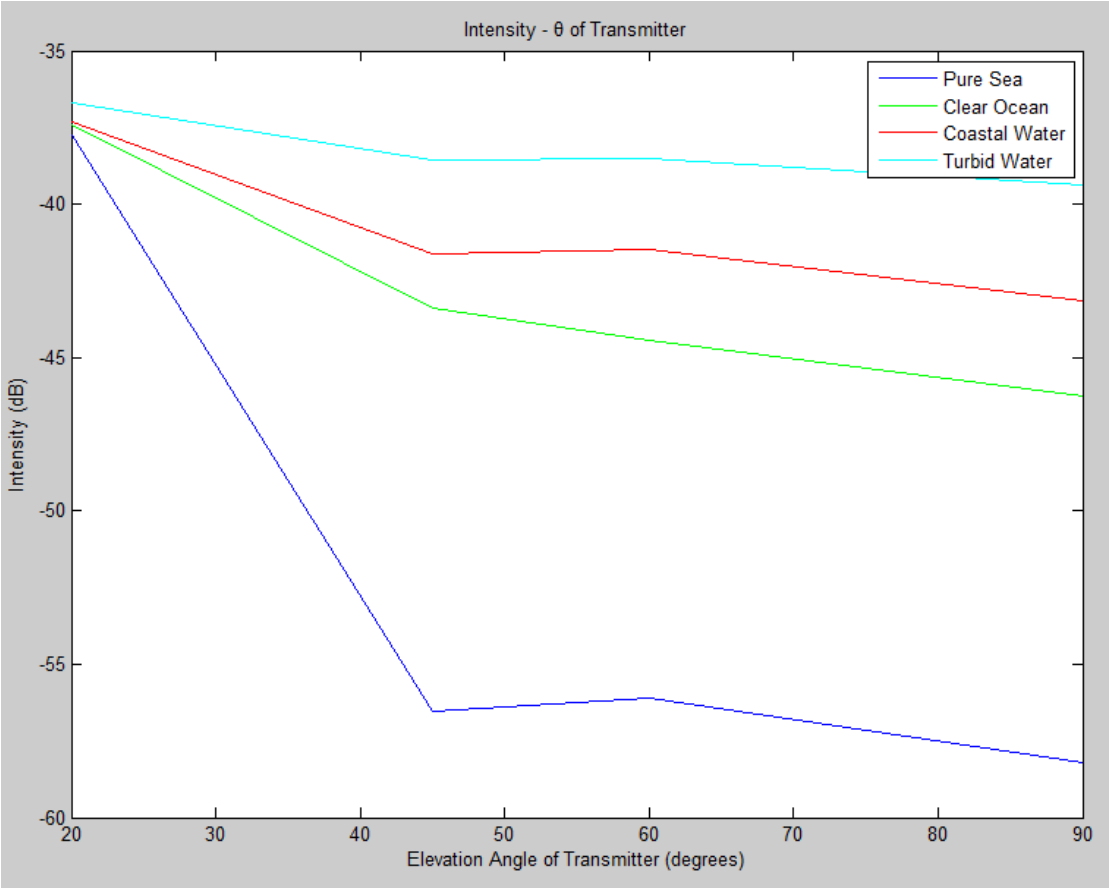

Figure 1: Intensity vs. transmitter's elevation angle for d = 20 m and depth = 200 m.

Generally, the received power is higher when the divergence angle is 60^{o} (Figure 2) due to the larger volume created by the divergence angle of the source's beam and the receiver's FOV. To be more specific, concerning clear, coastal and turbid environments, we notice that the intensity is maximized when the elevation angle is 45^{o}. This is owed to the fact that in these water types a component of the optical beam at 45^{o} elevation angle (in the center of the beam) will be reflected at the sea-air surface and will be guided directly to the receiver. On the other hand, about clear water, the maximum of the intensity was reached when the elevation angle is 60^{o}. This is again owed to the link geometry. The pure water imposes mild scattering and allows more reflections at water-boundaries. More components of the optical beam will be reflected at the water-air boundary even more than two times and will be then guided to the receiver. It is worth mentioning that the intensity is almost the same in the following two cases:

- Turbid water: Divergence angle is 30^{o} and the elevation angle is 60^{o}
- Pure water: Divergence angle is 60^{o} and the elevation angle is 60^{o}

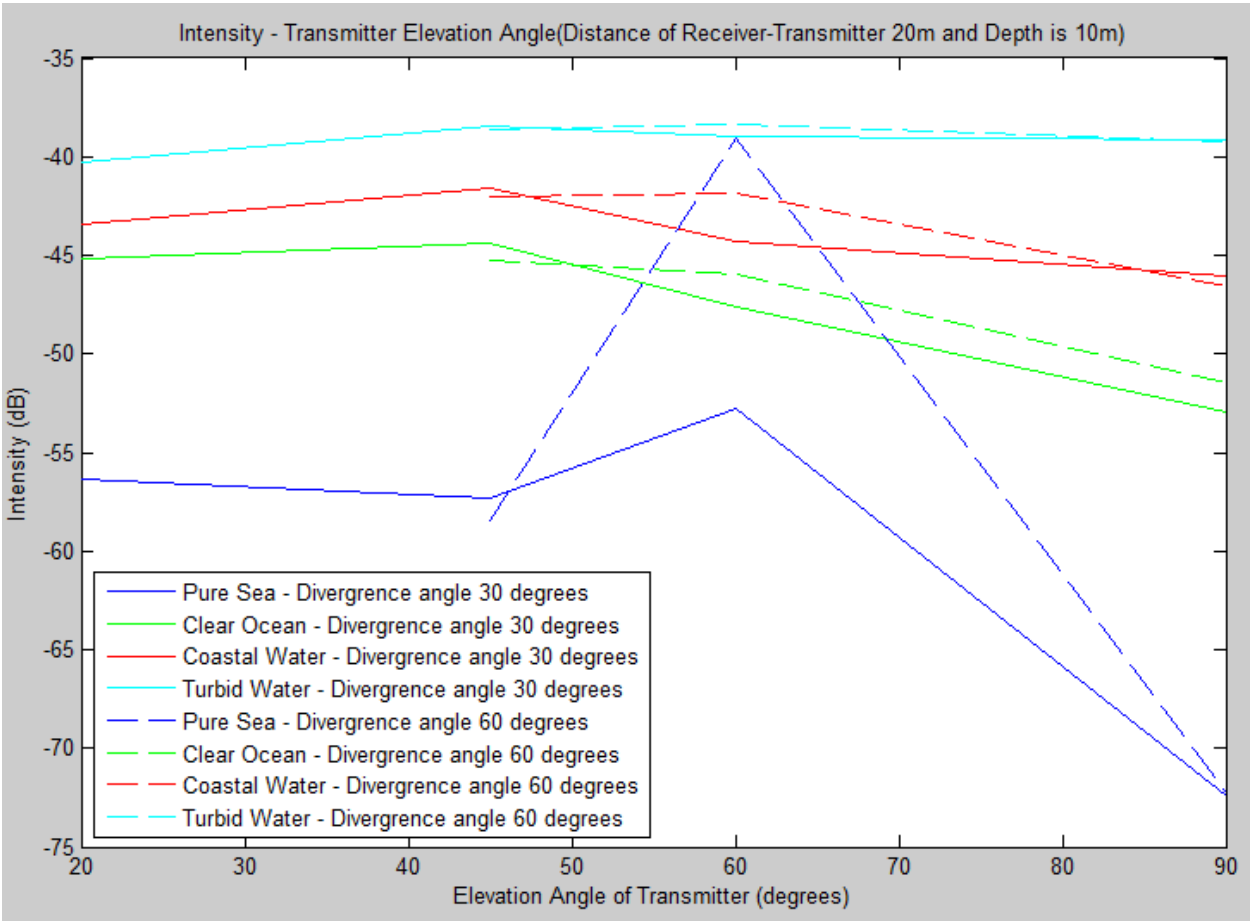

Figure 2: Intensity vs. transmitter's elevation angle for d = 20 m and depth = 10 m.

Moreover, from Figures Figure 1 and Figure 2, we note that in the case of turbid water, the intensity is changed smoother because the photon's direction is totally different from the initial one after a high amount of scattering events.

Lastly, the influence of the depth is more obvious when we examine the cases of pure water. In this case, when the elevation and the divergence angle of transmitter are both 60^o, then the received power is much greater at 10 m depth compared to the one at 200 m depth. This was owed to the geometry of the link as already explained above.

4.1.2 Effect of the transmitter's aperture angle

In this section, we present the diagrams of intensity versus the transmitter's aperture angle for the two first scenarios. Apart from the effect of water's depth, we also take into consideration the impact of the distance between the transmitter and the receiver for the deep water scenario, as illustrated in Figure 3. The examined values for the aperture angle were 15^o, 20^o, 25^o, 30^o, 45^o, 50^o, 60^o for distance between transmitter and receiver equal to 20 m. When distance was 40 m, the same values were considered, except for $\varphi_{Tr} = 15^o$. In Figure 3, regarding the same channel conditions, it is noted that the intensity is always higher when the receiver is 20 m away from the transmitter in comparison with the case where this distance is 40 m. Overall, we do not observe great fluctuations in the received power as the transmitter aperture angle is increased due to the "memoryless" transitions after each scattering event for each photon. Additionally, the transmitter elevation angle of 45^o created a link configuration that didn't affect the results significantly. This is also verified in Figure 2 for all the water types at 45^o

elevation angle and both divergence angles of the transmitter, where the modifications after changing the divergence angle is insignificant for each water type case. Another notice is that in most cases where the distance between the transmitter and receiver is 20 m, the intensity is maximized near 30^o, whereas for angles greater than 30^o the intensity is almost the same.

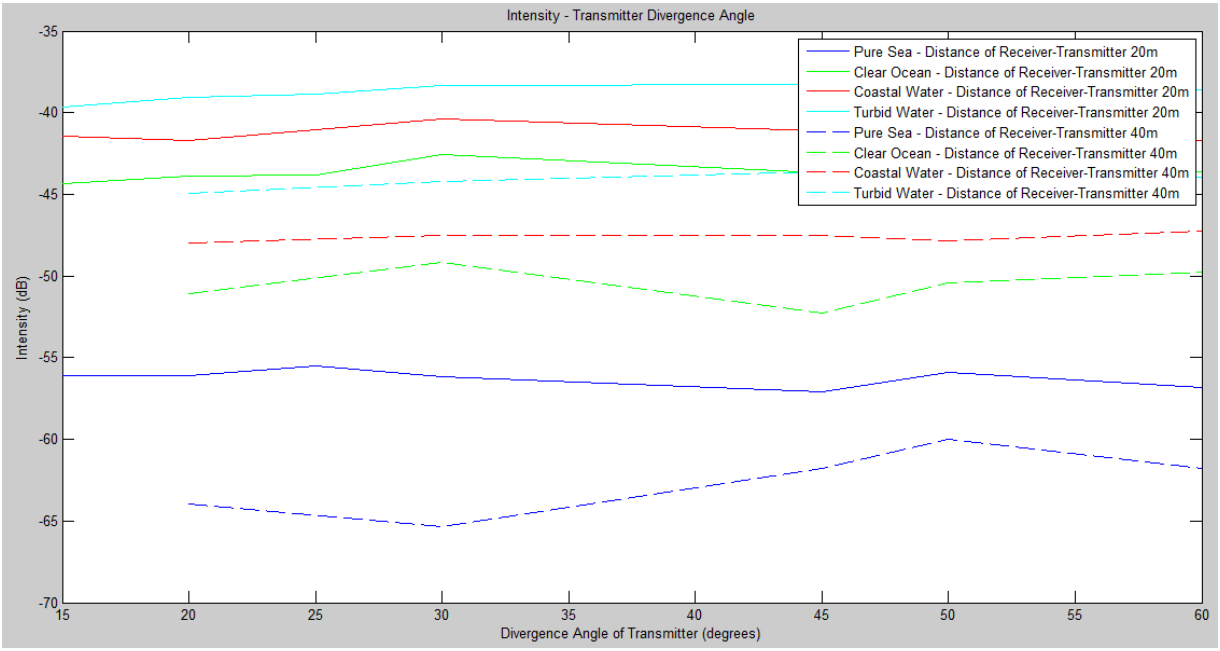

Figure 3: Intensity vs. transmitter's aperture angle for depth = 200 m and distance of transmitter – receiver set to 20 m and 40 m.

In Figure 4, the combined effect of the water's depth and divergence angle of the transmitter is presented. Particularly, the impact of the depth is more obvious for the pure sea environment, due to the plenty of reflections in the water – air surface. For pure sea, the larger number of reflections at both ends (water-air, water-bottom interfaces) at 10 m depth led to lower intensity level for divergence angle up to 50^o. The larger divergence angle of 60^o changes the configuration geometry of the link and favors the shallow waters case. However, as the water becomes more turbid, the depth's impact is reduced. The maximum intensity (-37.9362 dB) appeared for turbid waters when the depth is 10 m and the transmitter's aperture angle is 60^o. Furthermore, there are cases where the intensity is larger for deep waters, instead of shallow waters. This fact appears in turbid water environment and in the same transmitter's divergence angle.

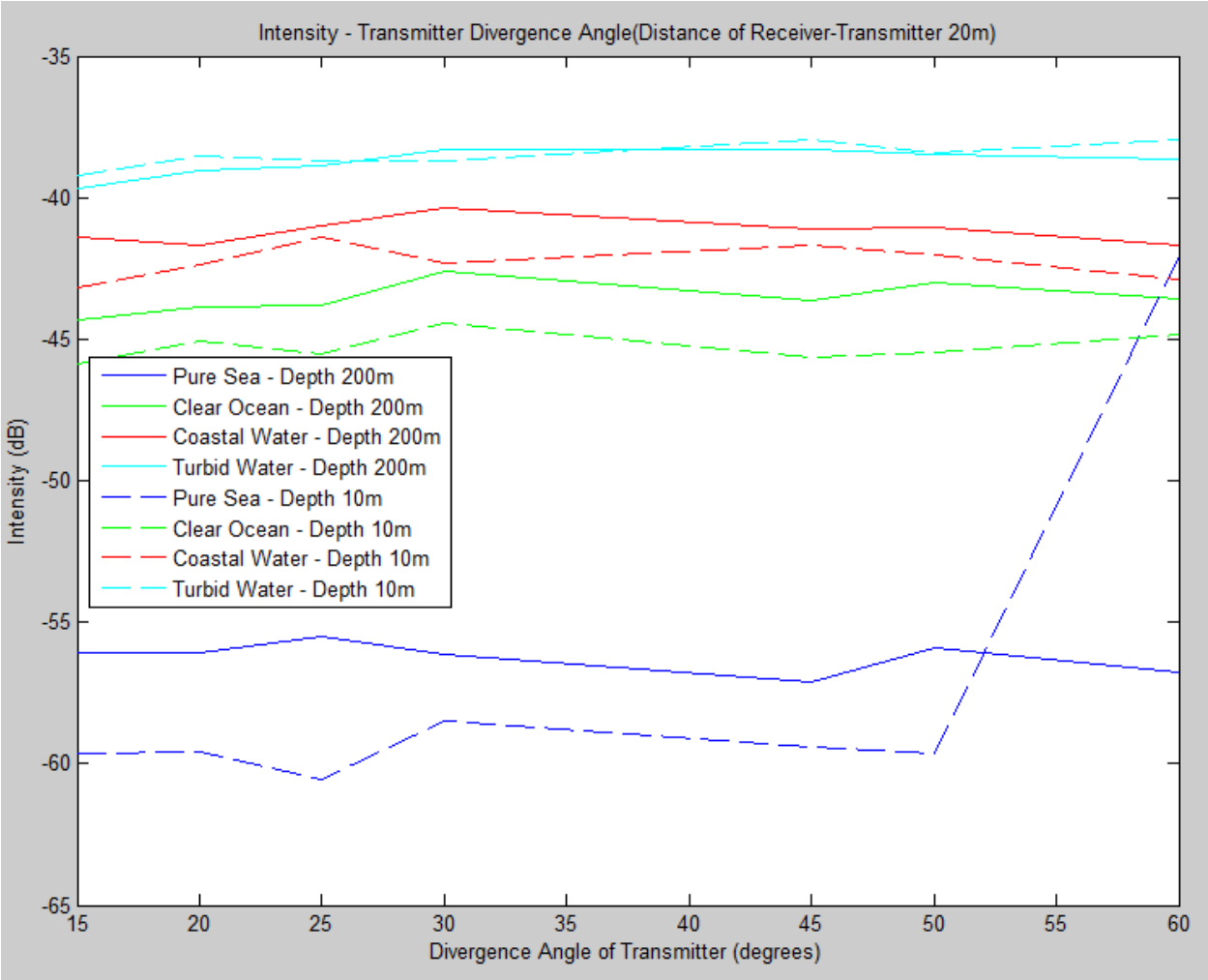

Figure 4: Intensity vs. transmitter's aperture angle for depth = 200 m and 10 m and distance of transmitter – receiver set to 20 m.

4.1.3 Effect of the transmitter's and the receiver's distance

The following Figures represent the impact of the distance between the two communicating nodes for all environments and for scenarios 1 and 2. The distance varies from 10 m to 100 m, with step 10 m.

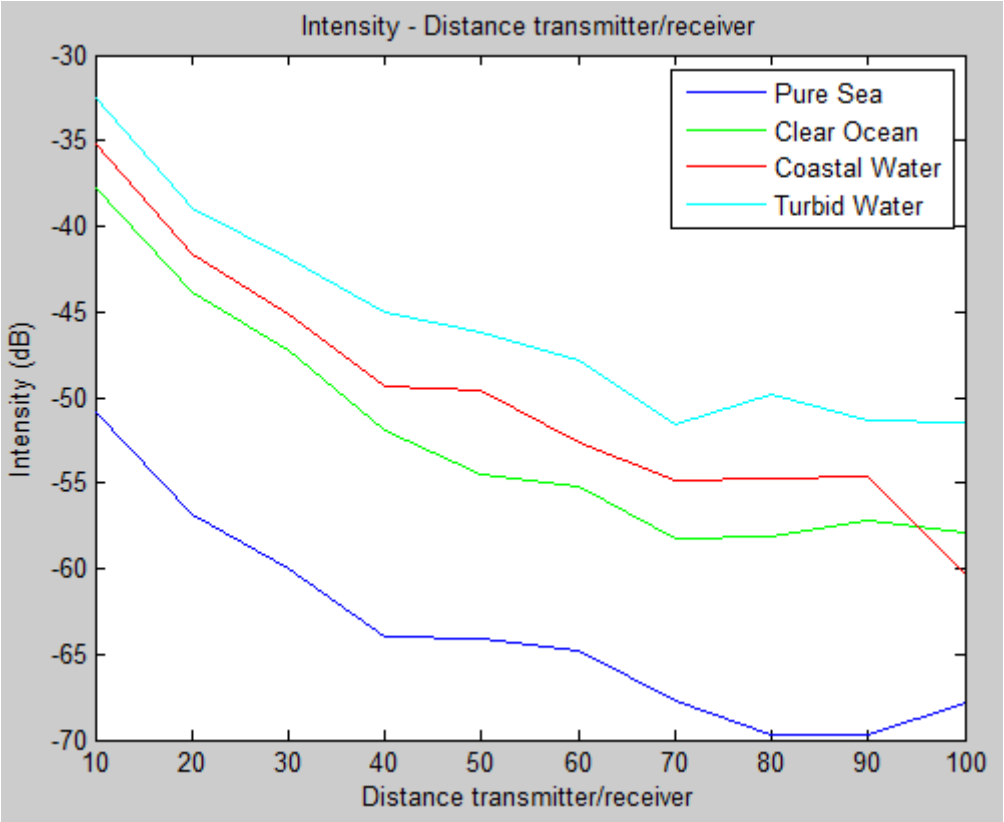

Figure 5: Intensity vs. Distance between transmitter and receiver for depth = 200 m.

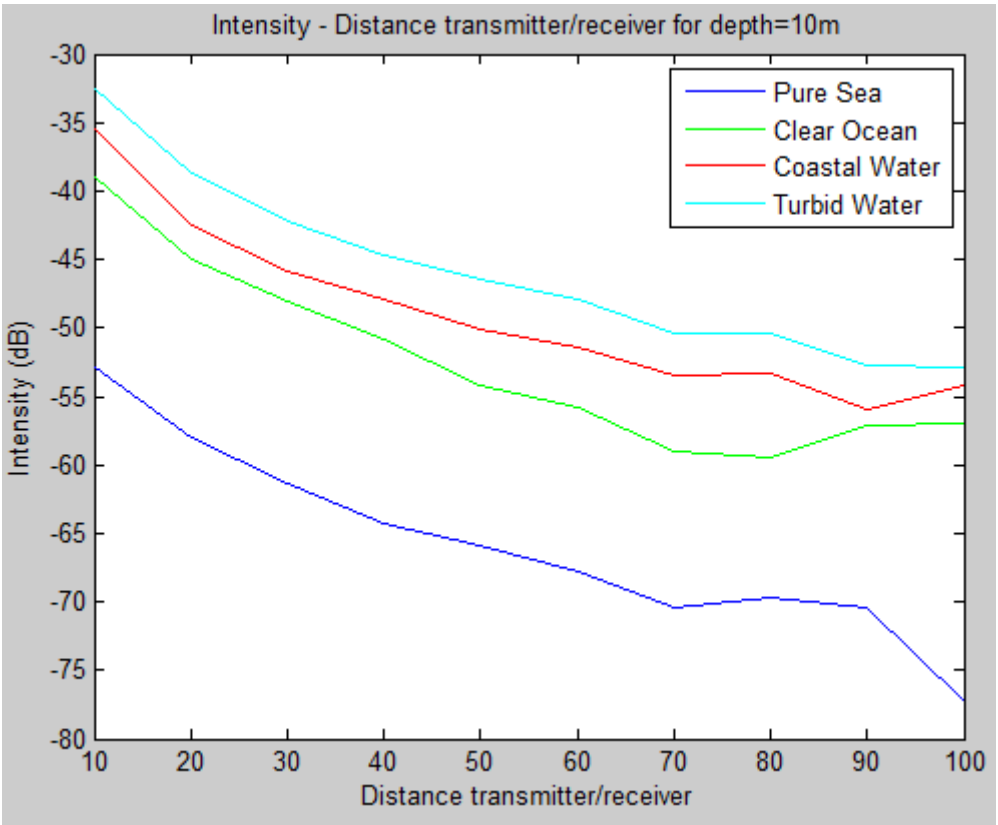

Figure 6: Intensity vs. Distance between transmitter and receiver for depth = 10 m.

In general, the higher the distance between the transmitter and the receiver, the lower the intensity gets. Concerning all environments, the maximum of the intensity is reached

when the examined distance is 10 m. Another notable comment is that the intensity for distance 100 m in turbid water is slightly higher than the one for distance 10 m in pure water. For example, for shallow waters (Figure 6) the intensity is -52.8493 dB for 100 m distance in turbid waters and -52.9241 dB for 10 m distance in pure waters. Finally, even though the results seem to be slightly better for deep waters compared to shallow waters, the differences in the intensity values are very small and in some cases almost negligible between the two scenarios. Therefore, the water depth has a minimum impact on the relation between the received intensity and the distance.

4.1.4 Effect of the receiver's FOV

Lastly, the impact of the receiver's FOV in the first two scenarios is studied in this chapter. The considered FOV values vary from 60^o to 180^o, with step 30^o. Concerning the comparison between the two scenarios, it is noted that the depth affects more strongly the intensity in the coastal water environment (Figure 7). Regarding this environment, when the depth is higher, the intensity is increased. When the receiver's FOV is 160^o, the received intensity is the same for the below cases:

- Turbid water: depth 200 m or 10 m
- Coastal water: depth 10 m

We also notice that the intensity is maximized when we examine turbid water with receiver's FOV 180^o and depth 200 m (or 10 m). Despite the fact that the received power is greater in turbid environment compared to coastal water type in the cases studied above, in this scenario the intensity is larger for smaller than 160^o FOV angles in coastal environment. The large FOV (more than 160^o) favors the more intense scattering in turbid water. For lower FOV angles, the larger number of scattering events led to higher losses in order the photons to be received, resulting in higher intensity levels for the coastal water case.

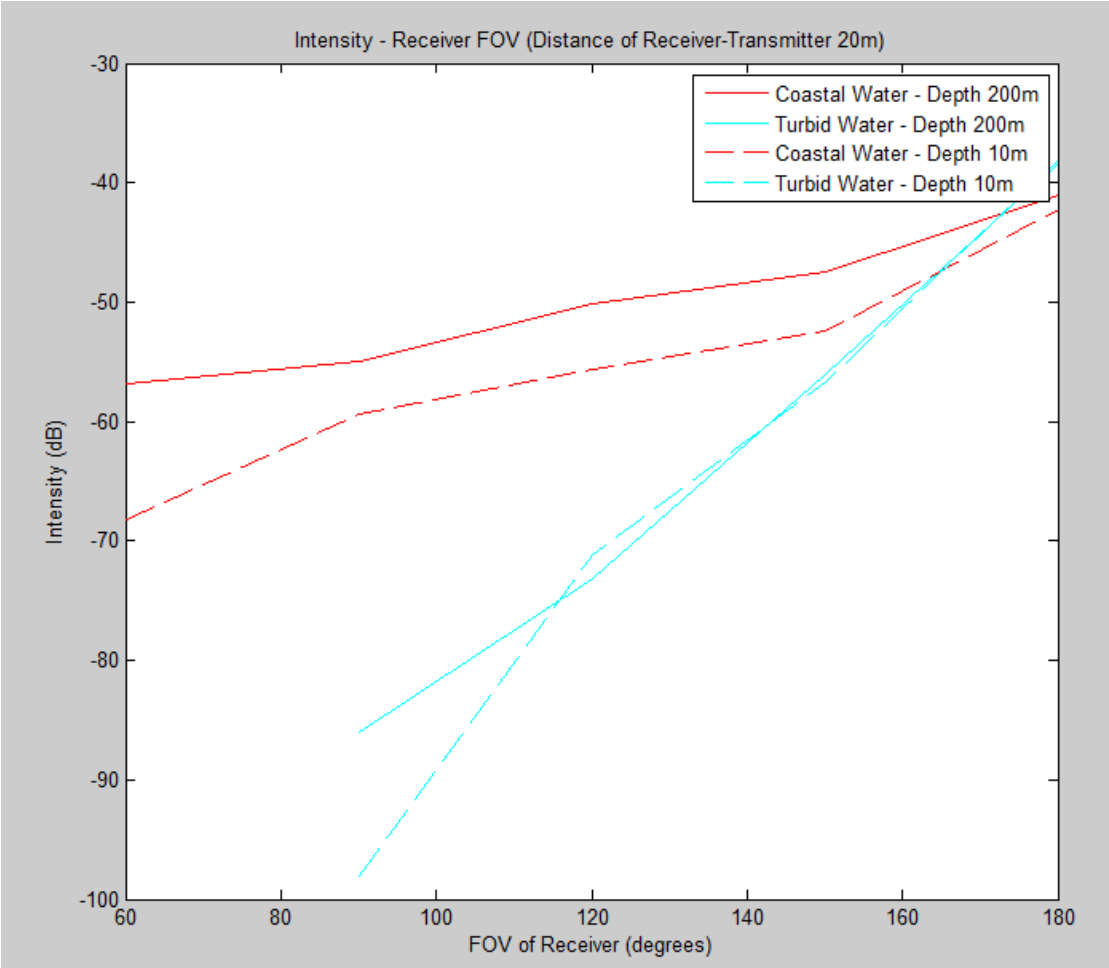

Figure 7: Intensity vs. receiver's FOV for depth = 200 m and 10 m and distance of transmitter – receiver set to 20 m.

To conclude, on the one hand, the large receiver's FOV provides better results on the intensity when we examine turbid water. On the other hand, the small receiver's FOV gives better results on the intensity in coastal water case, compared to the turbid water.

4.2 Results for 3rd scenario

In the next paragraphs we present the extracted intensity diagrams for the third scenario, were the transmitter is elevated 2 m above the sea bottom and the sea's depth is 20m.

4.2.1 Effect of the transmitter's elevation angle

Starting with the transmitter's elevation angle, the observations of this scenario are similar to the ones mentioned in Section 4.1.1. Particularly, for clear ocean, coastal and turbid water environments, the intensity hardly changes by the variation of the elevation angle, θ_{Tr}. Its value for coastal and clear waters is maximized at θ_{Tr} = 45°, while for turbid environment the intensity is maximized at θ_{Tr} = 20° and φ_{Tr} = 30°. Moreover, as shown in Figure 8, in most cases the intensity is higher when the divergence angle is 60°, compared to the corresponding cases where the divergence angle is 30°. This is

true for $55^o < \theta_{Tr} < 90^o$ in clear ocean and almost for $\theta_{Tr} > 45^o$ in the other three water types.

However, regarding pure sea, the power intensity does not take its maximum value when $\theta_{Tr} = 60^o$, as it does for the second scenario (Figure 2). On the contrary, not only the power is maximized when $\theta_{Tr} = 20^o$ and $\varphi_{Tr} = 30^o$, but also this value is very close to the corresponding value for the turbid environment. Furthermore, these angles achieve the strongest received power for pure waters, compared to the first and second scenarios where the transmitter's elevation angle is also examined (Section 4.1). For the non-pure water environments, the results have almost the same behavior as the one shown in Section 4.1, especially for the part $\theta_{Tr} > 50^o$, where estimations of intensity were computed for both $\varphi_{Tr} = 30^o$ and $\varphi_{Tr} = 60^o$.

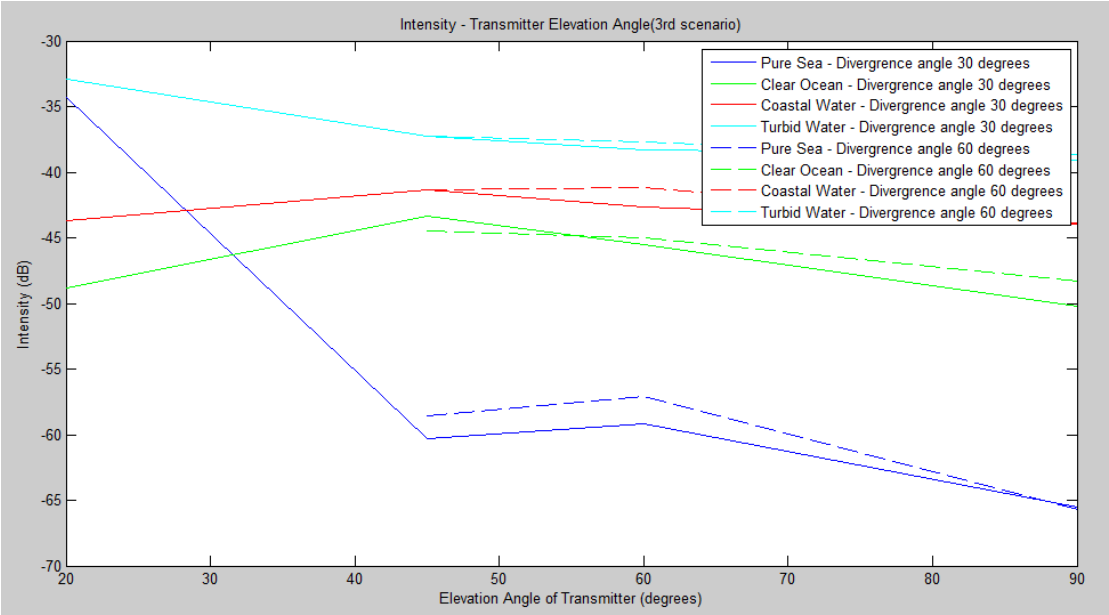

Figure 8: Intensity vs. transmitter's elevation angle for the 3rd scenario.

4.2.2 Effect of transmitter's aperture angle

Figure 9 depicts the diagram of the received intensity versus the transmitter's aperture angle for 3rd scenario. From this figure, it is clear that, for the pure water case, the intensity's fluctuations are less severe compared to the fluctuations in the second scenario (Figure 4). We also note that for the current scenario the received power for pure water is maximized when the transmitter's aperture angle is 25^o, contrary to the first and second scenarios, where the maximum values are observed for $\varphi_{Tr} = 50^o$ and 60^o, for 200 m and 10 m, respectively. For the rest water environments, among three scenarios, i.e. when the depth is equal to 200 m, 10 m and 20 m with an elevated transmitter, the results have almost the same behavior, as it can be verified by Figure 9 and Figure 4.

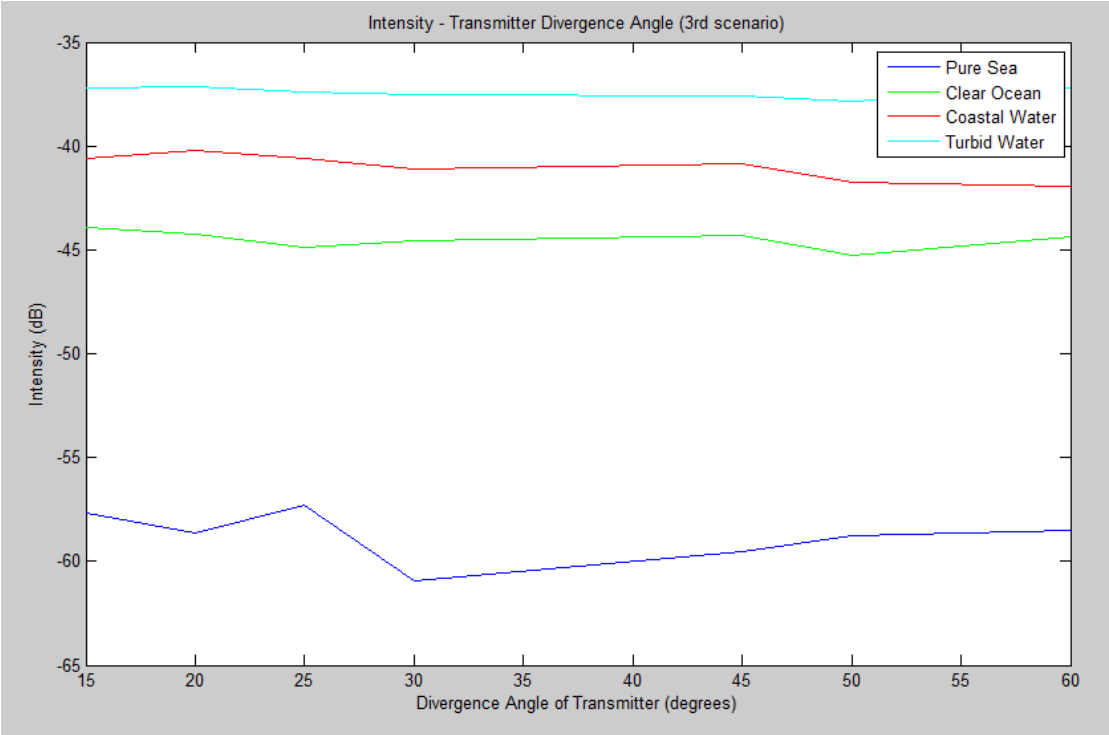

Figure 9: Intensity vs. transmitter's aperture angle for the 3rd scenario.

4.2.3 Effect of the transmitter's receiver distance

In Figure 10, we study the effect of the distance between transmitter and receiver for the third simulated scenario. The observations for this scenario are similar to the observations of the previous two scenarios, as mentioned in Section 4.1.3. In summary, we have noticed that the intensity is reduced as we increase the transmitted distance, as well as for turbid water we have stronger received power in comparison to the other environments and thus it can support longer ranges.

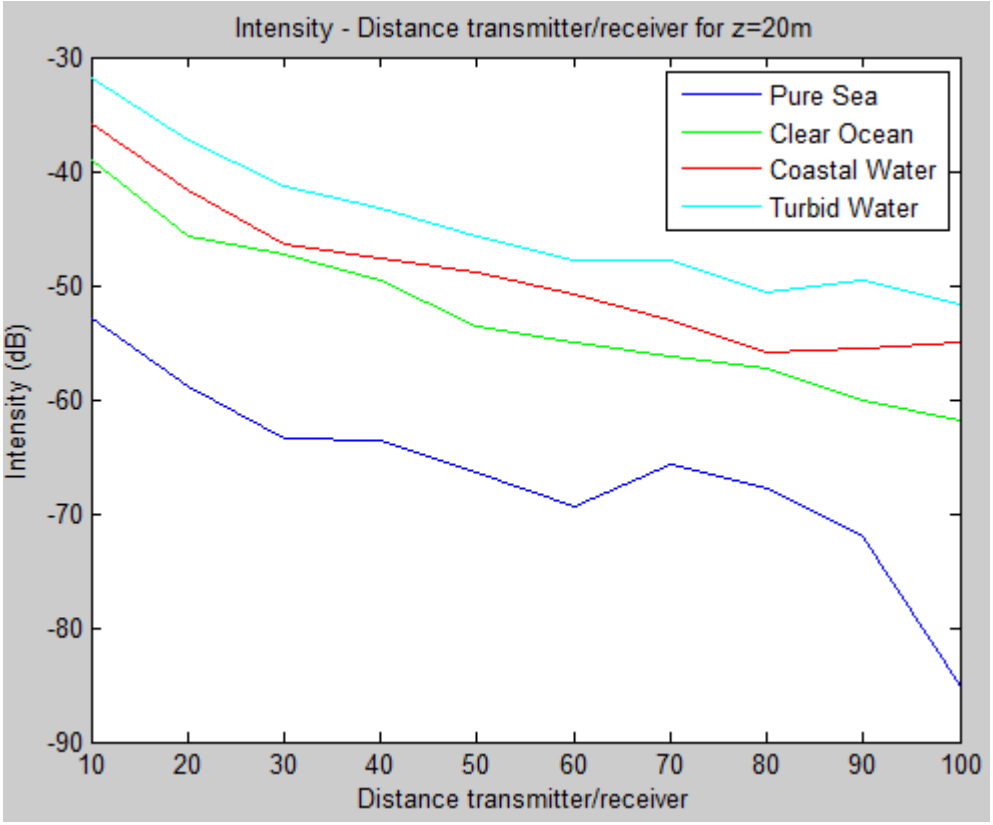

Figure 10: Intensity vs. Distance between transmitter and receiver for the 3rd scenario.

All in all, among three configurations the value of the received intensity is almost the same for a specific distance and water environment (Figure 5, Figure 6 and Figure 10). Therefore, it is concluded that when we move from one simulating scenario to another, the performance, with respect to the received intensity, can be noticeably improved only if we adjust the transmitter's elevation and/or aperture angle. If we modify only the distance between the transmitter and the receiver, then the performance slightly changes for the third scenario, where the intensity tends to decrease, especially in the pure water environment.

4.2.4 Effect of the receiver's FOV

Figure 11 illustrates the effect of receiver's field of view on the received intensity. Similarly to the other two scenarios, when the FOV is 160°, the received power is the same for both cases. For FOV 180°, the turbid environment achieves better performance. However, for angles lower than 160° the received power is much higher in coastal environment. Finally, for the same receiver's FOV, the received intensity varies only a little among the different simulations (Figure 7).

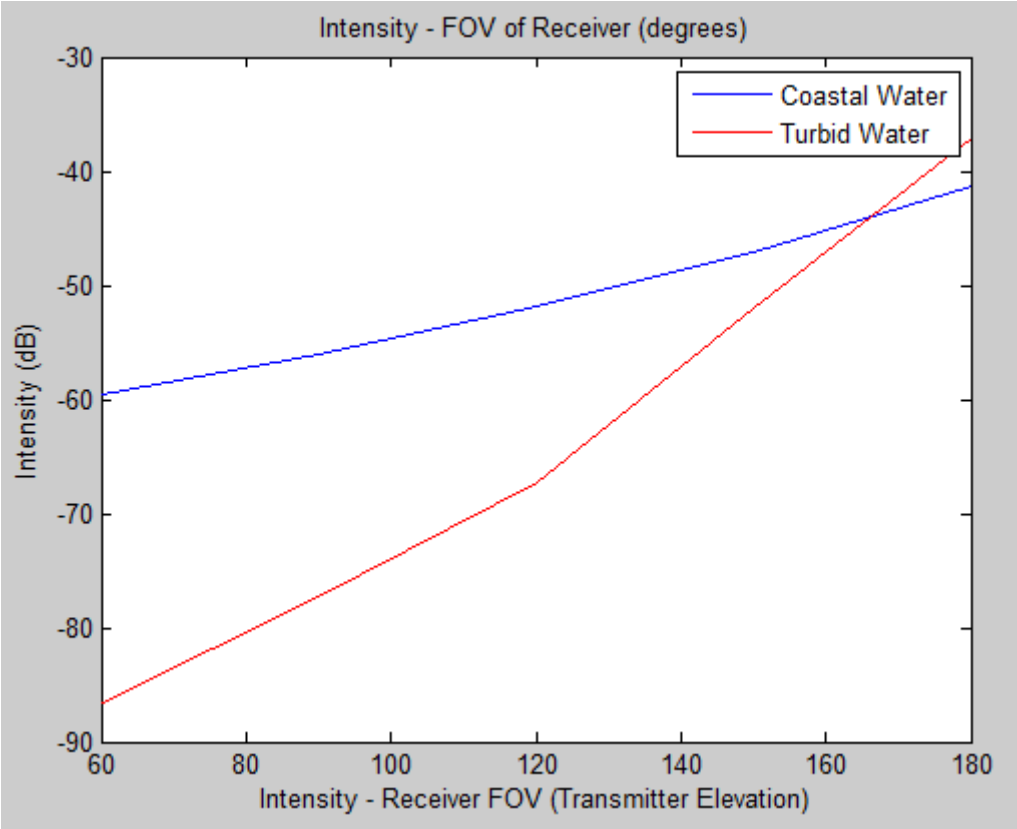

Figure 11: Intensity vs. receiver's FOV for the 3rd scenario.

4.3 Impulse response Scenario

In the following subsections we present the channel impulse response diagrams for coastal and turbid waters and for transmitter to receiver ranges that vary from 10 m to 50 m. The horizontal axis represents the time that the photons reach the receiver and the vertical axis represents the sum of the photon's weights that were received during the set intervals as previously mentioned in 3.2. This sum is in arbitrary units. It should be mentioned that for these simulations the depth of the water is 10 m and that both transmitter and receiver are located at the bottom of the sea. As for the rest configuration characteristics, we have defined $\theta_{Tr} = 45^{o}$, $\varphi_{Tr} = 60^{o}$, $\theta_{Re} = 90^{o}$ and $\varphi_{Re} = 180^{o}$, as analytically described in Section 3.3.

4.3.1 Impulse response for Coastal waters

In Figures Figure 12 to Figure 16 the channel impulse response diagrams are depicted for coastal water environments and for distances between the transmitter and the receiver starting from 10 m in Figure 12 to 50 m in Figure 16 with 10 m step size.

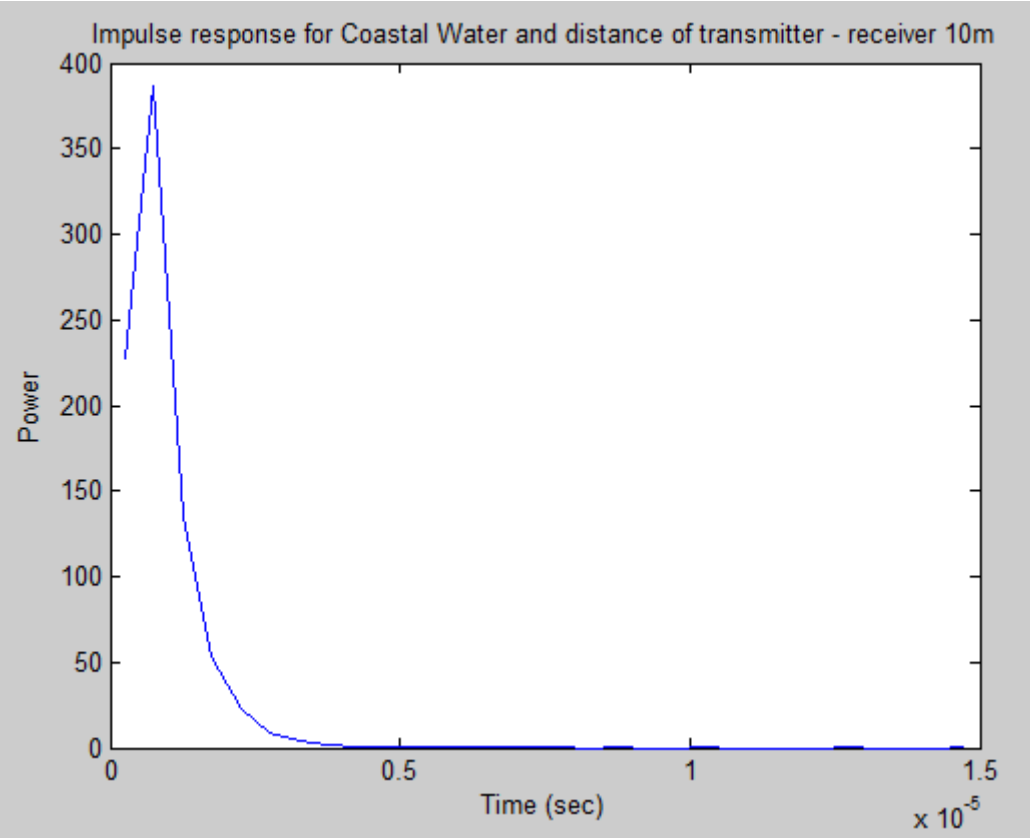

Figure 12: Coastal water. Distance between transmitter and receiver = 10 m.

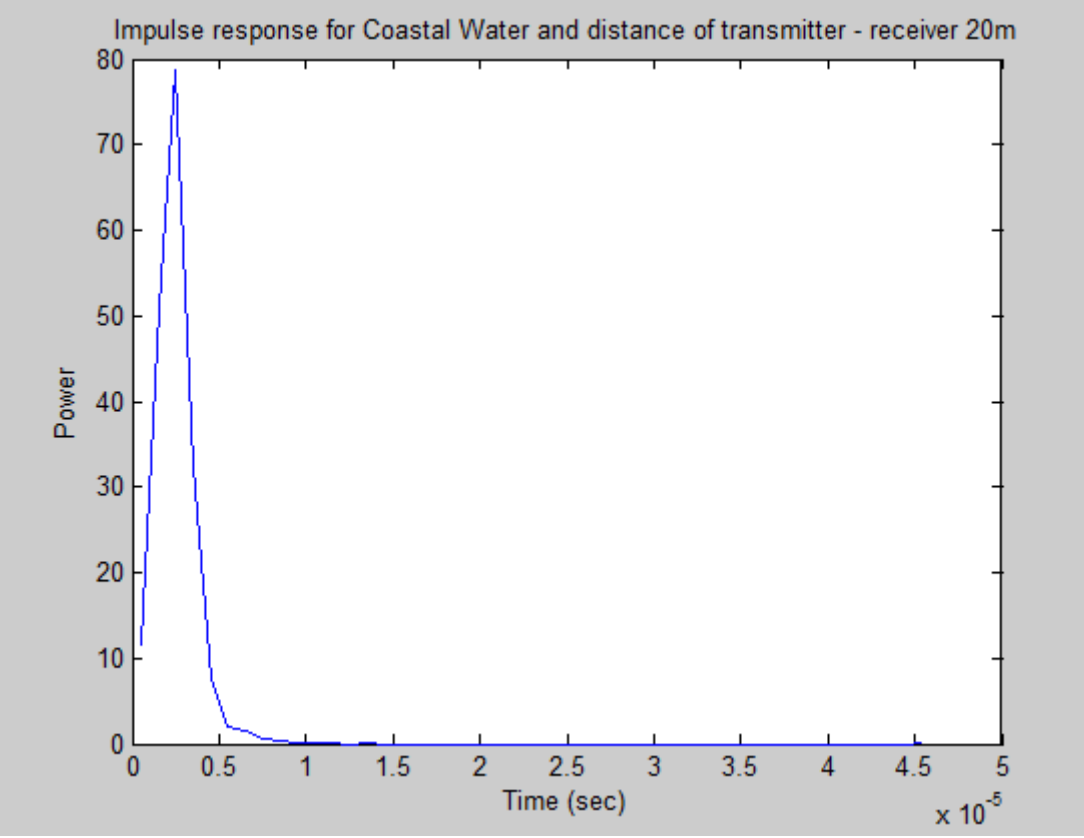

Figure 13: Coastal water. Distance between transmitter and receiver = 20 m.

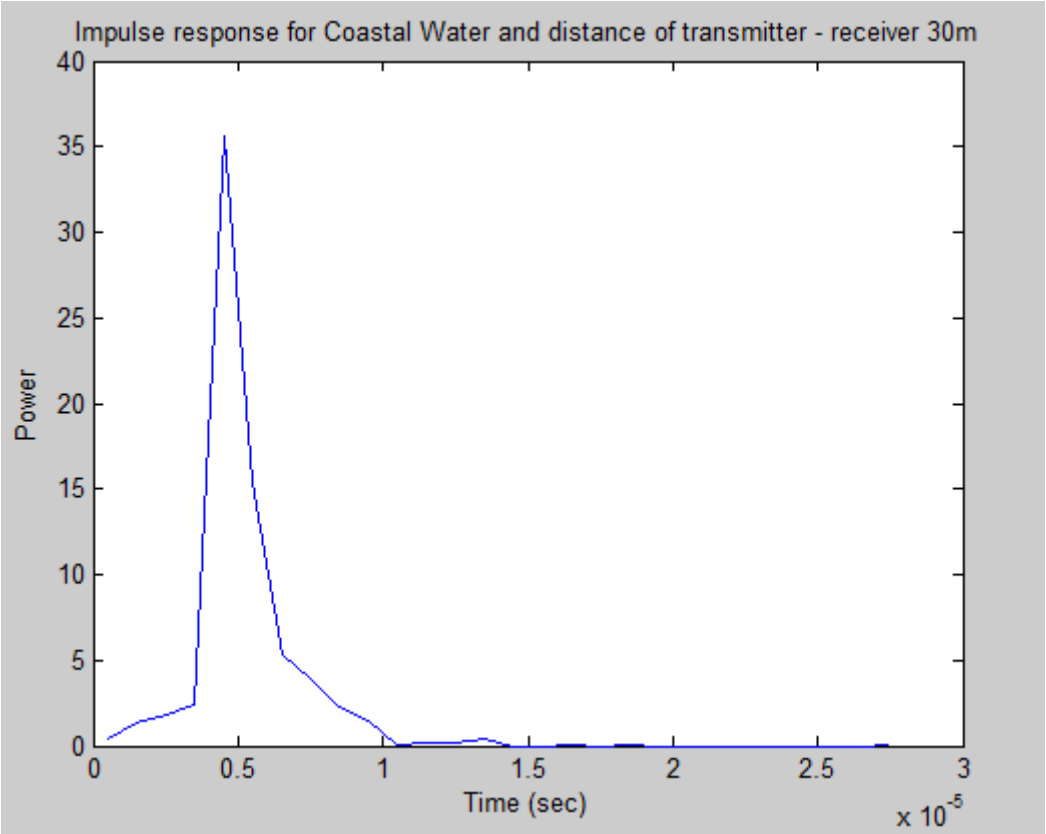

Figure 14: Coastal water. Distance between transmitter and receiver = 30 m.

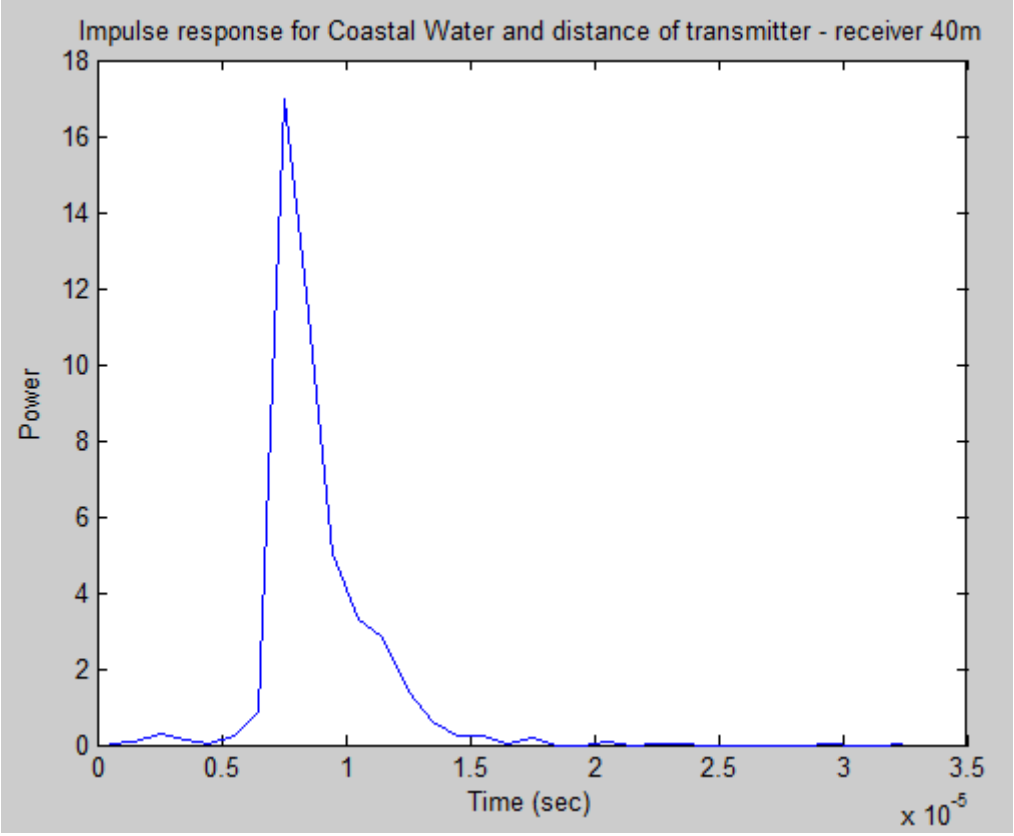

Figure 15: Coastal water. Distance between transmitter and receiver = 40 m.

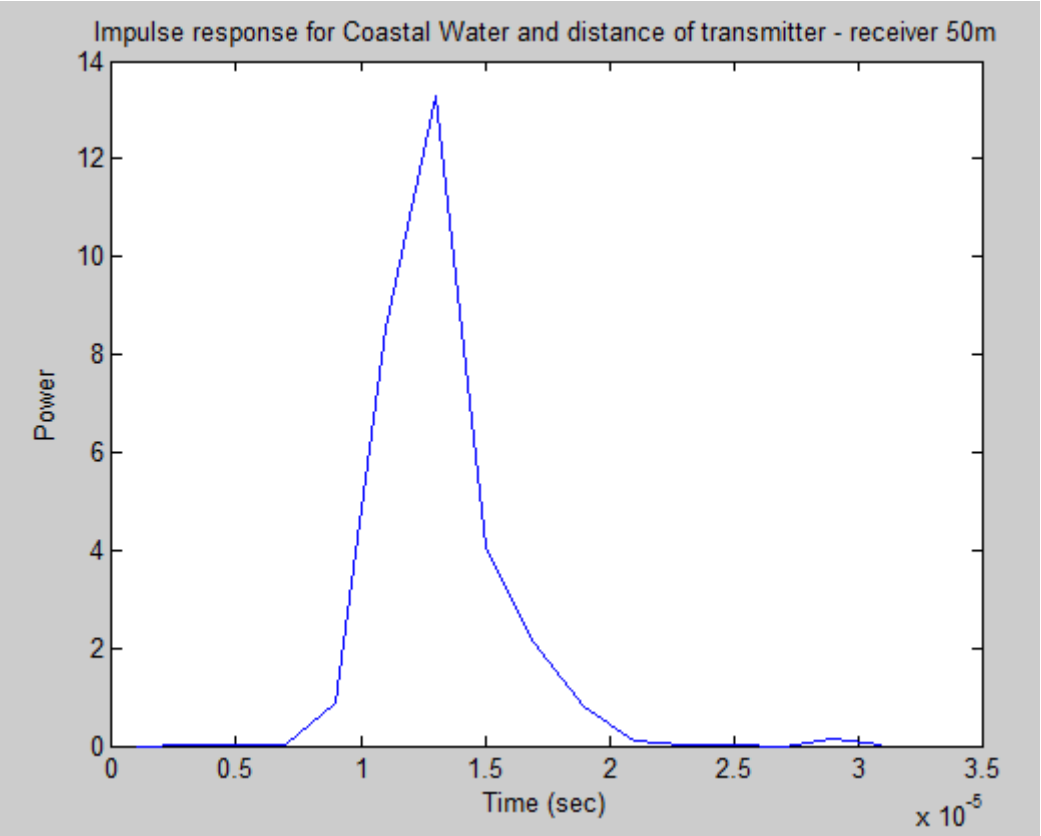

Figure 16: Coastal water. Distance between transmitter and receiver = 50 m.

Comparing the previous Figures, it is obvious that as the distance from transmitter is increased, the peak of the impulse response diagram, i.e. the maximum power, is shifted to later moments and its value is reduced. The shift of the peak power is expected, since the longer the distance is, the more time is needed for the photons to reach the destination. Furthermore, the optical signal loses more energy while "covering" larger paths, as already shown in Figures Figure 5, Figure 6 and Figure 10. This explains the reduced power that is noticed for longer ranges. Lastly, in this coastal environment we observe that for shorter ranges, in particular for 10 m to 30 m, the diagram's lobe in the time domain is narrower compared to larger distances (40 m and 50 m) where the lobe is almost 10^{-5} sec, i.e. two times larger than the lobe for the shorter distances. Therefore, in larger distances the optical beam suffers not only from greater power loss, but also from higher time dispersion.

4.3.2 Impulse response for turbid waters

In Figures Figure 17 to Figure 21, the channel impulse response diagrams are shown for turbid water environments and for various distances. Similarly to the coastal environment, which was examined in Section 4.3.1, as the transmission range is increased, the power peak is reduced and it is shifted to later time moments. As already shown in all previous simulation results, the received power for the same distance between the transmitter and the receiver is larger for turbid waters compared to coastal waters for wide FOV (more than 160^{o}). Moreover, when the distance between the transmitter and the receiver was set equal to 10 m in the turbid water case, the optical signal reaches the receiver sooner than it does for coastal environment, for the same

link range. On the contrary, for longer distances, we do not notice important differences in the photons' reception times between coastal and turbid environments.

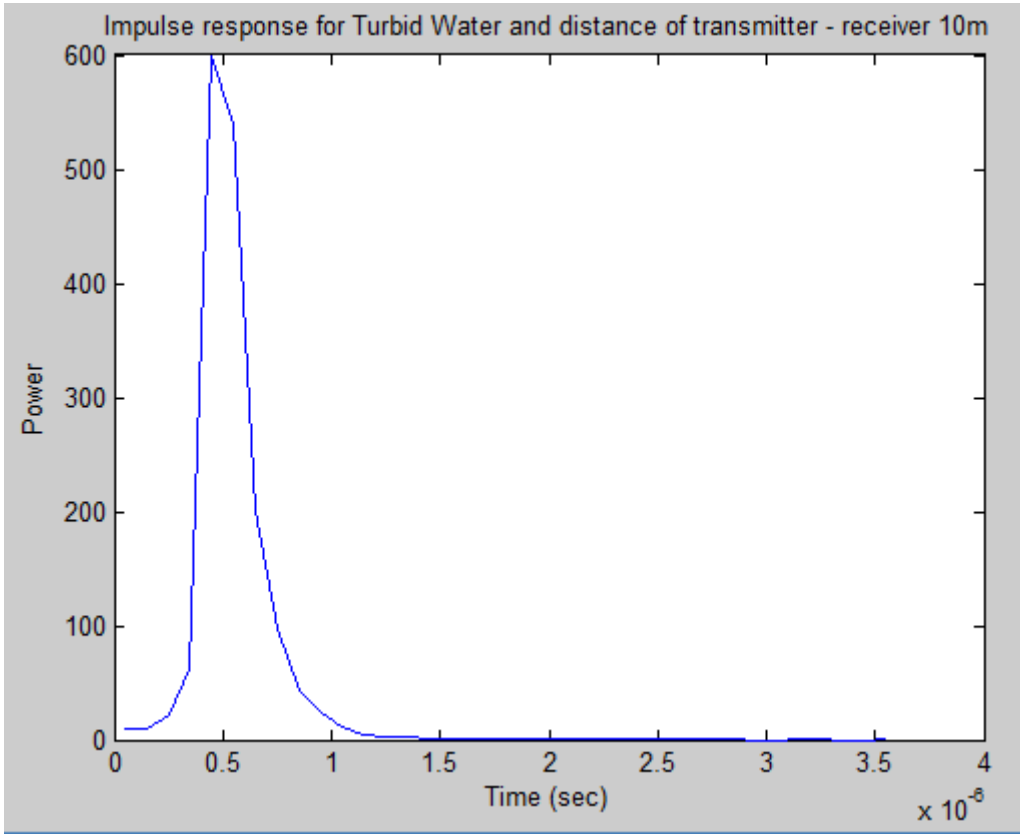

Figure 17: Turbid water. Distance between transmitter and receiver = 10 m.

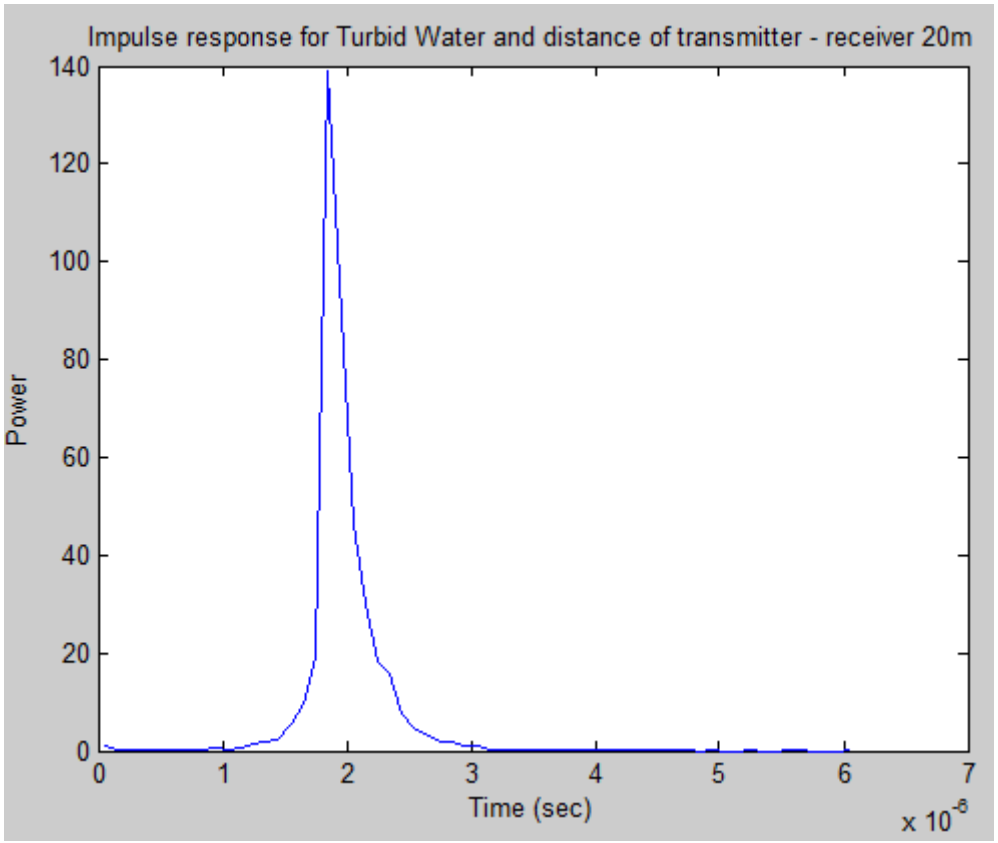

Figure 18: Turbid water. Distance between transmitter and receiver = 20 m.

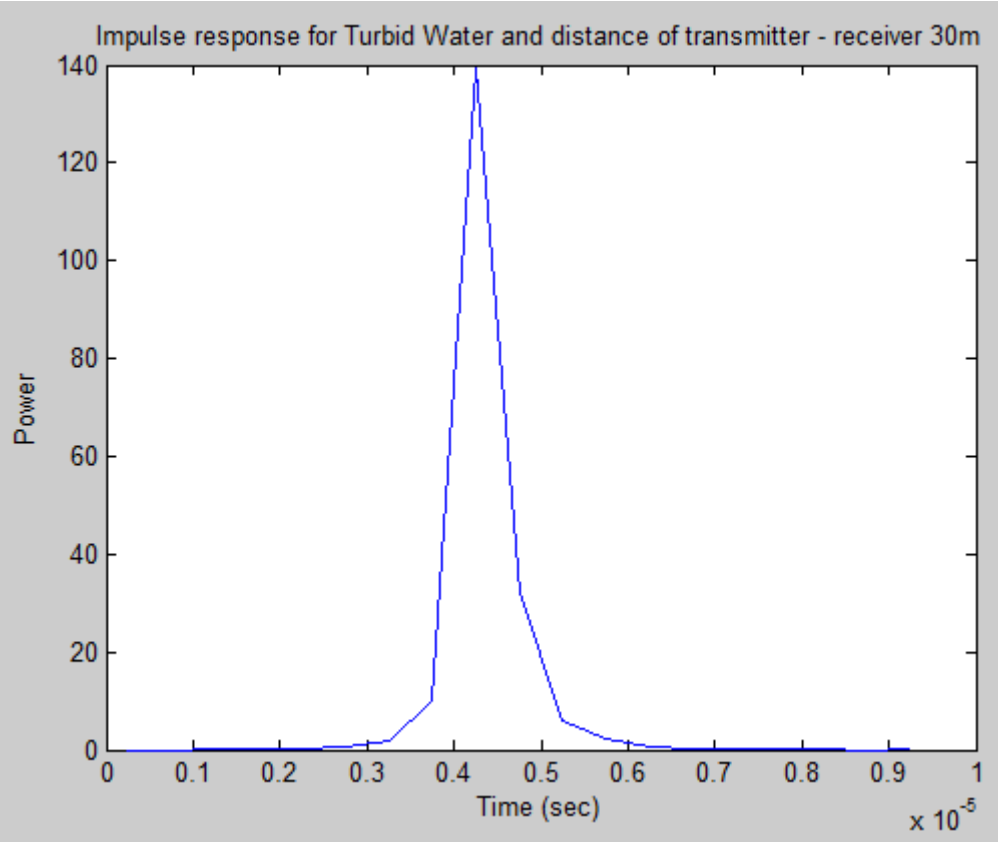

Figure 19: Turbid water. Distance between transmitter and receiver = 30 m.

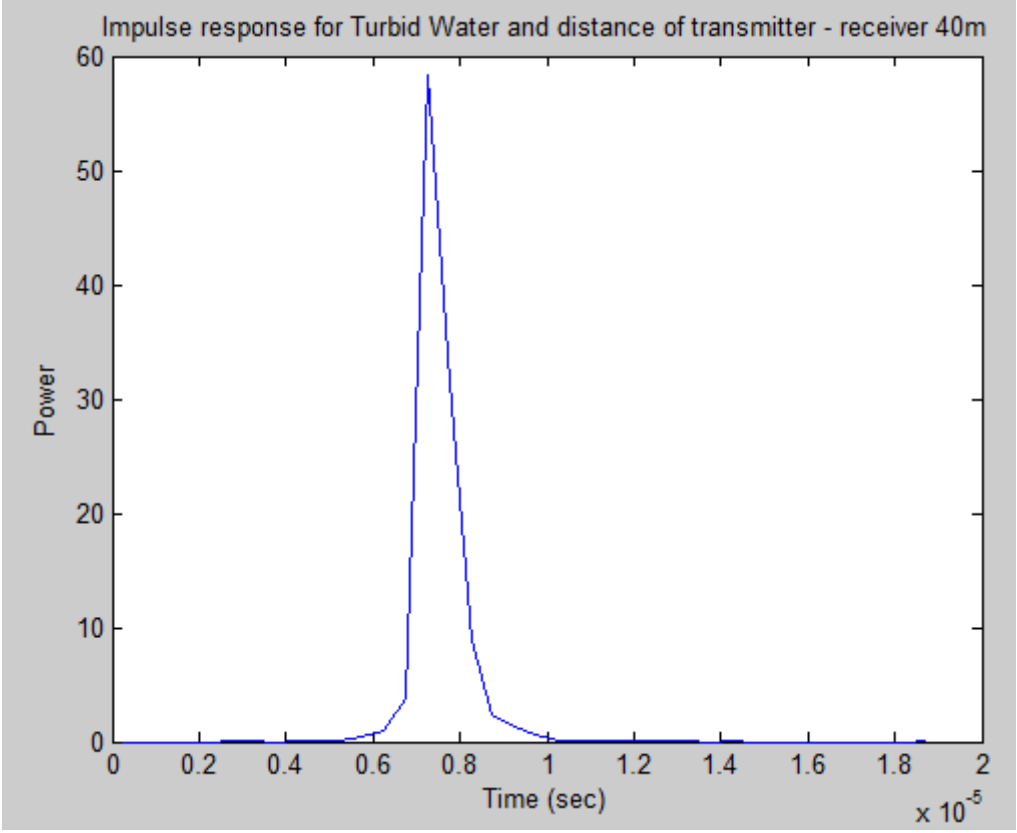

Figure 20: Turbid water. Distance between transmitter and receiver = 40 m.

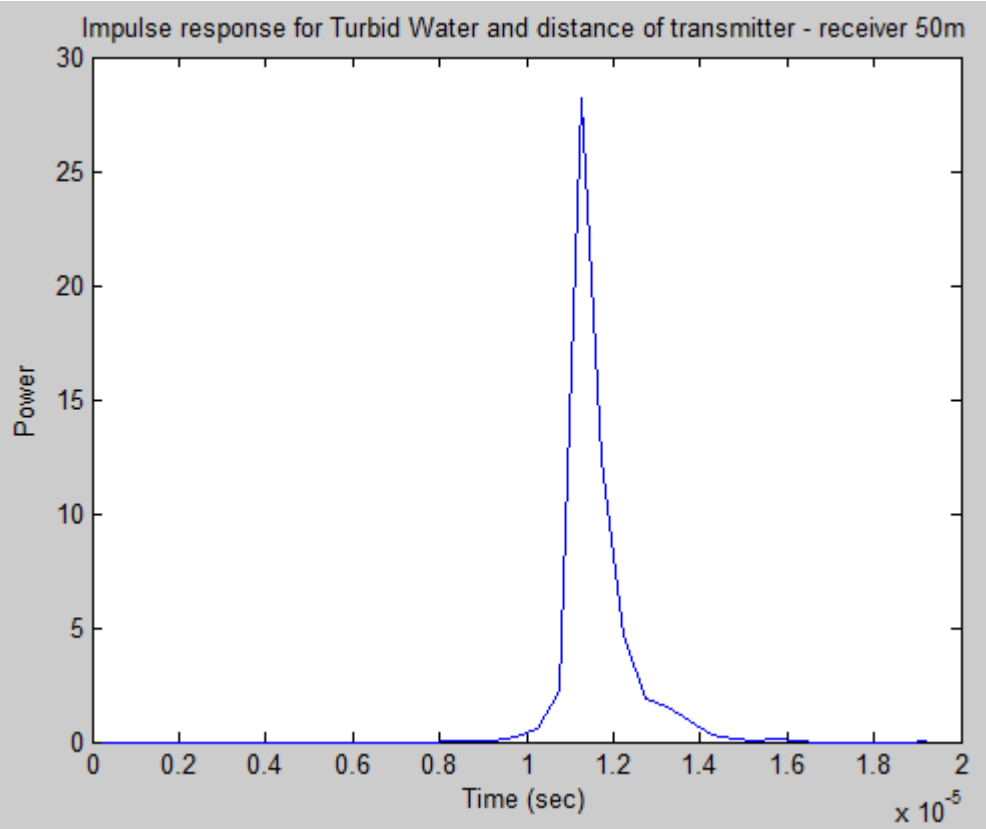

Figure 21: Turbid water. Distance between transmitter and receiver = 50 m.

A major distinction between coastal and turbid waters is that in the turbid water case the width of the diagram's lobe tends to be slowly broadened as the distance is increased, whereas in the coastal water case we notice that the width is more rapidly broadened with increasing distance and thus the channel bandwidth is more rapidly reduced. As a result, in turbid waters, the time dispersion increases with a low rate with distance and is not affected severely by the distance between transmitter and receiver. Generally, if we compare the lobe's width of the impulse response for a turbid environment with the respective lobe for the same distance in the coastal environment, we notice that it is narrower in the turbid case, which means that the time dispersion is lower and the bandwidth of the channel is larger. As a consequence, the turbid water environment is better than the coastal one in an NLOS regime with receivers with wide FOV in two aspects; when a pulsed optical signal is transmitted, it will be less affected in time domain, in terms of pulse broadening and the received power intensity will be higher. These are very interesting findings as we can assume that a link configuration as those examined here, for which it is proved that operates efficiently in a coastal environment, would operate equally as well, or even better, in an environment with more turbid waters with almost no modifications. Thus, the same configuration can be used for two different water environments.

5. CONCLUSIONS

The optical signals are considered to be the most suitable communication method for underwater wireless sensor networks, as they can support higher data rates compared to the acoustic signals, as well as greater link coverage compared to the RF signals. In our thesis, we simulated the NLOS optical underwater configuration through the Monte Carlo technique. We supplement the existing research on non-line-of-sight communication links by examining various NLOS configurations in four different water environments. More specifically, we have designed three simulating scenarios, as described in Section 3.3. In each scenario, we modified various input parameters considering several case studies and we compared the corresponding results. From this comparison, it is generally derived that for all three configurations, where an NLOS link is implemented and the receiver has wide FOV, the more turbid the waters are, the better are the retrieved results in terms of the received intensity and the width of the impulse response in time domain. In the next paragraphs we summarize the most important outcomes of each simulation.

Starting with the transmitter's elevation angle, we noted that when the transmitter and the receiver were located on the bottom of a deep sea, the received intensity was reduced as the elevation angle was increased, as we were getting away from the LOS link configuration. On the contrary, when the nodes were placed in shallow waters, the received power increased with the raise of the elevation angle up to a maximum value. After that value, the intensity started decreasing. The increase of intensity is explained by the raise in the number of internal reflections by components of the initial beam for specific elevation angles, which added more power to the total received intensity. Generally, regarding the relation between the received power and the transmitter's elevation angle, in more clear waters, the low elevation angles resulted in less loss. On the contrary, in more unclean waters, the curves of the diagrams or received intensity had lower slopes or the maximum intensity values were achieved in different angles from the lowest ones depending on the configurations investigated each time, owing to the positive effect of scattering. As far as the transmitter's aperture angle is concerned, it was observed that the received power did not significantly vary while the transmitter aperture angle was increased for the same water environment and the specific configurations considered (elevations angles of the transmitter and the receiver, distance between them, depth values of the water). Finally, especially for non-pure waters, i.e. for clear ocean, coastal and turbid water, the intensity varied only slightly when transmitter aperture angle was modified for each examined case.

While examining the effect of the distance between the transmitter and the receiver, we observed that as the distance was enlarged, the received power was reduced. Furthermore, the obtained results were similar among the different depth scenarios with slight differentiations. Only in pure sea case, a trend of intensity decrease appeared when increasing the distance in shallow waters compared to the deep water environment. From the aforementioned observations and for the specific elevation angles of the transmitter and the receiver, divergence and FOV angles, it is concluded that if we transfer the nodes from a deep sea to a shallow sea, and vice versa, reducing the distance and/or elevating the transmitter above the bottom will not improve the system performance. On the other hand, it may be vital to adapt the transmitter's elevation and aperture angles in order to obtain higher power intensity.

Even though for all the configurations the turbid environment seemed to have the best performance in terms of the intensity, this was true only if the receiver's FOV is 180^{o}.

For smaller FOVs, which were studied only for blurred water, we have noticed that the coastal environment displayed better results than the turbid environment.

Besides the received power for the various simulations, we have also examined the channel impulse response diagram for a certain scenario, but for a variety of transmitter to receiver ranges. The underwater environments that were considered are the coastal and turbid waters. Broadly speaking, it was observed that as the transmitting range was increased, the received power was reduced, while its value was maximized in later time moments. Also, the time dispersion was increased for longer distances. Comparing the two water environments, it was noticed that in turbid water the intensity was stronger and the time dispersion was tighter, making the turbid environment even more suitable for the specific link configurations. Therefore, we can conclude that a configuration which functions well in a coastal environment, it will operate equally as well, if not better, in turbid water.

For verifying the above conclusions it is necessary to design a suitable communicating system, which can be used for experimental tests. Moreover, it would be useful to apply real signals in the communication link in both the simulation as well as the laboratory experiment. As for the simulation, this can be further improved if we take into consideration that the medium's characteristics, such as the refractive index, the scattering and absorption coefficients as well as the HG parameter are not constant in all the water area. Actually, these characteristics vary according to the particles on which the photons are incident to, where the type and the density of the particles depend on the water's type, depth and temperature. Also, the water's wavy surface has not been taken into account either, resulting in less accurate simulation of the internal reflection. Furthermore, in each case we have considered that the receiver's elevation angle is 90^o and based on that, we have implemented the presented simulations. Therefore, the simulation's design can be extended by taking into account the fact that the elevation angle may not be 90^o, the FOV may be less than 180^o, and the receiver may not be placed on the bottom of the underwater area considered. Finally, the simulation that we have demonstrated can be used to examine various scenarios as well as to test more combinations of the implemented scenarios.

TABLE OF TERMINOLOGY

English Term	Greek Term
Absorption	Απορρόφηση
Aperture angle	Γωνία ανοίγματος
Aphotic	Άφωτος
Asymmetry parameter	Παράμετρος ασυμετρίας
Attenuation	Εξασθένηση
Background noise	Θόρυβος περιβάλλοντος
Chlorophyll	Χλωροφύλλη
Clear ocean waters	Νερά καθαρού ωκεανού
Coastal ocean waters	Παράκτια νερά ωκεανού
Colored Dissolved Organic Material	Χρωματισμένο Διαλυμένο Οργανικό Υλικό
Coordinates	Συντεταγμένες
Critical angle	Κρίσιμη Γωνία
Divergence angle	Γωνία απόκλισης
Dysphotic	Δύσφωτος
Elevation angles	Γωνία ανύψωσης
Euphotic	Φωτεινός
Field of View	Οπτικό Πεδίο
Flow diagram	Διάγραμμα ροής
Hybrid system	Υβριδικό σύστημα
Impulse response	Κρουστική απόκριση
Intensity	Ένταση
Inter-Symbol Interference	Δια-συμβολική Παρεμβολή
Line-of-sight	Οπτική επαφή
Optical spectrum	Οπτικό φάσμα
Partition	Διαμέριση
Permittivity	Ορατότητα
Phase function	Συνάρτηση φάσης
Photodetector	Φωτοανιχνευτής
Phytoplankton	Φυτοπλαγκτόν
Preamplifier	Προ-ενισχυτής
Probability density function	Συνάρτηση πυκνότητας πιθανότητας
Pure sea waters	Νερά καθαρής θάλασσας
Reflection	Ανάκλαση
Refractive index	Δείκτης διάθλασης
Roulette technique	Τεχνική ρουλέτας
Salinity	Αλμυρότητα
Scattering	Σκέδαση
Semiconductor	Ημιαγωγός
Simulation	Προσομοίωση
Spectral range	Φασματικό εύρος
Suspended particles	Αιωρούμενα Σωματίδια
Time interval	Χρονικό διάστημα
Thermal noise	Θερμικός θόρυβος
Throughput	Απόδοση
Time spreading	Χρονική διεύρυνση
Trajectory	Τροχιά
Transmission power	Ισχύς μετάδοσης

Turbid harbor waters	Θολά νερά λιμανιού
Turbulence	Αναταραχή
Underwater Wireless Optical Communications	Υποθαλάσσιες Ασύρματες Οπτικές Επικοινωνίες
Velocity	Ταχύτητα
Water molecules	Μόρια Νερού
Wavelength	Μήκος κύματος

ABBREVIATIONS - ACRONYMS

AOP	Apparent Optical Properties
ARQ	Automatic Repeat Request
AUV	Autonomous Underwater Vehicle
BER	Bit Error Rate
BPSK	Binary Phase Shift Keying
CDOM	Colored Dissolved Organic Material
CIR	Channel Impulse Response
CORK-OTS	Circulation Obviation Retrofit Kit - Optical Telemetry System
CW	Continuous Wave
ELF	Extremely Low Frequency
FEC	Forward Error Correction
FOV	Field of View
FSO	Free-Space Optical
HG	Henyey – Greenstein
IOP	Intrinsic (or Inherent) Optical Property
ISI	Inter-Symbol Interference
LED	Light Emitting Diode
LF	Low Frequency
LOS	Line-of-Sight
MIMO	Multiple Input Multiple Output
MURAO	Multi-level Q-learning-based Routing Protocol
NLOS	Non-Line-of-Sight
OFDM	Orthogonal Frequency Division Multiplexing
OWC	Optical Wireless Communication
P&T	Pointing & Tracking
PDF	Probability Distribution Function
QAM	Quadrature Amplitude Modulation
QPSK	Quadrature Phase Shift Keying
RF	Radio – Frequency
ROV	Remotely Operated Vehicle
RTE	Radiative Transfer Equation
SNR	Signal-to-Noise Ratio

SSB	Single Side-Band
TDMA	Time-division Multiple Access
TIR	Total Internal Reflection
UOWC	Underwater Optical Wireless Communication
UTROV	Untethered Remotely Operated Underwater Vehicle
UV	UltraViolet
UWSN	Underwater Wireless Sensor Network
VSF	Volume Scattering Function

ANNEX I

In this annex we present the Matlab code that was implemented for the purposes of the simulation.

```
function [ thetaPh, phiPh, positionPh, directionPh, weightPh ] =
         initialize_photon( thetaTr, phiTr, positionTr )
% Initialize the transmitted photon
%   Input parameters:
%       thetaTr: transmitter's elevation angle
%       phiTr: transmitter's aperture angle
%       positionTr: Transmitter's position in (x, y, z)
                    coordinates system
%   Returned parameters:
%       thetaPh: photon's initial zenith angle
%       phiPh: photon's initial azimuth angle
%       positionPh: Photon's initial position in (x, y, z)
                    coordinates system
%       directionPh: photon's initial direction (μ_x, μ_y, μ_z)
%       weight: photon's initial weight

positionPh = positionTr; %Initial position of photon

%phi of photon
phiPh = 2*pi*rand; %random value in [0, 2π]

%theta of photon
u = acos(1 - rand*(1 - cos(phiTr/2)));
thetaPh = u + pi/2 - thetaTr;

%direction of photon
cos_phi = cos(phiPh);
sin_phi = sin(phiPh);
cos_theta = cos(thetaPh);
sin_theta = sin(thetaPh);
directionPh = [cos_phi*sin_theta, sin_phi*sin_theta, cos_theta];

%wheight of photon
weightPh = 1;

end


function [ position_new ] = move_photon( d, position_old,
                                         direction )
% Moves the photon to its new position according to d, old
position and direction
%   Input parameters:
%       d: step size Δd
%       position_old: photon's previous position
%       direction: photon's current direction
%   Returned parameters:
```

```
%       position_new: Photon's new position

position_new = position_old + direction*d;

end


function [ boolean_value, positionPh_received, out_of_fov] =
received ( positionRe, radiusRe, positionPh, directionPh,
           positionPh_new, fov)
% Returns true if the photon is considered as received. We check
% the cases where the photon may be received
%
%   Input parameters:
%       positionRe: receiver's position in (x, y, z)
%       radiusRe: receiver's radius
%       positionPh: photon's previous position
%       directionPh: photon's current direction
%       positionPh_new: photon's current position
%       fov: receiver's FOV
%   Returned parameters:
%       Boolean_value: this is true if the photon is considered
                       as received. Otherwise, this is false
%       positionPh_received: the position at which the photon is
                             received by the receiver
%       out_of_fov: This is true if the photon is considered as
                    received (boolean_value = true) from a
                    geometrical aspect, but it is out of the
                    receiver's FOV, so it will not be considered
                    as received as the receiver doesn't "see" it.

boolean_value = false;
positionPh_received = positionPh_new;
out_of_fov = false;
if (((positionPh_new(1)-positionRe(1))^2 + (positionPh_new(2)-
      positionRe(2))^2 +(positionPh_new(3)-positionRe(3))^2)<=
      radiusRe^2)
    boolean_value = true;
else
    a = norm(directionPh)^2;
    b= 2*dot(directionPh,positionPh-positionRe);
    c= norm(positionPh-positionRe)^2 - radiusRe^2;

    discr = b^2 - 4*a*c;

    if (discr>=0)
        % This means that line of the photon's direction
          intersects with the sphere. Now we need to check if the
          point of the photon's new position on the line is
          before or after the point where it intersects with the
          sphere.
```

```
        % For this reason, first we find the distance from the
          photon's initial position with point(s) where the line
          intersects with the medium
        d1 = (-b + sqrt(discr)) / 2*a;
        d2 = (-b - sqrt(discr)) / 2*a;
        d_min = min(d1, d2);

        % Distance of phton's new position to its old position
        distancePh_new = norm(positionPh-positionPh_new);

        if (distancePh_new >= d_min)
            % The photon passes inside the sphere, so it is
              received
            boolean_value = true;
            % Now the photon's new position must change so that
              it would be inside the receiver's aperture area.
              The position at which the photon is received is at
              distance d_min from its initial point
            positionPh_received = positionPh+directionPh*d_min;
        end
    end
end

if boolean_value == true
    % We check the diarection's angle and FOV
    line1 = positionPh(3) - positionRe(3); % ΔZ = Zp - Zr
    line2 = norm(positionPh - positionRe); % ΔΦ
    theta = acos(line1/line2);

    if theta <= fov/2
        boolean_value = true;
        out_of_fov = false;
    else
        boolean_value = false;
        out_of_fov = true;
    end
end
end


function [ thetaPh, phiPh, directionPh_new ] = scattering(g,
                                                directionPh)
% Scattering function
%   Input parameters:
%       g: HG asymmetry parameter
%       directionPh: photon's current direction
%
%   Returned parameters:
%       thetaPh: photon's zenith angle after scattering
%       phiPh: photon's azimuth angle after scattering
%       directionPh_new: photon's direction after scattering

% new azimuthal angle
```

```
phiPh = 2 * pi * rand;

% new zenith angle
x = rand;
if (g == 0)
    thetaPh = acos(2 * x - 1);
else
    thetaPh = acos((1 + g^2 - ((1-g^2)/(1-g+2*g*x))^2) / 2*g);
end

% new direction
cos_phi = cos(phiPh);
sin_phi = sin(phiPh);
cos_theta = cos(thetaPh);
sin_theta = sin(thetaPh);
miX = directionPh(1);
miY = directionPh(2);
miZ = directionPh(3);

if (abs(miZ) > 0.99999)
    miX_new = sin_theta * cos_phi;
    miY_new = sin_theta * sin_phi;
    miZ_new = sign(miZ) * cos_theta;
else
    miX_new = (sin_theta / sqrt(1-miZ^2)) * (miX*miZ*cos_phi -
               miY*sin_phi) + miX*cos_theta;
    miY_new = (sin_theta / sqrt(1-miZ^2)) * (miY*miZ*cos_phi +
               miX*sin_phi) + miY*cos_theta;
    miZ_new = -sin_theta * sqrt(1-miZ^2) * cos_phi +
              miZ*cos_theta;
end
directionPh_new = [miX_new, miY_new, miZ_new];

end
```

Simulation

```
clear;
%constants

%variables of medium
%pure sea
%a = 0.053;
%b = 0.003;
%c = 0.056;

%Clear Ocean
%a = 0.069;
%b = 0.08;
%c = 0.15;

%Coastal
```

```
a = 0.088;
b = 0.216;
c = 0.305;

%Turbid harbor
%a = 0.295;
%b = 1.875;
%c = 2.17;

z_min = 0;
z_max = 10;
n_water = 1.333;
n_air = 1;
n_bottom = 1.45;
lamda = 532; %nm

roulete_constand = 10; % This is for roulette functionality
g = 0.924; % HG asymmetry parameter

%variables of transmitter
thetaTr = pi/4;
phiTr = pi/3;
positionTr = [0,0,0];

%variables of receiver
thetaRe = pi/2;
phiRe = pi/3; % Receiver's FOV
positionRe = [20,0,0];
radiusRe = 0.2;

%variables of photons
N = 1e6;
weight_thr = 10^(-4);

%initialize arrays for photons
photons_distance = zeros(N,1); % The total distance that each
                                  photon traveled
photons_weight = zeros(N,1);
photons_time = zeros(N,1); % The time that each photon reached
                              the receiver


photons_received = 0;
total_intensity = 0;

%speed in the water
speed_in_space = 3*1e8;
v = speed_in_space / n_water;

for i=1:N
    %initialize photon
    [ thetaPh, phiPh, positionPh, directionPh, weightPh ] =
      initialize_photon( thetaTr, phiTr, positionTr );
```

```
reached = false;
total_distance = 0;
total_time = 0;

while ~reached && weightPh > 0
    %move the photon
    d = - log(rand)/c;
    positionPh_new = move_photon(d, positionPh,
                                 directionPh);

    %We check if the photon exceeds the medium
    if positionPh_new(3) > z_max
        % If the photon gets to the air

        % Photon's new position is on the surface
        z_new = z_max;
        d = (z_max - positionPh(3))/directionPh(3);%distance
        x_new = positionPh(1) + directionPh(1)*d;
        y_new = positionPh(2) + directionPh(2)*d;
        positionPh_new = [x_new, y_new, z_new];

        t = d/v;
        total_distance = total_distance + d;
        total_time = total_time + t;

        %computation of Fresnel reflection coefficient
        %refraction angle
        thetaRefr = asin(n_water*sin(thetaPh)/n_air);
        % Fresnel coefficient
        fresnel_co = 1/2 * (((sin(thetaPh-thetaRefr))^2)
                           /((sin(thetaPh+thetaRefr))^2) +
                            ((tan(thetaPh-thetaRefr))^2)
                           /((tan(thetaPh+thetaRefr))^2));

        % We check if we have internal reflection
        rand_var = rand;
        if rand_var < fresnel_co
            %internal reflection
            directionPh(3) = -directionPh(3); % z_new = -z
        else
            %in the air
            weightPh = 0;
        end
    elseif positionPh_new(3) < z_min
        %If the photon reached the bottom

        %Photon's new position is on the bottom
        z_new = z_min;
        d = (z_min - positionPh(3))/directionPh(3);

        x_new = positionPh(1) + directionPh(1)*d;
        y_new = positionPh(2) + directionPh(2)*d;
        positionPh_new = [x_new, y_new, z_new];
```

```
            t = d/v;
            total_distance = total_distance + d;
            total_time = total_time + t;

            % refraction angle
            thetaRefr = asin(n_water*sin(thetaPh)/n_bottom);
            % Fresnel coefficient
            fresnel_co = 1/2 * (((sin(thetaPh-thetaRefr))^2)
                              /((sin(thetaPh + thetaRefr))^2) +
                               ((tan(thetaPh - thetaRefr))^2)
                              /((tan(thetaPh + thetaRefr))^2));

            % At this point z = z_min. But we still need to
              check if the photon is received.

            [reached, positionPh_received, out_of_fov] =
             received(positionRe, radiusRe, positionPh,
                      directionPh, positionPh_new, phiRe);

            if (reached && out_of_fov==false)
                positionPh_new = positionPh_received;
                photons_received = photons_received + 1;
                total_intensity = total_intensity + weightPh;
                photons_time(i) = total_time;
                break; % since the photon is received, there is
                         no need to calculate absorption and
                         scattering
            elseif (reached==false && out_of_fov)
                positionPh_new = positionPh;
            end

            %We check if we have internal reflection
            rand_var = rand;
            if rand_var < fresnel_co
                %internal reflection
                directionPh(3) = -directionPh(3); % z_new = -z
            else
                %in the sand -> it is lost
                weightPh = 0;
            end

        else
            %The photon is in the water
            % Check if the photon is received
            [reached, positionPh_received, out_of_fov] =
             received(positionRe, radiusRe, positionPh,
                      directionPh, positionPh_new, phiRe);

            distance = norm(positionPh-positionPh_received)^2;
            t = distance/v;
            total_distance = total_distance + distance;
            total_time = total_time + t;
```

```
            if (reached && out_of_fov==false)
                positionPh_new = positionPh_received;
                photons_received = photons_received + 1;
                total_intensity = total_intensity + weightPh;
                photons_time(i) = total_time;
                break; % since the photon is received, there is
                         no need to calculate absorption and
                         scattering
            elseif (reached==false && out_of_fov)
                positionPh_new = positionPh;
            end

            % The photon is in the water and not received. So
              the Monte Carlo continues
            %absorption
            weightPh_new = absorb(weightPh, a, c);
            weightPh = weightPh_new;

            % We check the photon's weight
            if (weightPh < weight_thr)
                %roulette
                propability_of_survival = 1 / roulete_constand;
                x = rand;
                if (x <= propability_of_survival)
                    weightPh = roulete_constand * weightPh;
                else
                    weightPh = 0;
                    break;
                end
            end


            % scattering
            [thetaPh_new, phiPh_new, directionPh_new] =
             scattering(g, directionPh);

            thetaPh = thetaPh_new;
            phiPh = phiPh_new;
            directionPh = directionPh_new;
        end
        positionPh = positionPh_new;
    end

    %in the end, before moving to the next photons we save the
     followings

    photons_weight(i) = weightPh;
    photons_distance(i) = total_distance;

end
intensity = 10*log10(total_intensity/N);
photons_percentage = (photons_received/N)*100;
save('results');
```

REFERENCES

[1] Ch. Gabriel et al., Monte-Carlo-Based Channel Characterization for Underwater Optical Communication Systems, Journal of Optical Communications and Networking, Jan. 2013.

[2] Ch. Gabriel et al., "Channel Modeling for Underwater Optical Communication", *GLOBECOM Workshops (GC Wkshps)*, IEEE, Dec. 2011.

[3] Z. Zeng et al.,A Survey of Underwater Optical Wireless Communications, Commun. Surveys Tuts, IEEE, Oct. 2016.

[4] W. Charles, "Simulation, Modeling, and Design of Underwater Optical Communication Systems", Ph.D Dissertation, Electrical Engineering, North Carolina State University, Feb. 2012.

[5] H. Kaushal and G. Kaddoum, Underwater Optical Wireless Communication, IEEE Access, April 2016

[6] Wikipedia*, Radiance*, https://en.wikipedia.org/wiki/Radiance. [26/07/2017]

[7] Wikipedia, *Irradiance*, https://en.wikipedia.org/wiki/Irradiance. [26/07/2017]

[8] Wikipedia, *Reflectance*, https://en.wikipedia.org/wiki/Reflectance. [26/07/2017]

[9] S. Arnon and D. Kedar, Non-line-of-sight underwater optical wireless communication network, J. Opt. Soc. Am. A, OSA, March 2009.

[10] V. L. Haltrin and G. W. Kattawar, "Self-consistent solutions to the equation of transfer with elastic and inelastic scattering in oceanic optics: I. model", Applied Optics, Sept.1993.

[11] C. D. Mobley, *Light and Water: Radiative transfer in natural waters*, Academic Press, June 1994.

[12] D. Anguita et al., "Optical wireless underwater communication for AUV: Preliminary simulation and experimental results," *Proc. OCEANS Conf. 2011*, Santander, Spain, June 2011.

[13] M. A. Chancey, "Short range underwater optical communication links," M.S. thesis, Dept. Elect. Eng., North Carolina State Univ., Raleigh, NC, USA, 2005.

[14] J. A. Simpson, "A 1 Mbps underwater communications system using LEDs and photodiodes with signal processing capability," M.S. thesis, Dept. Elect. Eng., North Carolina State Univ., Raleigh, NC, USA, 2007.

[15] D. Kedar and Shl. Arnon, Subsea ultraviolet solar-blind broadband free-space optics communication, *Opt. Eng*., April 2009.

[16] M. V. Jamali and J. A. Salehi and F. Akhoundi, Performance Studies of Underwater Wireless Optical Communication Systems with Spatial Diversity: MIMO Scheme, IEEE Trans. Commun., IEEE, Dec. 2016.

[17] I. F. Akyildiz, D. Pompili and T. Melodia, "Underwater acoustic sensor networks: research challenges", Ad Hoc Networks 3, p. 257 – 279, 2005.

[18] R. E. Williams and H. F. Battestin, ''Coherent recombination of acoustic multipath signals propagated in the deep ocean'', J. Acoust. Soc. Amer., p. 1433, 1971.

[19] A. I. Al-Shamma'a, A. Shaw, and S. Saman, Propagation of electromagnetic waves at MHz frequencies through seawater, IEEE Trans. Antennas Propag., Nov. 2004.

[20] M. R. Frater, M. J. Ryan, and R. M. Dunbar, ''Electromagnetic communications within swarms of autonomous underwater vehicles'', *Proc. 1st ACM Underwater Netw.*, Sept. 2006.

[21] H. Kulhandjian, "Inside out: Underwater communications", J. Ocean Technol., pp. 104–105, 2014.

[22] M. Lanzagorta, "Underwater Communications", San Rafael, CA, USA: Morgan & Claypool, 2013.

[23] P. M. C. P. C. de Freitas, "Evaluation of Wi-Fi underwater networks in freshwater", Ph.D. dissertation, Faculdade Engenharia Univ. Porto, Porto, Portugal, 2014.

[24] Judith Bannon Snow et al., "Underwater propagation of high data rate laser communications pulses", Ocean Optics XI, SPIE, 1992.

[25] J. W. Bales and C. Chryssostomidis, ''High-bandwidth, low-power, short-range optical communication underwater'', *Proc. 9th Int. Symp. Unmanned, Untethered Submersible Technol.*, Durham, NH, USA, 1995.

[26] J. W. Giles and I. N. Bankman, "Underwater optical communications systems, Part 2: Basic design considerations", *Proc. IEEE Military Commun. Conf.*, 2005.

[27] N. Farr, J. Ware, C. Pontbriand and T. Hammar, "Optical communication system expands CORK seafloor observatory's bandwidth", *Proc. OCEANS Conf. 2010*, Seattle, WA, 2010.

[28] Hoa Le Minh et al., "80 Mbit/s Visible Light Communications using pre-equalized white LED", *2008 34th European Conference on Optical Communication*, IEEE, 2008.

[29] Kaiyun Cui et al., "Indoor optical wireless communication by ultraviolet and visible light", *Proc. SPIE 7464, Free-Space Laser Communications IX*, Aug. 2009.

[30] N. Farr et al., "Optical modem technology for seafloor observatories", *Proc. of IEEE oceans Conf. 2005*, IEEE, 2005.

[31] D. Anguita and D. Brizzolara, "Optical wireless communication for underwater Wireless Sensor Networks: Hardware modules and circuits design and implementation", *Proc. OCEANS Conf. 2010*, Seattle, WA, 2010.

[32] Fr. Hanson and St. Radic, “High bandwidth underwater optical communication”, Applied Optics, Jan. 2008.
[33] S. Jaruwatanadilok, “Channel Modeling and Performance Evaluation using Vector Radiative Transfer Theory”, 2008.
[34] A. Laux et al., “The a, b, cs of oceanographic lidar predictions: a significant step toward closing the loop between theory and experiment”, Journal of Modern Optics, March 2002.
[35] Br. Cochenour et al., “Effects of multiple scattering on the implementation of an underwater wireless optical communications link”, *Proc. OCEANS Conf. 2006*, IEEE, Sept. 2006
[36] Br. Cochenour, L. Mullen and Al. Laux, “Phase Coherent Digital Communications for Wireless Optical Links in Turbid Underwater Environments”, *Proc. OCEANS Conf. 2007*, IEEE, Oct. 2007.
[37] L. Mullen et al., “Backscatter suppression for underwater modulating retroreflector links using polarization discrimination”, Applied Optics, Jan. 2009
[38] Br. Cochenour, L. J. Mullen and Al. E. Laux, “Characterization of the Beam-Spread Function for Underwater Wireless Optical Communications Links”, IEEE J. Ocean. Eng., IEEE, Oct. 2008.
[39] M. Doniec and D. Rus, “Bidirectional optical communication with AquaOptical II”, *Proc. IEEE Int. Conf. Commun. Syst.*, IEEE, Nov. 2010.
[40] D. Kedar and Shl. Arnon, “Optical wireless communication through fog in the presence of pointing errors”, Applied optics, Aug. 2003.
[41] G. Baiden, Y. Bissiri, and A. Masoti, ‘‘Paving the way for a future underwater omnidirectional wireless optical communication systems’’, Ocean Eng., 2009.
[42] *High-Bandwidth Underwater Transceiver*, http://www.ambalux.com. [26/07/2017]
[43] F. Jasman and R. J. Green, ‘‘Monte carlo simulation for underwater optical wireless communications’’ *Proc. IEEE 2nd Int. Workshop Opt. Wireless Commun.*, Newcastle upon Tyne, U.K., Oct.2013.
[44] G. Baiden and Y. Bissiri, ‘‘High bandwidth optical networking for underwater untethered telerobotic operation’’, *Proc. OCEANS Conf. 2007*, IEEE, Oct. 2007.
[45] Shl. Arnon, Underwater optical wireless communication network, *Opt. Eng*., Jan. 2010.
[46] I. Vasilescu et al., “Data collection, storage, and retrieval with an underwater sensor network’’, *Proc. 3rd Int. Conf. Embedded Netw. Sensor Syst.*, 2005.
[47] N. Farr et al., “An integrated, underwater optical/acoustic communications system”, *Proc. OCEANS Conf. 2010*, Sydney, Australia, May 2010.
[48] N. Farr et al., “Demonstration of wireless data harvesting from a subsea node using a ‘ship of opportunity”, *Proc. OCEANS Conf. 2013*, San Diego, USA, 2013.
[49] L. J. Johnson, R. J. Green, and M. S. Leeson, ‘‘Hybrid underwater optical/acoustic link design”, *Proc. 16th Int. Conf. Transparent Opt. Netw.*, Graz, Austria, Jul. 2014.
[50] T. Hu and Y. Fei, “MURAO: A multi-level routing protocol for acoustic-optical hybrid underwater wireless sensor networks”, *Proc. 9th Annu. IEEE Commun. Soc. Conf. Sensor, Mesh Ad Hoc Commun. Netw. (SECON)*, Seoul, South Korea, Jun. 2012.
[51] S. Han et al., “Evaluation of underwater optical-acoustic hybrid network”, China Commun., May 2014.
[52] I. Vasilescu, C. Detweiler, and D. Rus, “Aquanodes: An underwater sensor network”, *Proc. ACM Int. Workshop Underwater Netw. Syst. (WUWNet)*, Montreal, Canada, 2007.
[53] S. A. Prahl et al., “A Monte Carlo Model of Light Propagation in Tissue”, *SPIE Proc. of Dosimetry of Laser Radiation in Medicine and Biology*, 1989.
[54] Sh. Tang, X. Zhang and Yuh. Dong, “On Impulse Response for Underwater Wireless Optical Links”, *Proc. OCEANS Conf. 2013*, Bergen, Norway, Sept. 2013.
[55] Sh. Tang, Yuh. Dong and X. Zhang, Impulse Response Modeling for Underwater Wireless Optical Communication Links, IEEE Trans. Commun., IEEE, Dec. 2013.
[56] Wikipedia, *Line–sphere intersection*, https://en.wikipedia.org/wiki/Line%E2%80%93sphere_intersection. [26/07/2017]
[57] *Angle between two 3D lines*, https://math.stackexchange.com/questions/463415/angle-between-two-3d-lines. [26/07/2017]
[58] R.W. Fenn, "Optical and infrared properties of the atmosphere", Chapter 18 in Handbook of Geophysics and the Space Environment, 1985.